ADSORPTION KINETICS AND DYNAMICS OF SMALL MOLECULES ON GRAPHENE AND GRAPHENE OXIDE

A Dissertation
Submitted to the Graduate Faculty
of the
North Dakota State University
of Agriculture and Applied Science

By

Nilushni Sivapragasam

In Partial Fulfillment of the Requirements
for the Degree of
DOCTOR OF PHILOSOPHY

Major Department:
Chemistry and Biochemistry

February 2018

Fargo, North Dakota

North Dakota State University
Graduate School

Title

Adsorption kinetics and dynamics of small molecules on graphene and graphene oxide

By

Nilushni Sivapragasam

The Supervisory Committee certifies that this ***disquisition*** complies with North Dakota State University's regulations and meets the accepted standards for the degree of

DOCTOR OF PHILOSOPHY

SUPERVISORY COMMITTEE:

Dr. Uwe Burghaus
Chair

Dr. John Hershberger

Dr. Svetlana Kilina

Dr. Wei Lin

Approved:

02-20-2018
Date

Dr. Gregory Cook
Department Chair

ABSTRACT

Graphene is an allotrope of carbon composed of sp^2 hybridized carbon and arranged into a honeycomb lattice. Graphene is a mechanically strong material (200 times stronger than steel) and has high carrier mobility, high thermal conductivity, and high optical transparency. Owing to these outstanding properties graphene is used in many applications; often graphene is used on a support instead as a free-standing graphene. When graphene is utilized it can adsorb many molecules and this adsorption could be influenced by the support. Furthermore, comparing the adsorption of such molecules on the support alone and on the supported graphene (graphene on the support) could provide details on the transparency of graphene; transparency can be defined as the identical interactions of a molecule on a supported graphene and the respective support. Therefore, this dissertation focused on studying the adsorption kinetics and dynamics of selected molecules (water, benzene, n-alkane, and carbon dioxide) on two different types of graphene: chemical vapor deposited (CVD) and physical vapor deposited (PVD) graphene. In addition, the chemically inert graphene was functionalized with oxygen to produce graphene oxide and the reactivity of graphene oxide on carbon dioxide adsorption was studied. All the experiments were carried at ultrahigh vacuum conditions to ensure an atomically clean environment.

The PVD graphene was synthesized on Ru(0001) and was further functionalized with oxygen to produce graphene oxide. The surface characterizations were carried out by various surface analytical techniques: Auger electron spectroscopy (AES), low energy electron diffraction (LEED), and X-ray photoelectron spectroscopy (XPS). The adsorption kinetics and dynamics were studied by thermal desorption spectroscopy (TDS) and molecular beam scattering techniques, respectively. Transparency of graphene, support effects, and the reactivity of graphene oxide were mapped. The studies clearly showed that the transparency of graphene depends on the

polarizability of the molecule and the supports; the supports indeed influenced the adsorption of molecules on graphene. In addition, graphene oxide did not react with CO_2 to produce any reaction products but it enhanced the CO_2 adsorption.

ACKNOWLEDGMENTS

I am thankful to all those who contributed and supported my journey throughout the last few years at grad school. My advisor Dr. Uwe Burghaus provided me a timely guidance to make these four years successful in his lab. Thanks to all the mentorship you have given, which was essential for me to live through this journey. My committee members Dr. John Hershberger, Dr. Svetlana Kilina, and Dr. Wei Lin considered me as their own grad student and were always open for discussions without any hesitations and provided me the necessary support as and when I needed.

I am also thankful to North Dakota State University for the acceptance into grad school initially as a MS student at the Department of Food Sciences and then as a PhD student at the Department of Chemistry and Biochemistry. I am indebted to both the faculty at the Department of Food Science and the Department of Chemistry and Biochemistry. I am happy and proud to be a part of the Bison family.

Lastly, I would have not made it this far without the support of my family who were always there for me. My journey at grad school involved a lot of sacrifices, commitments, and compromises and my family was the greatest support for me in making my days, months, and years fruitful.

TABLE OF CONTENTS

LIST OF TABLES

LIST OF FIGURES

LIST OF ABBREVIATIONS

AES .....Auger Electron Spectroscopy

CMA .....Cylindrical Mirror Analyzer

CNT.....Carbon Nanotube

CPO.....Chloroperoxidase

CVD .....Chemical Vapor Deposition

DMF.....Dimethyl Formamide

ESCA .....Electron Spectroscopy for Chemical Analysis

FET .....Field Effect Transistor

FTIR.....Fourier Transform Infrared Spectroscopy

HSA.....Hemispherical Sector Analyzer

HV.....High voltage

KE .....Kinetic Energy

L .....Langmuir

LASER.....Light Amplification by Stimulated Emission of Radiation

LEED .....Low Energy Electron Diffraction

MBS .....Molecular Beam Scattering

ML.....Monolayer

MWCNT .....Multi-walled Carbon Nanotube

NMP.....N-methyl-2-pyrrolidone

PDMS.....Polydimethyl Siloxane

PMMA .....Poly-methyl methacrylate

PVD.....Physical Vapor Deposition

QMS.....Quadrupole Mass Spectrometer

RBM.....Radial Breathing Mode

SAR.....Structure Activity Relationship

SDBS.....Sodium Dodecyl Benzene Sulfonate

SWCNT.....Single-walled Carbon Nanotube

TBA.....Tetrabutylammonium

TDS.....Thermal Desorption Spectroscopy

TOF.....Time-of-Flight Spectroscopy

UHV.....Ultra-High Vacuum

XPS.....X-ray Photoelectron Spectroscopy

LIST OF SYMBOLS

β ..... Heating rate

θ.....Coverage

θ_M .....Coverage of adsorbate

θ_{sat}.....Saturation coverage

λ.....Molecular mean free path length

λ.....Wavelength

ν.....Pre-exponential factor

Φ.....Work function of the surface

χ.....Exposure

Δt.....Time duration

c.....Velocity of light

d.....Nozzle diameter

dN/dE .....Differential number of electrons with energy E

E_a.....Activation energy

E_{des}.....Energy of desorption

E_i .....Impact energy

eV.....Electron volt

E_{vac} .....Vacuum level

h.....Planck's constant

k.....Desorption rate

k_d .....Desorption rate coefficient

keV.....Kilo electron volt

KL_1L_2 .....Auger transition

m/e.....Mass to charge ratio

N.....Number of molecules

n.....Order of the reaction

N(E).....Number of electrons with energy E

P .....Pressure in mbar

P_0 .....Initial pressure

P_b .....Base pressure

P_{sat} .....Saturation pressure

r .....Reaction rate

S(Θ).....Coverage dependent adsorption probability

S_0 .....Initial adsorption probability

T_s .....Surface temperature

T_0.....Initial surface temperature

V.....Voltage

Z .....Atomic number

CHAPTER 1. INTRODUCTION

This dissertation focused on studying the adsorption of small molecule (water, benzene, n-alkanes, and carbon dioxide) on graphene and graphene oxide. Graphene is a two-dimensional allotrope of carbon with a thickness of just one atomic layer. The sp^2 hybridized carbon in graphene makes it, both, chemically stable and mechanically stronger. Graphene also possesses a high surface area (2600 m^2g^{-1}), high carrier mobility (1000 $cm^2V^{-1}s^{-1}$), and high thermal conductivity (4000 $Wm^{-1}K^{-1}$).[1] Owing to these outstanding properties, graphene has been used in many applications; almost all applications utilize graphene on a support (supported or epitaxial graphene) instead of a free-standing graphene. The supports on which graphene is placed could influence the properties of graphene. Therefore, this dissertation was aimed at studying the adsorption kinetics and dynamics of small molecule on several different supported graphene and the respective supports. In addition, graphene oxide was synthesized by functionalizing graphene. The reactive oxygen species on graphene can act as active sites to enhance the adsorption of small molecules; reactive oxygen can also involve in reactions on the adsorbed molecules. Overall, the support effects on small molecule adsorption on supported graphene, enhancement of adsorption kinetics and dynamics of small molecules on graphene oxide, and the reactivity of graphene oxide were studied.

This dissertation is composed of four main projects (figure 1). The first study (chapter 4) describes the adsorption of water on supported graphene (graphene/Ru(0001), graphene/Cu, and graphene/SiO_2) and the respective supports (Ru(0001), Cu, and SiO_2). The transparency of graphene and the support effects were addressed by studying the adsorption kinetics of graphene; graphene is considered transparent if the adsorption kinetics on the supported graphene mimics the

support. The findings showed that the supports influenced the water adsorption on graphene and graphene was translucent for water adsorption.

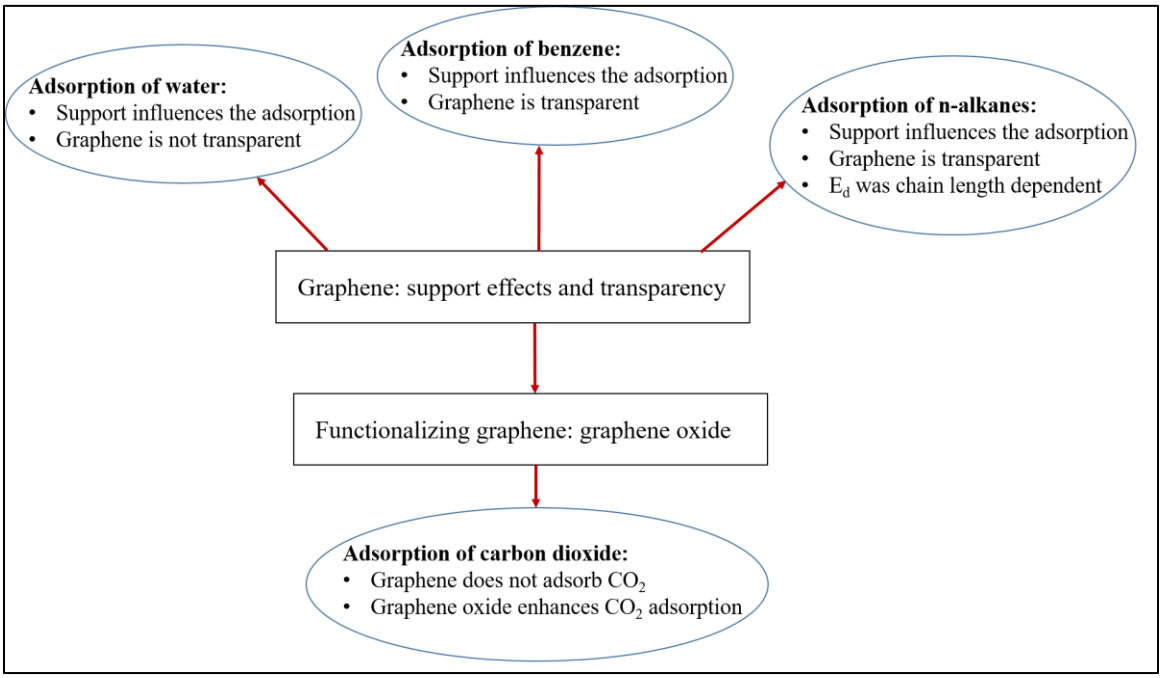

Figure 1. An illustration of the projects studied in this dissertation. The four main projects and the findings are shown within the circles

The second study (chapter 5) focuses on the adsorption of benzene on supported graphene (graphene/Ru(0001), graphene/Cu, and graphene/SiO_2) and the respective supports (Ru(0001), Cu, and SiO_2). Benzene is a prototype for carbon allotropes (fullerenes, graphite, and carbon nanotubes (CNTs)) and biomolecules (amino acids and nucleic acids). The interaction between benzene and graphene occurs through Π-Π stacking; supports can influence the degree of Π-Π stacking. The results of this study showed that the support affected the adsorption of benzene on graphene and also graphene was transparent to benzene adsorption on CVD graphene.

The third study (chapter 6) aimed at studying the n-alkane (n-butane, iso-butane, n-pentane, n-hexane, cyclo-hexane, and n-heptane) adsorption on supported graphene and the respective supports. This study is divided into three objectives: transparency of graphene, support effects of

graphene, and the chain length dependence of n-alkanes adsorption kinetics on graphene. Firstly, the kinetic and dynamic transparency of graphene was studied on graphene/Ru(0001) an Ru(0001) for n-butane adsorption. Graphene was, both, kinetically and dynamically transparent for n-butane adsorption. Secondly, the support effects were studied for n-pentane on graphene/Ru(0001), graphene/Cu, and graphene/SiO_2. The support affected the adsorption of n-pentane on graphene, i.e., binding energies increased as: graphene/SiO_2<graphene/Cu<graphene/Ru(0001). Thirdly, the chain length dependence of n-alkanes on graphene/Ru(0001) was investigated (chapter 6). The adsorption energies increased with increasing chain length.

Finally, the fourth study (chapter 7) describes the adsorption of carbon dioxide on Ru(0001), graphene/Ru(0001), and graphene oxide/Ru(0001). Carbon dioxide adsorbed on Ru(0001) and graphene oxide/Ru(0001), but did not adsorb on graphene/Ru(0001). Furthermore, the adsorption was enhanced on graphene oxide/Ru(0001) compared to Ru(0001) due to the active oxygen species; carbon dioxide adsorbed molecularly on, both, Ru(0001) and graphene oxide/Ru(0001) and no reaction products were formed on graphene oxide/Ru(001). The four studies of this dissertation were mainly focused on the adsorption of various small molecules on supported graphene, functionalized graphene (graphene oxide), and the respective supports.

Adsorption of molecules is a surface phenomenon compared to absorption, which is a bulk process. Molecules can adsorb on the surface through weak bonds or strong bonds. Surface science provides atomistic understanding of the adsorption of molecules on the surfaces of interest. All the studies in this dissertation were carried out on the surfaces under ultrahigh vacuum (UHV) conditions to provide an atomically clean environment. The intrinsic interactions of the molecules on the surface is mapped with various surface analytical techniques. Findings of this dissertation could serve as a model system for futuristic applications.

1.1. Surface chemistry

Atoms in the bulk of a solid or a liquid will experience a different force compared to the atoms at the surface. Atoms in the interior (bulk) are completely surrounded by other atoms and will experience a symmetrical force. In contrast, the atoms on the surfaces experience asymmetrical force due to the imbalances in the surrounding. The forces acting on an atom in the bulk and on the surface is shown in figure 2. The properties of the surface atoms are different than the properties of the atoms in the bulk due to the asymmetric force acting on the surface atoms. A study of the physical chemistry of such surface phenomenon is called "surface chemistry". Surface effects are tremendous important in applications such as wetting, heterogeneous catalysis, coatings, and sensors.[2-3] Thus, the in-depth understanding of the surface processes is important for various applications.

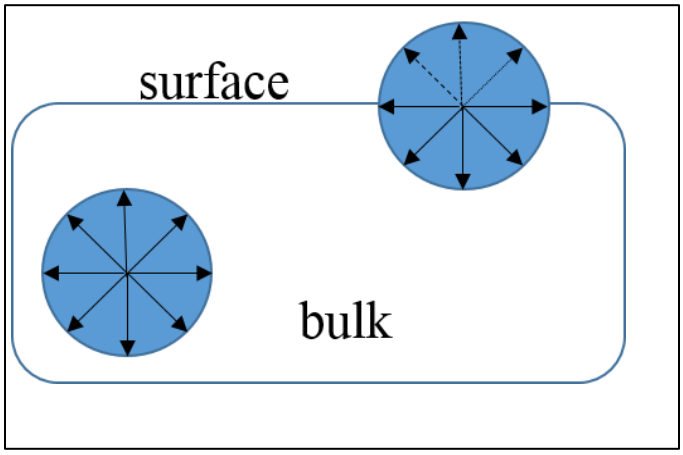

Figure 2. Symmetrical forces acting on the atom in the bulk and the asymmetrical forces acting on the atoms in the surface

1.2. Adsorption

Adsorption is a surface process where the adsorbing molecules are enriched at the surface due to the imbalanced forces acting on the surface. Adsorption can be classified as physisorption or chemisorption based on the nature of the forces that bind the adsorbates (adsorbing molecules) to the substrate (adsorbent).

Physisorption: physisorption occurs because of the weak interaction between the surface and the adsorbate. The weak interactions are due the van der Waals interactions. In addition, polarization of the adsorbates on the surfaces can also lead to a weak interaction and result in physisorption. Physisorption can be considered as a non-specific adsorption because no chemical bonds are formed between the adsorbates and the surface. Although the interaction between the adsorbate and the surface is very weak in physisorption the interaction between the adsorbates (lateral interactions) could be comparable to the strength of physisorption between the adsorbate and the surface.[2-5]

Chemisorption: rearrangement of electrons between the adsorbate and the surface with consequential formation of chemical bonds leads to chemisorption. Unlike physisorption, chemisorption is specific (directional) due to the bond formation; chemisorption can be considered as a chemical reaction on the surface. The binding energy of the chemisorption is usually above 50 kJ/mol.[2-5]

1.3. Surfaces

A surface can be homogeneous or heterogeneous. Binding of the adsorbate on the homogeneous surfaces will be uniform. In contrast, heterogeneity of the surface occurs due to defects, deformities, and irregularities. A heterogeneous surface is comprised of flat surfaces (terrace) and defects (steps, kinks, and ledges) as shown in figure 3. The regions around such

heterogeneities will be different and influence the adsorption of the incoming molecules. Techniques such as scanning tunneling microscopy (STM) and atomic force microscopy (AFM) can distinguish the surface heterogeneity.[5] In addition, thermal desorption spectroscopy (TDS) can be used to study the heterogeneity of the surface because of the appearance of multiple peaks with different binding energies. Overall, the nature of the surface influences the adsorption behavior of the adsorbates.

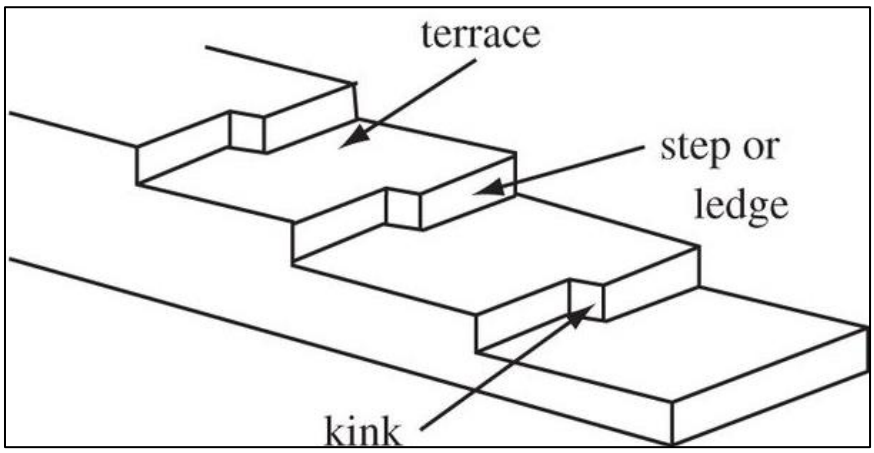

Figure 3. The heterogeneity of the surface[5]

1.4. Catalysis

Catalysis is a process where the catalyst accelerates the reaction. Catalysts can be classified as homogeneous catalyst and heterogeneous catalyst. In a homogeneous catalyst, both, the reactants and the catalyst are in the same phase; usually the homogeneous catalyst occur in liquid phase. In contrast, heterogeneous catalysis involves different phases of catalyst and the reactants. Heterogeneous catalysts are considered as the workhorses in the chemical industries; mostly the heterogeneous catalysts are present in solid phase- making the separation of catalyst and products easier.[6] The reactants in a heterogeneously catalyzed reaction could be in liquid or gas phase. The reactants can form bonds with the surface of the catalyst to facilitate the reaction and subsequently the products can be desorbed from the surface of the catalyst. For most of the bulk processes,

heterogeneous catalysts are preferred over homogeneous catalyst because the products can be easily separated from the catalyst. In a heterogeneously catalyzed reaction the reactants can be physisorbed or chemisorbed. Physisorbed reactants do not form a bond with the catalyst surface but can act as precursors for the incoming molecules to favor the reaction. In contrast, the chemisorbed reactants can form strong bonds with the catalyst surface to facilitate the reaction. Metal surfaces are commonly used heterogeneous catalyst due to the presence of various active sites on the surface.[6-7] However, recently metal-free catalysts are widely used in the chemical industry owing to the advantages of metal-free catalyst over metal catalyst. Metal-free catalysts are also known as "carbocatalyst"; sustainability and reduced toxicity of the carbocatalyst are the major reasons for the widespread use of carbocatalyst in the recent days. Carbon allotropes are the scientifically intriguing carbocatalysts. Lately, graphene and its derivatives are explored as metal-free catalysts. Remarkable success of such studies could be achieved by surface science approach, which provides fundamental understanding of such catalytic surfaces and catalytic reaction.[1,8]

1.5. Graphene and graphene oxide

A new era of carbon chemistry dawned with the discovery of graphene in 2004 at the University of Manchester by Geim and Novoselov.[8] Graphene is an allotrope of carbon composed of sp^2 hybridized carbons; the sp^2 hybridized carbon atom is attached to three nearest neighbors and forms a hexagonal planar structure as shown in figure 4. Graphene is a two-dimensional planar material with an atomic layer thickness and arranged into a honeycomb structure. Graphene forms a hexagonal lattice structure, where the unit cell has two carbon atoms. Graphene can be considered as a "mother material" for the other sp^2 nanocarbons (fullerene, graphite, and CNTs) because graphene serves as a platform structure to build the other allotropes.[8] Graphene has a high surface area (2600 m^2g^{-1}), which allows graphene to act as a support, specifically as a catalyst support, for

binding a large number of molecules. In addition, due to the sp^2 hybridization graphene is, both, chemically and mechanically stable; the Young's modulus of graphene is around 1TPa. Furthermore, the sp^2 hybridization provides an unhybridized p_z orbital, which results in high carrier mobility (10000 $cm^2V^{-1}s^{-1}$) and high thermal conductivity (≈4000 $Wm^{-1}K^{-1}$). Owing to these outstanding properties graphene is used in many areas such as medicine, engineering, and material sciences.[1, 8-10]

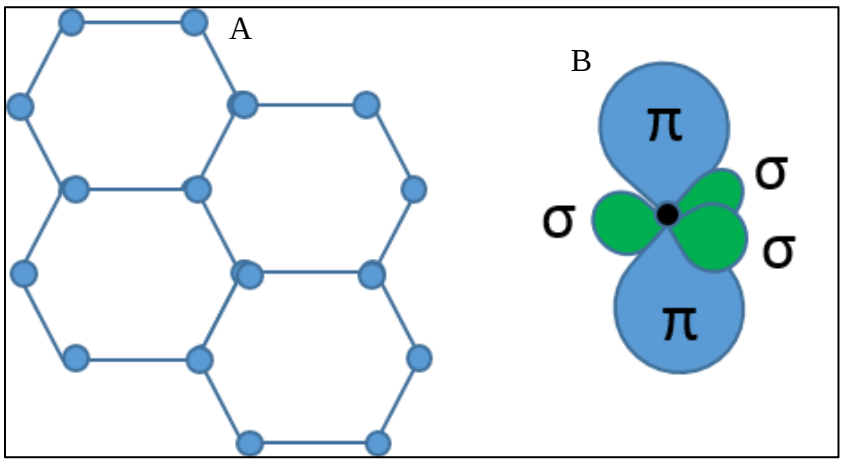

Figure 4. A. Hexagonal structure of graphene. B. sp^2 hybridized carbon with an unhybrdized p_z orbital to form a Π bond and 3-σ bonds attached to the nearest neighbors

Graphene is considered as the "heart of electronics" due to its high carrier mobility and high thermal conductivity. The first graphene based field effect transistors (FET) was reported in 2004 by Geim and Novoselov after the discovery of graphene. Later the efficiency of FET was enhanced by modifying the graphene surface to increase the bandgap and the efficiency of FET. In addition, graphene is also used in photovoltaics. High electrical conductivity, high surface area, and high optical transparency makes graphene a promising material in photovoltaics; graphene can be used as transparent electrode, due to the optical transparency, in solar cells to increase the power conversion efficiency. Besides, graphene is also used as a flame retardant due to high thermal conductivity and easy dissipation of heat. Not only in electronics but also graphene is used in

biomedical applications. The mechanical strength and the chemical inertness of graphene are utilized in implants.[1, 11-12] Furthermore, graphene is used as a transducer in biosensors to amplify the signal.[1] In summary, graphene is vastly used in many applications and it is constantly modified to tailor to the needs of the suitable applications.

Many applications utilize graphene on a support instead of a free standing graphene. Although free standing graphene is a stable structure most of the applications require placing graphene on a particular support; free-standing graphene is mainly used in liquid phase.[11-12] The supports for graphene can vary from metal, semi-conductors, and even ceramics. However, transition metals and semi-conductors are the most widely used supports for graphene based applications. A transition metal supported graphene is formed due to the interaction of graphene with the d-orbitals of the transition metals; interactions can be strong or weak depending on the adsorption mode of graphene on the metal. For example, the carbon atoms of graphene occupy the metal atop sites on Ru resulting in a strong interaction whereas the carbon atoms of graphene occupy the triangular hollow sites on Cu and result in weak interaction. The degree of interaction influences the interlayer spacing between graphene and the support.[9] The interlayer spacing between graphene and Ru is 2-3 Å as compared to the interlayer spacing with Cu, which is 3-4 Å due to the strong and weak interactions, respectively. In contrast to transition metal supports, graphene on semi-conductor supports such as SiC is formed by the thermal decomposition; unlike transition metals the interlayer spacing is lesser between the graphene and the semiconductor support.[9] The distinct interactions of graphene on various supports influences the properties of graphene.

1.5.1. Synthesis of graphene

Graphene can be synthesized using a top-down approach or a bottom-up approach. Top-down synthesis of graphene includes: exfoliation, chemical oxidation-reduction, and unzipping carbon nanotubes (CNTs). The bottom- up approach includes: epitaxial growth of graphene on SiC, vapor deposition (chemical vapor deposition, CVD and physical vapor deposition, PVD), and green synthesis of graphene.[13]

Exfoliation: graphite, is composed of many single layers, which are held by weak van der Waals interactions. Exfoliation involves removing the weak interactions between the adjacent layers of graphite by means of mechanical agitations; 3D graphite is converted to 2D graphene through exfolitation. Ultrasound and ultra-sonication are the most common methods used to disrupt the van der Waals interactions. Although sonication results in single layers of graphite (graphene) the individual graphene flakes have to be stabilized before they can be used in subsequent applications. Organic solvents (CPO, NMP, DMF, TBA, SDBS) act as exfoliant to stabilize the individual graphene flakes. The choice of solvent is critical as the surface energy of solvents have to be comparable to the surface energy of graphene; the comparable surface energies will facilitate in stabilizing the individual flakes through coulombic repulsive interactions. The adsorbed surfactant can be subsequently removed by vacuum evaporation leading to individual graphene flakes.[14-15]

Chemical oxidation-reduction: graphite oxide can be used as a precursor for the synthesis of graphene. A famous Hummers' method is used to convert graphite to graphitic oxide using an anhydrous oxidation mixture (con. H_2SO_4, $NaNO_3$, and $KMnO_4$). The oxidation not only introduces sp^3 hybridized carbons, but also it increases the interlayer space between the adjacent layers in graphite; a further sonication can result in oxygen functionalized individual layers of

graphite, which are called as graphene oxide. To obtain graphene from graphene oxide the oxygen functional groups are reduced using reducing agents such as hydrazine, $LiAlH_4$, and $NaBH_4$.[16]

Epitaxial growth of graphene on SiC: SiC is a semiconductor, which supports graphene formation through thermal decomposition. At 1150 ˚C Si sublimes and during a subsequent increase in temperature to 1350 ˚C the carbon rearranges into a honeycomb lattice to form a monolayer graphene. Temperature plays an important role in the number of layers of graphene; at temperatures between 1400 ˚C and 1600 ˚C bilayer and multilayer graphene can form and subsequently result in crumpled graphene at higher temperatures (>1700 ˚C).[17]

Unzipping of CNTs: graphene can be synthesized by unzipping the CNTs (single-walled CNTs and multi-walled CNTs). Oxidative treatment of CNTs with a mixture of H_2SO_4 and $KMnO_4$ unzips the CNTs longitudinally and introduces oxygen functionalities on graphene. A subsequent reduction with reducing agents can produce oxygen-free graphene. However, this method introduces pronounced structural damages due to the oxidative unzipping of CNTs. Alternatively, heating up CNTs in the presence of potassium at 250 ˚C cleaves the CNTs longitudinally and results in a defect-free (pristine) graphene. Besides, when multi-walled CNTs are used as starting materials, intercalating agents such as Li-NH_3 and subsequent exfoliation are used to produce graphene sheets. In addition, metal nano particles can also be used as catalysts to unzip the multi-walled CNTs to form graphene sheets.[13]

Chemical and physical vapor deposition (CVD and PVD) of graphene: Chemical and physical vapor deposition involves the formation of graphene through chemical and physical processes, respectively. Transition metals (Ni and Cu) are used as catalysts in CVD process. Carbon dissolves in the transition metals, which have grain boundaries; the grain boundaries act as nucleation center for the graphene growth. Once the graphene is formed at 900-1000 ˚C it can

be transferred to any substrate of interest. Transfer process involves coating the graphene with poly- methylmethacrylate (PMMA) or poly dimethyl siloxane (PDMS). Once the graphene is coated the transition metal can be etched with acidic treatment followed by dissolution of PMMA or PDMS coating with acetone.[1] In contrast to CVD, PVD process is done under vacuum condition, where the carbon source is sublimed under vacuum. The substrate should have active sites such as steps and terraces to dissociate the carbon source. Once the carbon source is dissociated into individual carbon, it rearranges into graphene at temperatures between 900 and 950 ˚C. The graphene formed in PVD process is pristine (crystalline) as it does not involve any chemical processes such CVD, which results in high quality graphene.[17-18]

Green synthesis of graphene: Plant based materials are sustainable sources, which can be used as precursors for graphene synthesis.[19] Furthermore, agricultural by-products are abundant in nature and are often utilized as feedstocks. Converting such agricultural by-products into two-dimensional materials like graphene will be a promising route due to the sustainability of agricultural by-products. Graphene has been synthesized from agricultural by-products such as rice husks,[20] wheat brans,[21-22] coconut shells,[23] and distillers' dried grains.[24] The high content of the organic carbon in these compounds are firstly activated with chemical agents, mainly $ZnCl_2$. Secondly, the activated matrix is carbonized at high temperatures (800-900 ˚C). Finally, a prolonged exposure at high temperature convert the agricultural by-products into graphene- by rearranging the carburized phase into graphene.[25-26]

1.5.2. Graphene as a catalyst

Metals are well-known and widely used catalytic surfaces. Recently, a metal-free catalytic system has been a new field of interest in the catalytic industry; carbon based materials are the potential metal-free catalyst. Carbon based materials are inexhaustible and less toxic compared to

metal catalysts. The dawn of graphene has paved its way as a carbocatalyst in the catalytic process. Graphene has a high surface area, which can act as a catalytic support to disperse catalytic nanoparticles.[27] Nevertheless, pristine graphene is a catalytically inert material. However, the defects and the zig-zag edges of the graphene can provide active sites and dangling bonds for catalytic activity. [28-29] Furthermore, covalent functionalization of graphene can provide active sites for catalytic activity; oxidation of graphene is one of the mostly studied surface for catalytic activity. Therefore, graphene and graphene oxide can be promising carbocatalyst in the catalytic industry.

1.5.3. Graphene oxide

Graphene can be converted to graphene oxide through high energy oxygen atoms. The oxidation process converts sp^2 hybridized carbon of graphene to sp^3 hybridization to accommodate oxygen groups. A complete oxidation of graphene (monolayer graphene oxide) results in a C:O 2:1 ratio because the two carbon atoms in a unit cell of graphene accommodates one oxygen atom.[30] Graphene oxide is a poly dispersed structure with various oxygen functionalities. The structure of graphene oxide was elucidated by different groups as shown in figure 5. Hofmann proposed that the basal plane of graphene oxide is exclusively composed of epoxy groups. In contrast, Ruess proposed that the graphene oxide is composed of, both, hydroxyl and epoxy groups. A recent study by Lerf-Klinowski showed that the graphene oxide is composed of hydroxyl, epoxy, and carbonyl groups.[31] To date an exact structure of graphene oxide is not reported in the literature except the evidence for the reactive oxygen species on graphene oxide. Graphene oxide can synergically enhance the catalytic activity due to the high surface area of graphene scaffold and the reactive oxygen species to serve as an efficient carbocatalyst.[31-32]

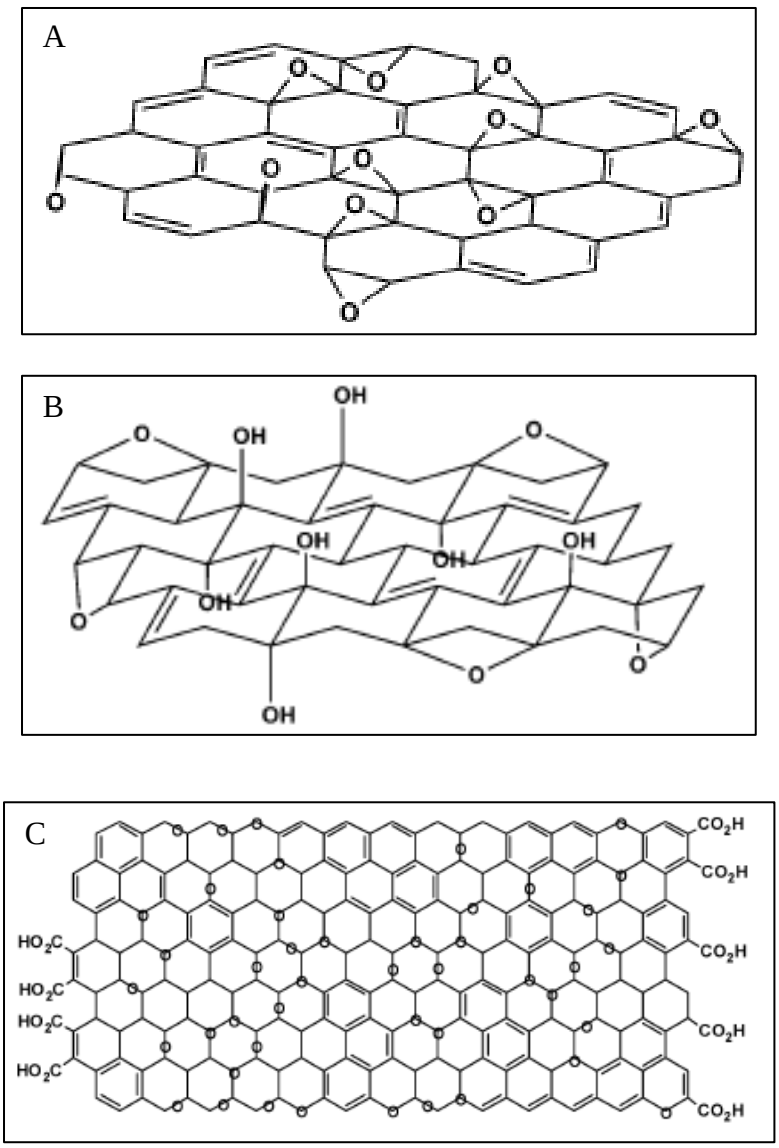

Figure 5. A. Structure of graphene oxide proposed by Hofmann. Graphene oxide is exclusively composed of epoxy groups. B. Structure of graphene oxide proposed by Ruess, where the graphene oxide is composed of, both, epoxy and hydroxyl groups. C. Structure of graphene oxide proposed by Lerf-Klinowski. Graphene oxide is composed of epoxy, hydroxy, and carbonyl groups[31]

Oxygen functionalities of graphene oxide can be studied by UV-visible spectroscopy, Fourier Transform Infrared Spectroscopy (FTIR), high resolution-XPS, and Raman spectroscopy. As depicted in figure 6, the UV-visible spectroscopy shows a clear difference between graphene and graphene oxide. Graphene has more Π- Π conjugation due to sp^2 hybridized carbon, compared

to graphene oxide. Higher degree of conjugation requires less energy for Π- Π* transition, which leads to increased wavelength in graphene (λ= 265 nm) compared to graphene oxide (λ= 235 nm).[33]

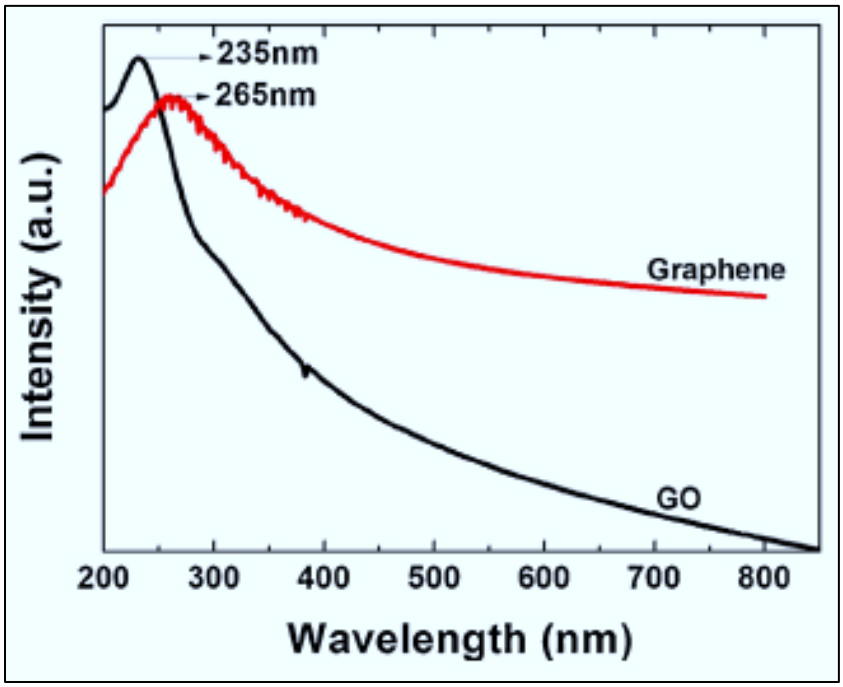

Figure 6. UV-visible spectrum for graphene and graphene oxide[33]

In contrast to UV-visible spectroscopy, both, FTIR and high resolution- XPS will allow to identify the chemical environments of the oxygen functionalities. FTIR of a graphene oxide is shown in figure 7. The peak at 3050- 3800 cm^{-1} corresponds to the –OH groups, peak around 1700 cm^{-1} corresponds to –COOH group, peak around 1600-1650 cm^{-1} corresponds to ketonic (C=O) species, and peak around 1230-1330 cm^{-1} corresponds to epoxide groups. In addition, sp^2 aromatic carbon is seen at 1500-1600 cm^{-1}; pristine graphene surface should show only the sp^2 aromatic carbon stretch in FTIR.[34]

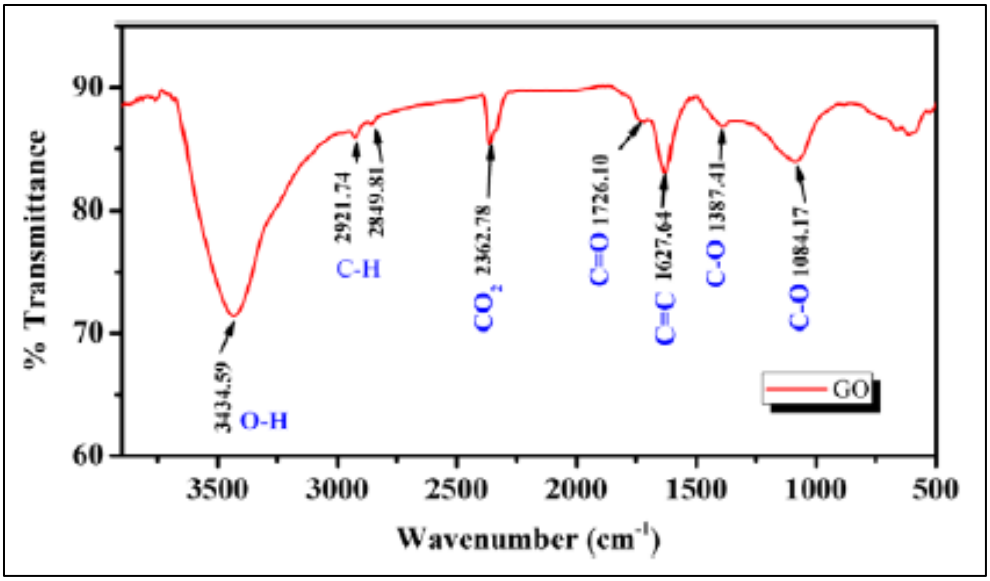

Figure 7. FTIR of graphene oxide[34]

A high resolution XPS of graphene and graphene oxide is shown in figure 8. A pristine graphene should not show any oxygen functionalities. However, the additional shoulder peak at 288.8 eV shows there is some oxygen residue on the surface. Peaks at 284.6 eV, 286.6 eV, and 288.5 eV correspond to sp^2 carbon, epoxy, and carboxyl groups, respectively. The sp^2 hybridized peak is intense in graphene compared to graphene oxide because graphene has more sp^2 hybridized carbon.[33,35] High resolution-XPS can be used to distinguish the oxygen functionalities on the graphene oxide surface. Unlike, FTIR and high resolution XPS, Raman spectroscopy characterizes the presence of oxygen functionalities in graphene oxide by considering the I_D/I_G ratio. A pristine graphene should have less defects, hence the intensity of D-band should be less resulting in less I_D/I_G. However, when oxygen functionalities are present the intensity of D-band will increase; presence of oxygen introduces sp^3 hybridized carbon.[36] Therefore, various techniques can be used to characterize the oxygen functionalities in graphene oxide.

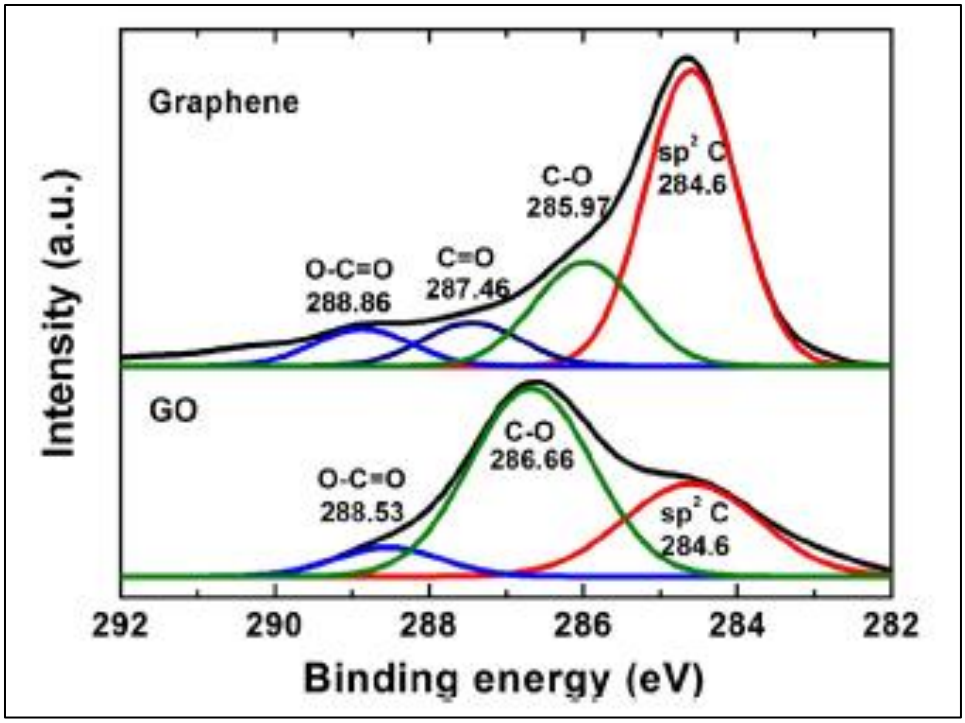

Figure 8. High resolution-XPS for graphene and graphene oxide[33]

In this dissertation, AES and XPS were used to characterize the graphene oxide/Ru(0001) sample and the findings are shown in chapter 3 (section 3).

CHAPTER 2. EXPERIMENTAL TECHNIQUES

2.1. Ultrahigh vacuum technique (UHV technique)

Ideal vacuum can be defined as volume devoid of matter. Real vacuum is when the volume is filled with a gas at any pressure under atmospheric pressure (10^3 mbar). Based on the pressure (mbar units), vacuum can be classified as: low vacuum (3.3x10 to 10^3 mbar), medium vacuum (10^{-3} to 3.3x10 mbar), high vacuum (10^{-9} to 10^{-3} mbar), ultrahigh vacuum (10^{-12} to 10^{-9} mbar), and extra ultrahigh vacuum ($\leq 10^{-12}$ mbar).[3] Different levels of vacuum are achieved by various pumps. Roughing pumps, turbomolecular pumps (turbo pumps), diffusion pumps, and ion getter pumps are mainly used in generating vacuum by removing gas molecules. The reduction in pressure leads to an increased mean free path (λ). Mean free path is the distance travelled by molecules between collisions; mean free path and pressure are inversely proportional ($\lambda \alpha 1/P$, where P is the pressure). At low pressures (vacuum level) λ will be large, which vastly increases the distance between collisions of the molecules to achieve a molecular flow. Although different levels of vacuum can be generated, ultrahigh vacuum (UHV) becomes predominantly important for surface science studies.

Surface science studies focus on studying various surfaces under atomically clean conditions. Preparation of atomically clean surface and maintaining the surface, uncontaminated, for a prolonged period requires UHV. The inception of UHV technology has proliferated the field of surface science with a variety of surface analytical techniques (LEED, AES, TDS, and XPS). The surface analytical techniques use low energy electrons and ions, which need large λ to ensure no scattering occurs before reaching the detector. UHV fulfills the requirements of atomically clean condition and molecular flow environment to perform surface science studies. A schematic representation of a general UHV set-up is shown in figure 9. The proceeding section describes the

UHV system available in North Dakota State University (NDSU), Fargo, which was used to carry out the experiments described in this dissertation.

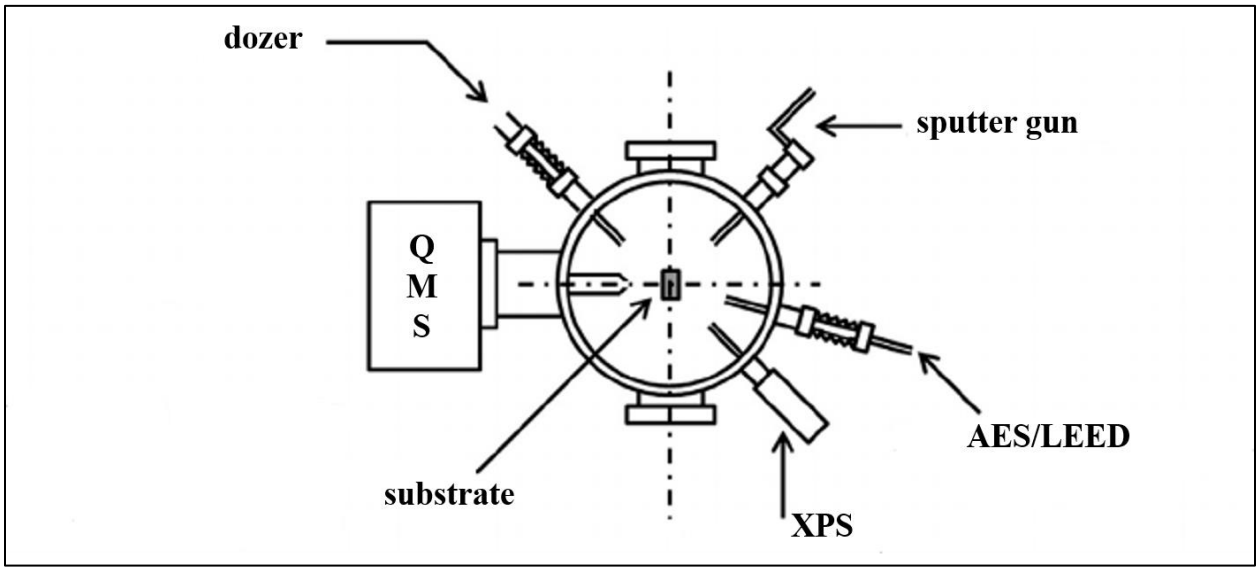

Figure 9. Schematic of a UHV set-up

2.1.1. UHV system at NDSU

There are two UHV systems available at the Department of Chemistry, NDSU to study the fundamental properties of the surfaces. One system is called a TDS chamber (kinetics system) and the other is called a molecular beam scattering chamber (dynamics system). Both systems are built with stainless material. Stainless steel has a low vapor pressure (avoid desorption), can withstand high temperatures (chamber reaches around 200 ˚C during baking), and is corrosion resistance. The chambers have multiple flanges mounted by a plethora of bolts and are sealed with metal gaskets to ensure no permeation of gas from atmosphere to the vacuum chamber. The pressure of both systems are monitored by Pirani gauges and ion gauges to ensure that the UHV is maintained.

2.1.1.1. TDS chamber

The TDS chamber for kinetics experiments has one roughing pump (Leybold), two turbomolecular pumps (Varian), and an ion getter pump with a back-up battery. Figure 10 shows

the TDS chamber at NDSU. The pumps generate a vacuum of $8x10^{-10}$ mbar. The chamber is housed with various surface analytical techniques: A combined low-energy electron diffraction (LEED) and an Auger electron spectroscopy (AES) from SPECS, ErLEED 300D, and two quadrupole mass spectrometers (SRS RGA 100 and SRS RGA 300). In addition, multiple leak valves are attached to the chamber to dose gases and liquids of interest. A home-made oxygen dozer is attached to the chamber to dose atomic oxygen. A sputter gun (SPECS) is available for sample cleaning process. The sample position can be manipulated with a XYZ manipulator (McAllister) where the sample can also be rotated (θ=360˚) with a stepper motor. The system has two gate valves (VAT) to protect the chamber during a power failure. The gate valves will close during a power failure and the ion-getter (with a back-up battery) will maintain a vacuum, for several hours.

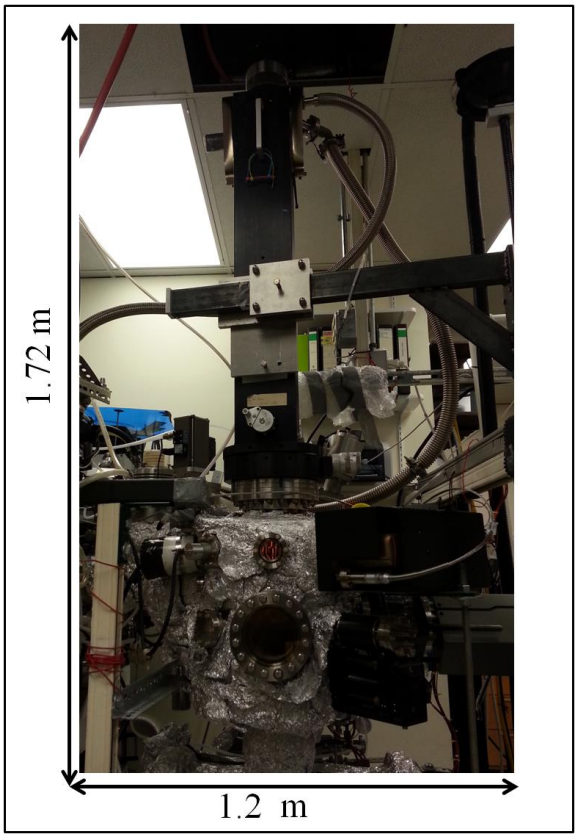

Figure 10. TDS chamber at NDSU

2.1.1.2. Beam chamber

This chamber has two major components: main chamber (scattering chamber) and a beam chamber as shown in figure 11. Both chambers are connected by a buffer chamber. The main chamber has two roughing pumps (Leybold), three turbo pumps (Varian), and one ion getter pump (Varian) to generate a pressure of $4x10^{-10}$ mbar. The main chamber is housed with AES and X-ray photoelectron spectroscopy (XPS), from Perkin Elmer, attached to a cylindrical mirror analyzer (CMA). In addition, there are two quadrupole mass spectrometers (SRS RGA 100 and SRS RGA 300). The beam chamber is pumped with two diffusion pumps (VHS- 10 at 3000 l/s pumping speed and VHS-6 at 600 l/s) and backed by a booster pump (D25B/WSU500) and subsequently a roughing pump (Leybold). The nozzle source for beam has a nozzle head to fit a Pt/Ir nozzle plate with a 20 μm aperture.

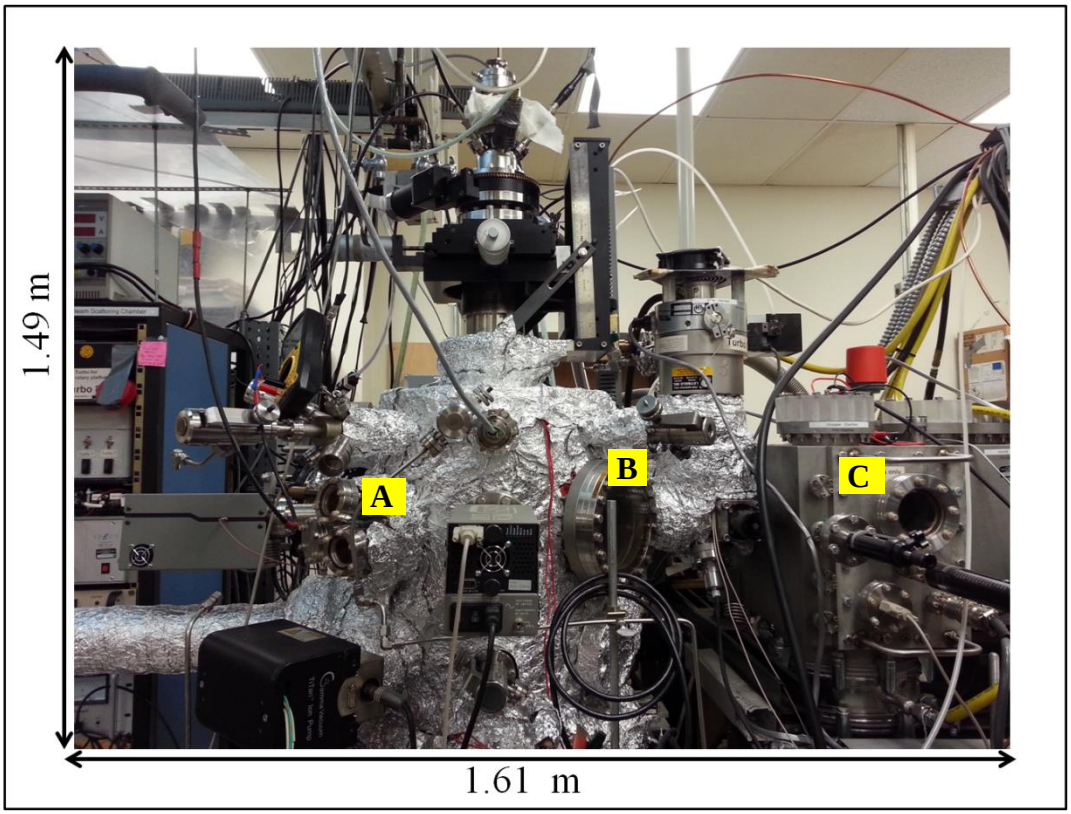

Figure 11. Beam chamber at NDSU: A. main chamber, B. buffer chamber, and C. beam chamber

2.1.1.3. Bake-out of chambers

Bake-out is essential when the chamber is exposed to the atmosphere where the water can be adsorbed on to the inner walls of the chamber. The chambers are vented during a sample transfer process or during a power failure. The chambers are wrapped with heating belts to ensure even heating of the chamber. In addition, surface heaters are also used for baking process. The chambers are baked to around 150 ˚C for 48 hours to achieve UHV.

2.1.1.4. Sample handling and mounting

A picture of a sample holder is shown in figure 12. The sample holder is made of stainless steel and it is connected to the manipulator. The size of the samples used usually amounts to 10x10x1 mm. The sample is spot-welded to two of four Mo-pins; one of the pins is also connected to high voltage. A thermocouple is attached to the sample to monitor the surface temperature. The thermocouple is made of two different metals Cr-Ni connected to each other and the temperature can be calibrated by applying a voltage (Seebeck effect). Filament (W-filament, diameter: 0.25 mm from Goodfellow) is spot-welded to the remaining two Mo pins at the back of the sample. The heating of a sample is carried out by applying a high voltage (0.5-1 kV) and resistively heating the W-filament. The filament produces electrons during heating, which accelerates towards the sample due to high voltage. The movement of electrons creates a current to subsequently heats up the sample. Temperature of the sample can be controlled by applying a voltage to the W-filament. The upper side of the sample holder is attached to the sample holder directly. The four Mo pins on the upper side are isolated with heat-shrink tubes to avoid contact in the presence of l-N_2. Sample is cooled to around 90 K with l-N_2 and it can be further cooled to about 85 K with He-bubbling.

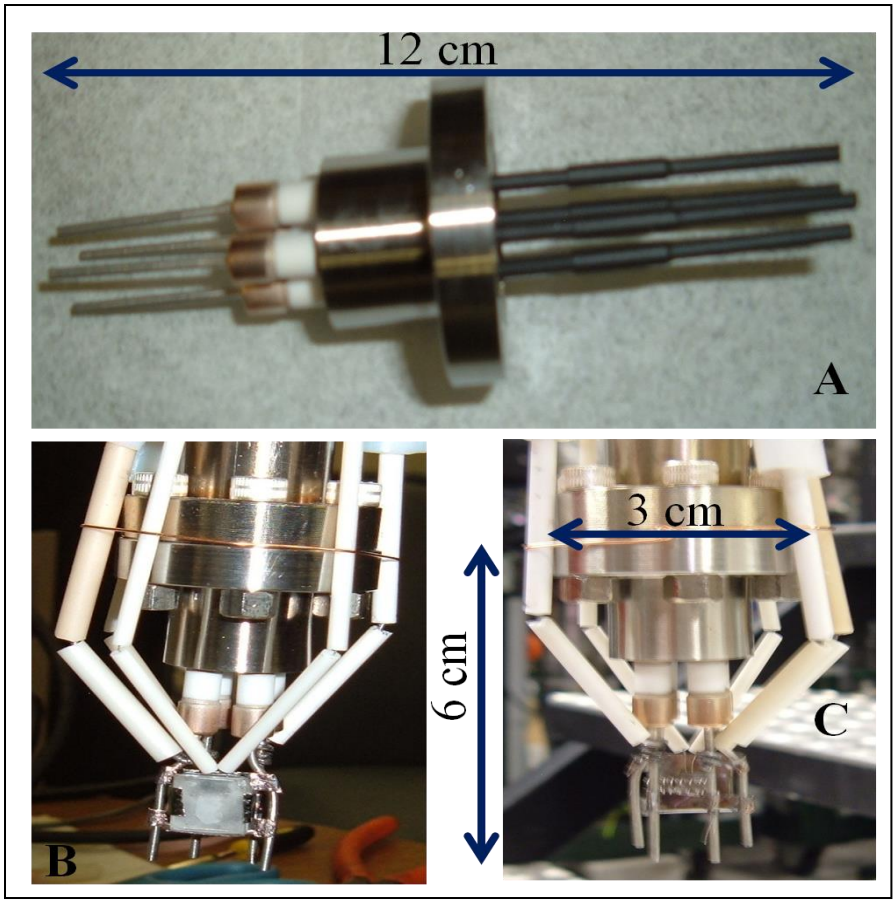

Figure 12. A Sample holder with four Mo-pins at the bottom and the tops. The bottom pins are isolated with ceramics. The top pins are isolated with heat-shrink tubes. B. Sample attached to two of the four Mo-pins. High voltage is attached to the left pin and the thermocouple is spot-welded on the sample. C. Back-side of the sample where W-filament is attached to both pins. All the connections are isolated with Teflon tubing to avoid short-circuit

2.2. Thermal desorption spectroscopy (TDS)

Thermal desorption spectroscopy (TDS) is used in studying the adsorption kinetics in surface science. The surface kinetic process is studied by monitoring the desorbed molecules in the gas phase, which are adsorbed on to the surface of interest. The experimental set up of the TDS is shown in figure 13. The experimental requirements to study the adsorption kinetics are,

1. Leak valve: this allows to dose the gas of interest into the UHV chamber. The gas dosage is quantified in Langmuir (L) units, where 1L= $1x10^{-6}$ mbar/second. Ideally, dosing 1L gas of interest should lead to a 1 monolayer (1 ML) coverage, provided that the adsorption probability

is 1; in most cases, a monolayer coverage is observed at several Langmuir dosages. The final pressure of the gas that adsorbs on to the surface is a sum of background pressure and the dosed pressure ($P_{final}=P_{background}+ P_{dose}$); the $P_{background}$ ($1x10^{-10}$ mbar) is smaller than P_{dose} (mbar), therefore the P_{final} can be considered as the exact dose of the gas pressure of interest.

2. Heating the sample: the sample is mounted in the manipulator, which is attached to the UHV chamber (described in section 2.1). The sample is, usually, ramped linearly, $T_{(t)}= T_0+\beta t$, where $T_{(t)}$ is the final temperature, T_0 is the initial temperature, β is the heating rate, and t is the time. The heating is carried out by resistively heating the sample through a W-filament and monitoring the temperature of the sample using a thermocouple, which is spot-welded on the sample. When the sample is heated, the thermal energy gained will facilitate the breaking of bonds between the adsorbates and the surface and eventually the adsorbates will desorb from the surface.
3. Detector: the desorbed molecules from the surface, due to a temperature ramp, can be monitored by a Quadrupole Mass Spectrometry (QMS). The QMS aids in detecting a mass-selective measure of the pressure rise. The QMS is composed of three parts (ion source, quadrupole analyzer, and electron multiplier), which is depicted in figure 14. The W-filament in the QMS is electrically heated, which produces free electrons. The free electrons accelerate between filament and the grid with subsequent ionization, which occurs between the grid and the aperture. The quadrupole analyzer is composed of 4 symmetrically arranged cylindrical rods, which are electrically connected. The analyzer allows the separation of the particles by the mass to charge ratio (m/e). The detected particles are passed through an electron multiplier (channeltron) - to obtain the multiplied signal.[37]

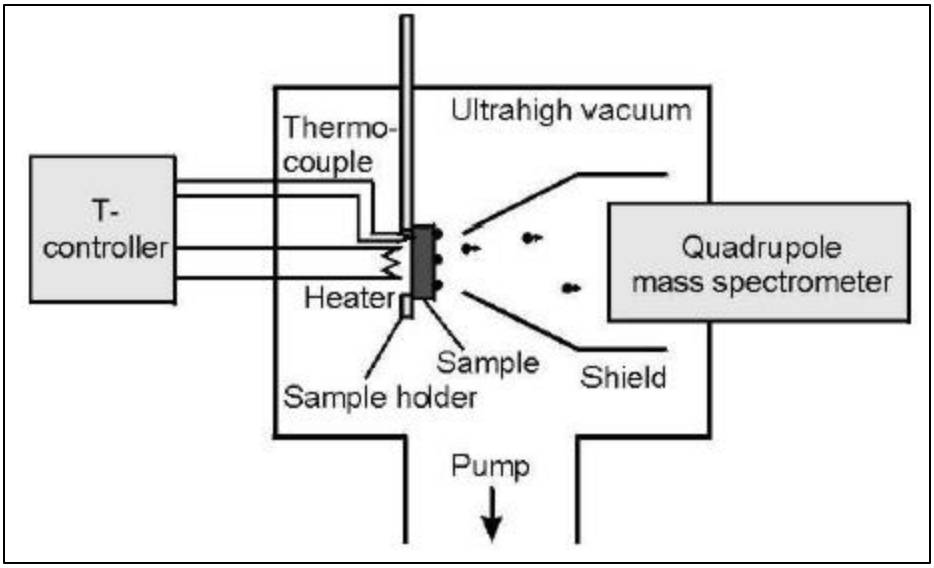

Figure 13. Schematic representation of TDS

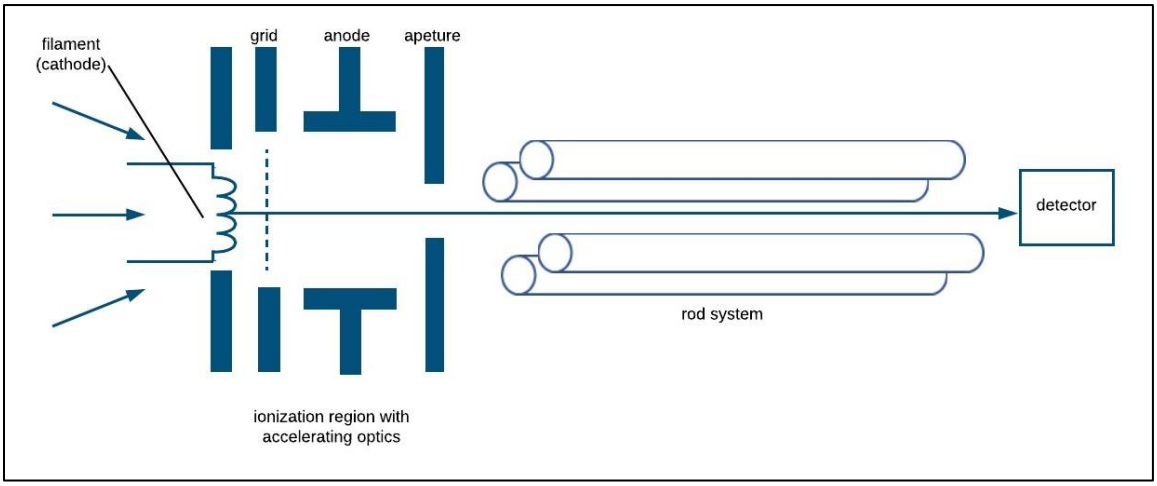

Figure 14. Components of QMS[37]

The TDS yields a variety of information: surface coverage, number of binding sites, desorption temperature, reaction order, and desorption energy (Edes). The surface coverage can be obtained by integrating the TDS peak. The number of binding sites can be obtained by considering the number of peaks in TDS. As a literature example, figure 15 shows benzene adsorption on CNTs.38 The CNTs have three different binding sites: internal, groove, and external, which are evident in TDS. The desorption peak at high temperature is assigned to the interior (A)

and the desorption peak at low temperature is assigned to the exterior (C). The peak assignments are based on the binding strength of the benzene molecule at different sites. In addition, a condensation peak (D) is seen around 145 K due to the condensation (multi-layer) of benzene on CNTs. TDS allows, both, qualitative and quantitative analysis in surface science.

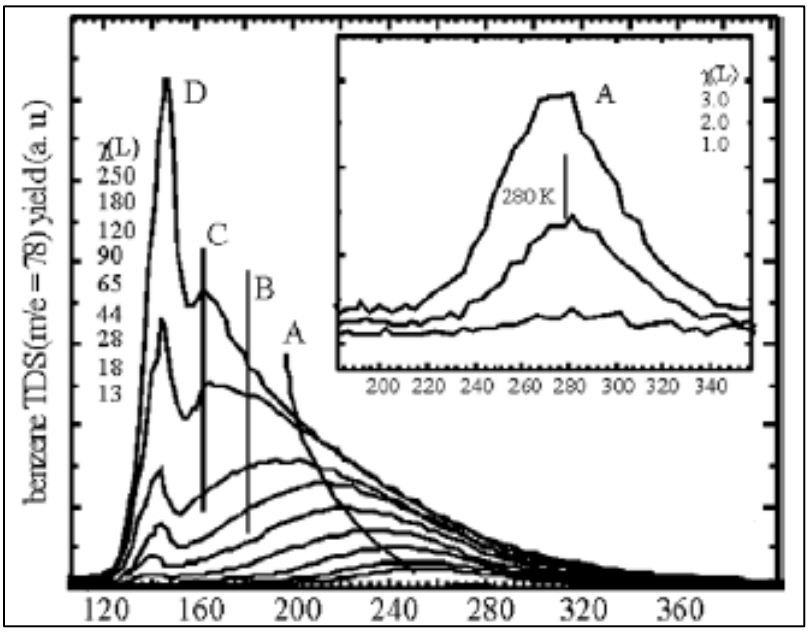

Figure 15. Adsorption of benzene on CNT. Three different binding sites are evidenced. Peak A corresponds to interior, peak B corresponds to groove, and peak C corresponds to the external sites. In addition, a condensation peak is seen at 145 K, which is designated as peak D[38]

The reaction order can be determined by the shape of the TDS curve. Simulated TDS curves for zeroth, first, and second order are shown in figure 16. The zeroth- order shows an alignment of the leading edge and an increasing shift in desorption temperature with increasing coverage. This behavior is seen in molecules where the intermolecular interactions are strong (ex: hydrophobic interactions of water on graphene; strong intermolecular interaction between water molecules), which leads to a common leading edge. Furthermore, the increase of desorption temperature is attributable to increasing coverage and eventual multilayer formation. In contrast to zeroth-order, first-order kinetics has an asymmetric peak with a non- changing desorption temperature due to the coverage independent behavior. A first order desorption is observed for non-dissociative

molecular adsorption and desorption. However, the exceptional behavior is seen in first-order kinetics, where the desorption temperature can decrease with increasing coverage; repulsive lateral interaction of the adsorbate molecules can lead to a destabilization of the adsorbates, which can result in lowering of the desorption temperature with increasing coverage. Besides, a second-order kinetics is seen for molecules, which dissociate on the surface and desorb and thus the desorption temperature decreases with increasing coverages. Overall, the peak shape in TDS allows one to determine the reaction order.

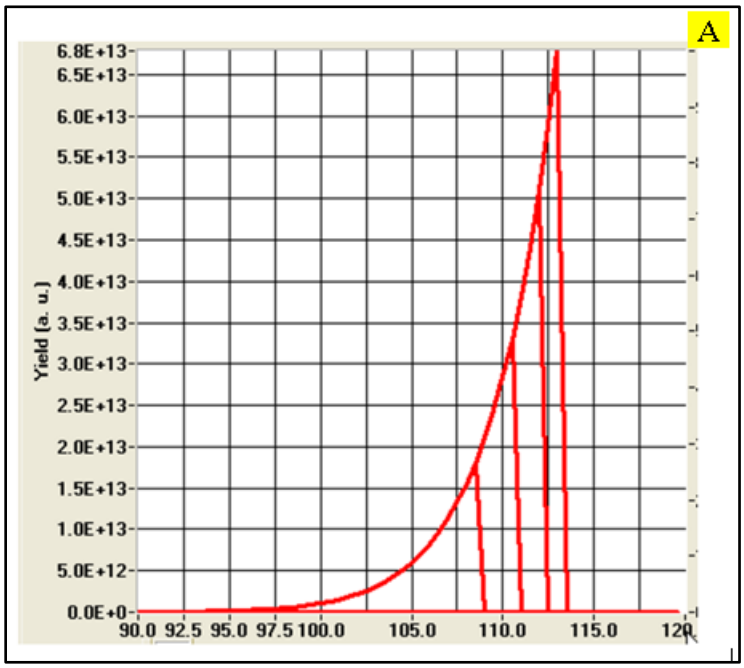

Figure 16. A. Zeroth-order kinetics with common leading edges and increase in desorption temperature with coverage. B. First-order kinetics shows an asymmetric peak and a constant desorption temperature with increasing coverage. C. Second-order kinetics shows a decrease in desorption temperature with increasing coverage

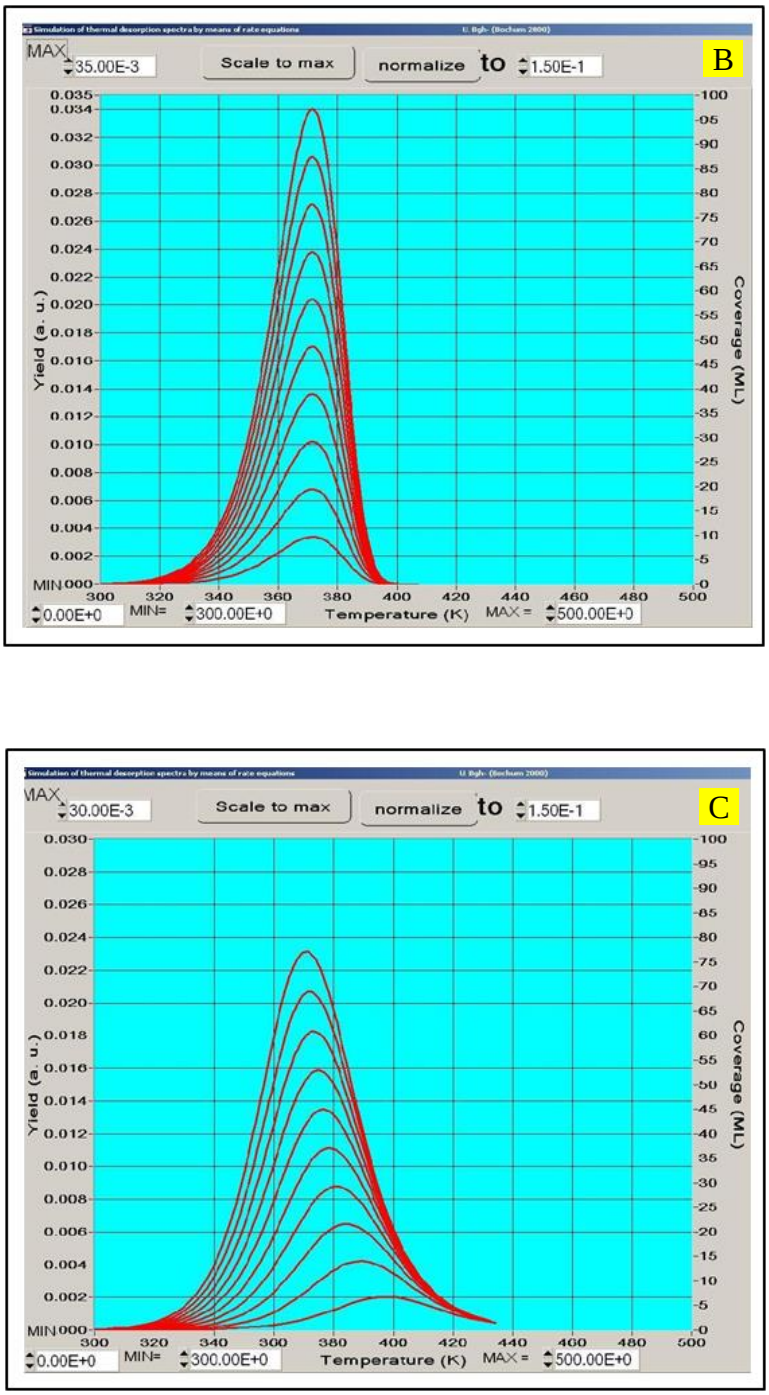

Figure 16. A. Zeroth-order kinetics with common leading edges and increase in desorption temperature with coverage. B. First-order kinetics shows an asymmetric peak and a constant desorption temperature with increasing coverage. C. Second-order kinetics shows a decrease in desorption temperature with increasing coverage (continued)

The TDS can be used in calculating the binding energies using one of the, most commonly used, following methods,[37]

1. Complete analysis
2. Leading edge analysis
3. Redhead analysis
4. Varying heating rate analysis

Complete analysis:

The complete analysis is done as following,

rate of desorption,

$$-d\theta/dt = k_d\theta^m \quad (1)$$

heating rate,

$$\beta = dT/dt \quad (2)$$

substituting (2) in (1)

$$-d\theta/dT = k_d\theta^m/\beta \quad (3)$$

Arrhenius equation

$$k_d = \nu e^{-Ea/RT} \quad (4)$$

substituting (4) in (3)

$$-d\theta/dT = \nu e^{-Ea/RT}\theta^m/\beta \quad (5)$$

if, $-d\theta/dT = r$, then

$$r = \nu e^{-Ea/RT}\theta^m/\beta \quad (6)$$

taking the natural logarithm of equation 6 yields in,

$$\ln r = \ln(\nu\theta^m/\beta) - Ea/RT \quad (7)$$

For each coverage (θ), a plot of ln r vs 1/T can be plotted and the gradient will result in Ea (desorption energy) for each coverage. The pre-exponential factor (ν) can be calculated from the intercept because the coverage (θ) and the order of the reaction (m) can be determined from the TDS curves. Although this method is accurate, the method is not used widely due to its complexity.

Leading edge analysis:

This method is used for the TDS curve at the leading edge, which is depicted in figure 17. The desorption energy (Ea) is calculated using equation 7. However, the signal to noise ratio (S/N) is very low at the leading edges. Therefore, this method is not usually used in calculating the desorption energies.

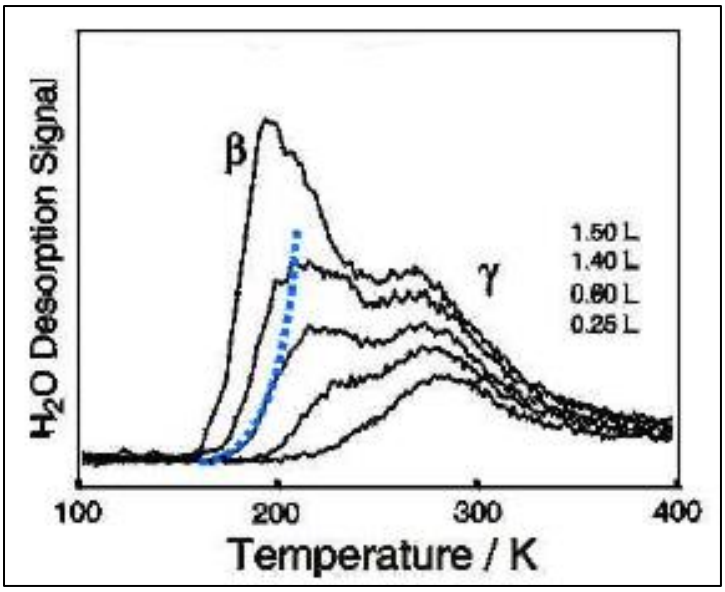

Figure 17. TDS curve where the leading edge is showed by dotted lines[39]

Redhead analysis:

Using equation 5, $-d\theta/dT = \nu e^{-Ea/RT}\theta^m/\beta$, the Redhead analysis can be done as follow. When $T=T_p$, where T_p is the maximum desorption temperature the rate of desorption also reaches a maximum giving $d^2\theta/dT^2= 0$. Therefore, the equation 5 can be written as,

$$E_a/RT^2 = \nu/\beta\ m\theta^{m-1}e^{-Ea/RT} \quad (8)$$

Redhead assumes first-order desorption, hence m=1, which leads to,

$$E_a/RT^2 = \nu/\beta\ e^{-Ea/RT} \quad (9)$$

Using the natural logarithm,

$$\ln (E_a/RT) = \ln (\nu T/\beta) - E_a/RT \quad (10)$$

and,

$$E_a = RT[(\ln (\nu T/\beta)) - \ln (E_a/RT)] \quad (11)$$

However, it is assumed that $\ln (E_a/RT) = 3.46$ and thus

$$E_a = RT[(\ln (\nu T/\beta)) - 3.46] \quad (12)$$

The desorption energy can be calculated by assuming the pre-exponential factor (ν)= 10^{13} s^{-1} for small molecules. This method is widely used, however the method has drawbacks due to the assumptions made.

Varying heat rate analysis:

TDS usually involves a linear heating ramp. However, the heating rate can be varied in order to determine the desorption energy. Rearranging the equation 9, $Ea/RT^2 = \nu/\beta\ e^{-Ea/RT}$ results in,

$$\beta/T^2 = (\nu R/E_a)\ e^{-Ea/RT} \quad (13)$$

The natural logarithm of equation 13 gives,

$$\ln (\beta/T^2) = \ln (\nu R/E_a) - E_a/RT \quad (14)$$

Change in heating rate (β) results in a negative slope, which gives the desorption energy. Although this method is reliable, it is not widely used due to the inconvenience in changing the heating rate.

TDS is an inevitable technique in most of the surface science studies, which could be considered as the “beauty and the beast” technique of surface science. The beauty lies in the fact

that the experiment is easier to carry out and the beast is due to the complexity in the data interpretation. Therefore, TDS can be extensively used in extracting information about the surface-adsorbate interactions.

2.2. Molecular beam scattering

A beam of molecules (atoms) can collide with a surface resulting in elastic or inelastic scattering. Elastic scattering occurs when the impinging molecule does not lose its energy (no energy exchange between molecule and surface) and scatter with the same amount of energy. Diffraction is a most common elastic scattering; the molecule should lose energy to stick to the surface. The elastic scattering does not result in energy transfer, between the surface and the adsorbate, where the incident molecule desorbs into the gas phase without an energy loss. In contrast to elastic scattering, the inelastic scattering results in an energy transfer between the molecule and the surface. Depending on the loss of energy, the inelastic scattering can be classified as: direct inelastic scattering and trapping. Direct inelastic scattering occurs when a molecule interacting with a surface either loses or gains energy and returns to the gas phase. Trapping can occur when the molecule loses enough energy to be trapped into the surface which eventually can desorb. However, the trapped molecules can also result in sticking to the surface if the molecule forms a bound state with the surface- where it cannot desorb from the surface.[40-41]

The scattering of molecules can be studied by molecular beam scattering techniques. An experimental set-up is shown in figure 18. A gas source with a high pressure is connected to the nozzle. The gas expands from high pressure through the nozzle. The gas molecules will colloid many times before they reach a thermal equilibrium. The nozzle is aligned with a skimmer to re-collimate the beam, which then will be directed to the main chamber to impinge the surface. The system is differentially pumped with diffusion pumps and turbo molecular pumps to avoid the gas

loads and to facilitate a free molecular flow. The beam created with nozzle source is called a supersonic beam because the mean free path of the molecules are less than the diameter of the nozzle resulting in a Knudson number less than 1; Knudson number is the ratio between mean free path (λ) and the nozzle diameter (d) (K=λ/d). The molecular beam scattering technique allows to quantify the adsorption probability (S) of a molecule, which provides information on the adsorption dynamics of a system.

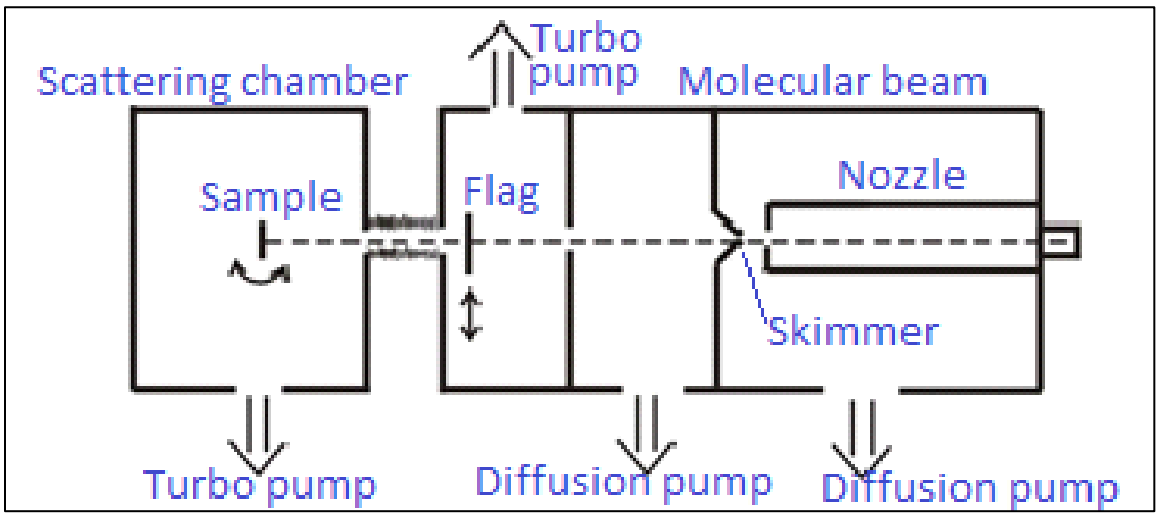

Figure 18. Molecular beam scattering technique set up

The adsorption probability (S) can be defined as the ability of the particle to adsorb on a particular surface. It can be experimentally determined as shown in figure 19. The beam flag is opened to allow the gas molecule to impinge the surface. As soon as the flag is open the pressure in the chamber increases in a step-like manner. The surface acts as a pump by adsorbing the molecules, which results in a slower increase in the pressure until a saturation is reached. Once the surface is saturated the beam flag is closed and the pressure drops. The change in pressure, with time, is simultaneously recorded using a mass spectrometer. The resulting spectrum, also known as King and Wells curve[41-42], allows to calculate the adsorption probability. According to figure 19, the adsorption probability is calculated as: $S(t)= (P_2-P_1/P_2-P_0)$; S approaches S_0 when the

coverage is close to zero. The adsorption dynamics can be classified as activated or non-activated process based on the behavior of adsorption probability with kinetic (impact) energy and surface temperature. In an activated process, the molecules encounter an energy barrier; molecules with low kinetic energy will reflect from the energy barrier whereas molecules with sufficient kinetic energies will overcome the energy barrier. Thus, there will be an increase in the S with an increasing kinetic energy (a step-like increase will be seen initially until a kinetic energy that is sufficient to overcome the energy barrier is observed). However, when the kinetic energy is too high the S will decrease because molecules with higher kinetic energies will have to dissipate more energy before sticking to the surface. In contrast, the non-activated adsorption does not have an energy barrier; S probability decreases with increasing kinetic energy. When the kinetic energy increases the molecules have to lose enough energy to stick to the surface resulting in a decreased S. Overall, the S allows one to differentiate between the activated and the non-activated process.[41-42]

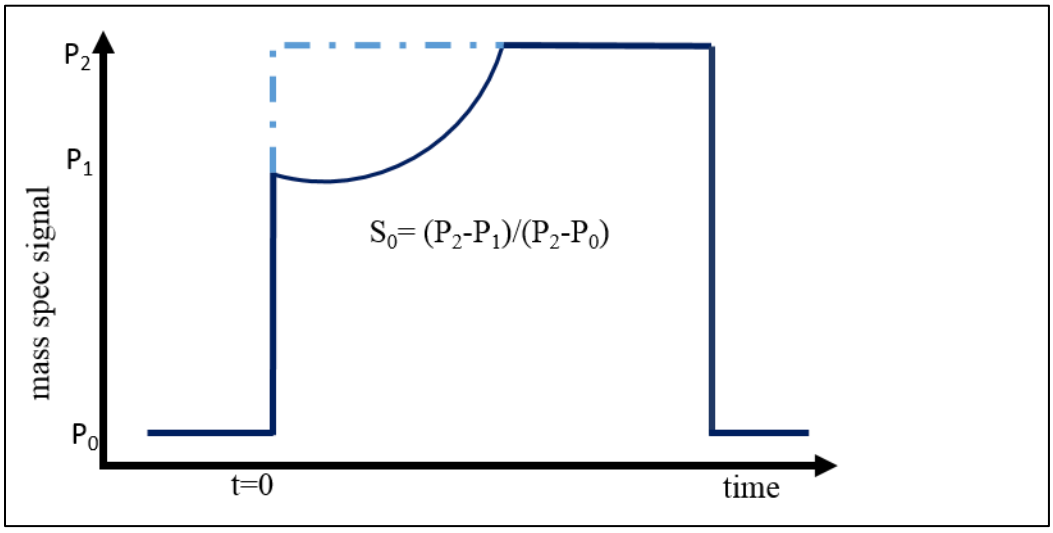

Figure 19. Calculating the adsorption probability

There are three models to map the adsorption dynamics from molecular beam scattering techniques as shown in figure 20. All three models show how the S changes with coverage (θ), which allows to characterize the adsorption dynamics between the molecules and the surface.[41-43]

1. Langmuir model
2. Kisliuk model (precursor-mediated adsorption)
3. Adsorbate-assisted adsorption

Langmuir model:

The Langmuir model assumes that the S=1 at an empty site (for θ=0) and S=0 when all the sites are occupied. The S decreases linearly with θ as shown in figure 20A and ceases when all the adsorption sites are occupied (blocked). However, Langmuir model can be considered as an ideal model because in actual situation attaining S=1 is impossible; not all the empty sites can equally adsorb the incoming molecules.

Kisliuk model (precursor-mediated adsorption):

A precursor state can be defined as a particle trapped in a state before it can adsorb onto the surface. The incoming molecules can encounter a precursor state, which could be either intrinsic or extrinsic; an intrinsic precursor state is a clean surface and the extrinsic precursor state is a pre-occupied precursor state. The incoming molecules will initially be trapped into either intrinsic or extrinsic surface and subsequently diffuse along the surface to hunt for a site to bind. At low temperature the precursor states could have a longer lifetime because the probability to find an empty site is high. Therefore, the change in S with coverage can be considered negligible which eventually will reach zero after saturation as seen in figure 20B.

Adsorbate-assisted adsorption:

Unlike Langmuir and Kisliuk model, the adsorption- assisted adsorption shows a different behavior. The incoming molecule adsorbs on to a pre-occupied adsorbate. The energy transfer between the incoming molecule and the pre-occupied adsorbate is efficient because of the mass-match; mass match (η) can be defined as the ratio between the mass of adsorbate and the mass of substrate ($\eta = m_{(adsorbate)}/m_{(substrate)}$). In an adsorbate-assisted adsorption the η=1, which results in an increased S. The mass-match is attributable to the increase of S with θ which at saturation the S drops to zero figure 20C.

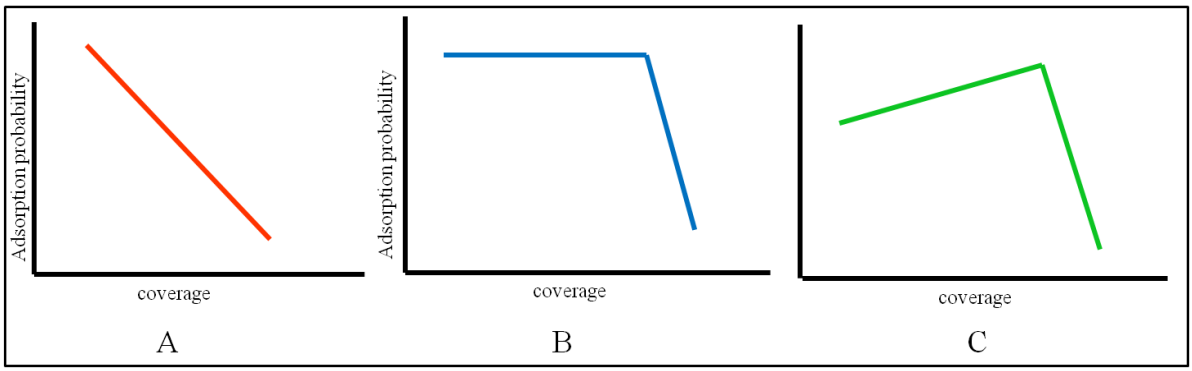

Figure 20. A. Langmuir model. B. Kisluik (precursor-mediated adsorption). C. Adsorbate-assisted adsorption

2.3. Auger Electron Spectroscopy (AES)

The Auger Electron Spectroscopy (AES) was named after the discovery of Auger electrons by Pierre Auger. The Auger process involves three steps (figure 21): ionization, relaxation, and emission. The incident energy removes an electron from the core level creating an ionized atom. The core hole is subsequently neutralized by an electron from the higher energy level. The transition of the electron from higher energy to core level releases energy, which will be used in removing a third electron. The third electron is called the Auger electron; the Auger electron has a following kinetic energy (E_{kin}) to escape into the vacuum,

$$E_{kin} = E_K - E_{L1} - E_{L2,3} \quad (15)$$

E_k is the energy in the core level (K level)

$E_{L1}$is the energy in the higher level from which the transition occurs for neutralizing the core hole

$E_{L2,3}$ is the energy level from which the Auger electron is removed

The Auger electron is assigned by three letters based on the X-ray notation. According to figure 21 the Auger electron can be considered as $KL_1L_{2,3}$. However, most commonly it can be written as KLL because the energy level of relaxation (L_1) and transition process ($L_{2,3}$) are indistinguishable. Besides, the Auger process involves three electrons, which therefore cannot be used in characterizing H and He elements because only one and two electrons are present in H and He, respectively. Furthermore, the Auger process depends on the atomic number (Z); KLL transition occurs for low atomic numbers ($Z \leq 20$), LMM transitions for intermediate ($Z \approx 50$), and MNN transition occurs for higher atomic numbers ($Z > 80$). The difficulty of the incident energy to penetrate to the core levels with higher atomic number leads to the ionization of the first electron in the Auger process to occur from higher energy level instead of K- level. The kinetic energy of Auger electrons are characterized by the binding energy of the electrons, irrespective of the incident energy, thus AES can be used for elemental characterization.[44]

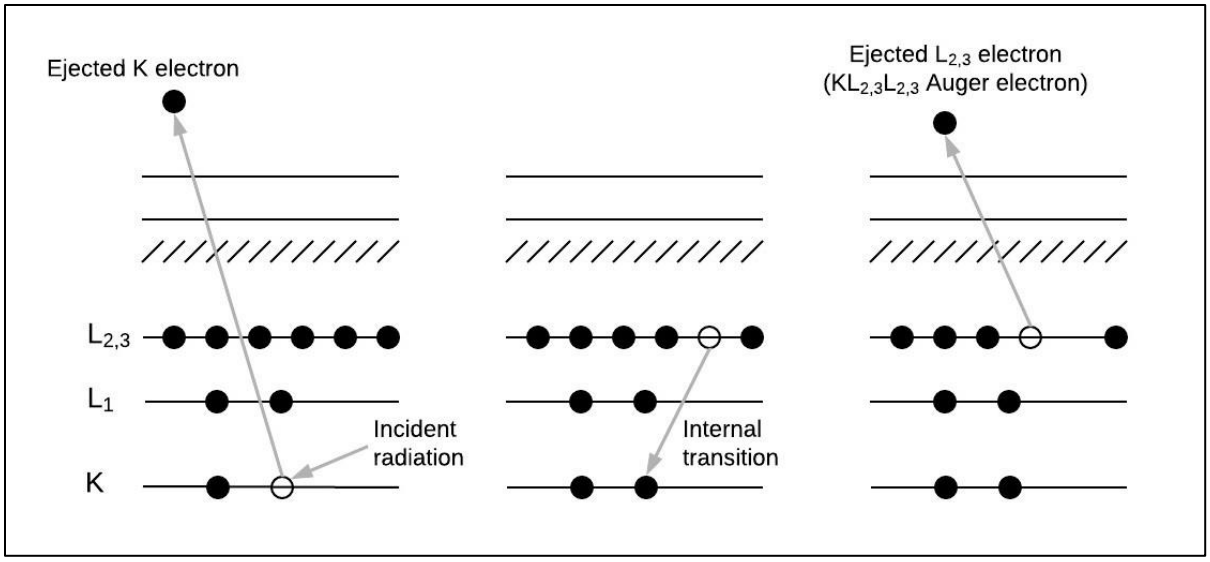

Figure 21. Auger process involving ionization, relaxation, and emission[44]

The AES yield the energy distribution of the emitted electrons with varying kinetic energy (N(E) vs E). However, the Auger peaks are detected along with other secondary electrons; Auger peaks are superimposed in the large background, which arises due to the multitude of large number of scattering process. A differential spectrum will result in a derivative mode of AES signal to identify the AES peaks. A direct spectrum (N(E) vs E) and a derivative spectrum of AES is (dN(E) vs E) is shown in figure 22.

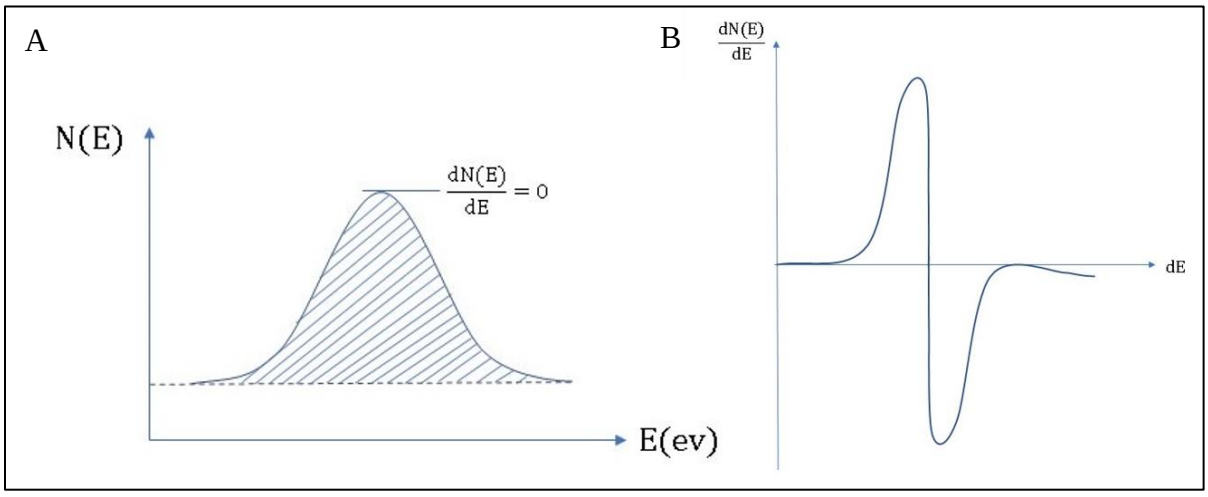

Figure 22. A. direct and B. differentiated spectrum of AES[44]

The instrumentation of AES involves an electron source and an electron analyzer. The electron source emits electrons (usually from a W-filament) with a small range of kinetic energy (mono energetic) to obtain a small spot size on the sample. The analyzer used in AES is a cylindrical mirror analyzer (CMA) or hemispherical sector analyzer (HSA). A schematic of a CMA is shown in Figure 23. The outer cylinder has a negative potential compared to the inner cylinder. Firstly, the Auger electrons emitted from the sample will pass through the defining aperture. Secondly, based on the difference between the outer and the inner potentials the electrons will pass through the detector aperture. Finally, the electrons will be re-focused at the detector- to result in an Auger spectrum. In contrast to CMA, the HSA has a pair of hemispherical electrodes as shown in figure 24. The gap between the electrodes are allowed for the trajectories of the electrons. Only the electrons with energy, $E= ke\Delta V$, where k depends on the radius of the hemisphere, e is the charge of electron, and ΔV is the difference between the hemispherical potential, will pass through the electrodes. A wide range of electrons with $E= ke\Delta V$ can reach the detector. However, a number of detectors are used at the output plane to increase the sensitivity. AES mostly uses CMA instead of HSA because HSA is used mainly for the spectral resolution.[44]

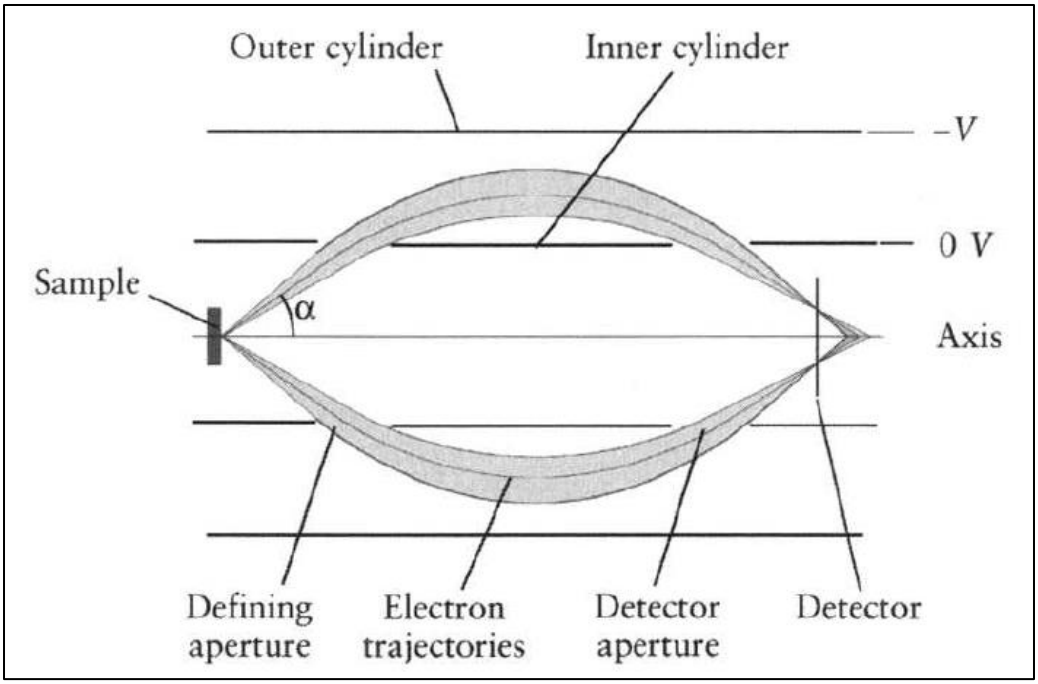

Figure 23. A schematic representation of cylindrical mirror analyzer (CMA)[44]

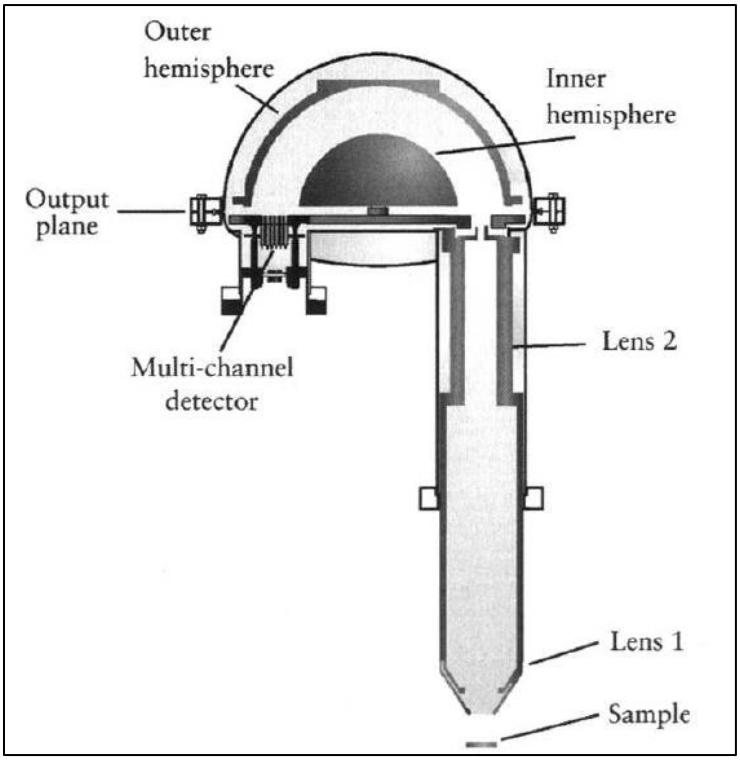

Figure 24. A schematic representation of hemispherical sector analyzer (HSA)[44]

2.4. X-ray photoelectron spectroscopy (XPS)

X-ray photoelectron spectroscopy (XPS) is another surface analytical technique, which was pioneered by Kai Siegbahn at the Uppsala University, Sweden. The principle of XPS is based on the Einstein's photoelectric effect; an X-ray energy removes a core electron of an atom to yield a photo electron. The XPS consists of three steps: absorption and ionization, creation of photo electron, and transport of photoelectron to the surface and escape from the vacuum. A schematic of XPS process is shown in figure 25A. A beam of high energy electrons are created by a filament (12-30 kV) to bombard an anodic material. Bombardment of high energetic electrons can remove an electron from the core level of the anodic material (figure 25B). The energy conservation is maintained by neutralizing the core hole by transiting an electron from the higher energy level. The transition leads to a Kα radiation, which is a characteristic radiation of the anodic material. The commonly used anodic materials are Mg and Al and the strongest X-ray spectral line produced from these anodes is the Kα radiation; Kα radiation has sufficient energy (Mg Kα= 1253.6 eV and Al Kα= 1486.6 eV) to excite the photoelectron from the core levels in all the elements in the periodic table.[44] When a photoelectron is ejected from an atom, the electron reaches the detector with a kinetic energy given as,

$$E_{kin} = h\nu - E_{BE} - \Phi \quad (16)$$

$$E_{BE} = h\nu - E_{kin} - \Phi \quad (17)$$

E_{kin}: kinetic energy of the photoelectron

$h\nu$: photon energy

E_{BE}: binding energy of the core level electron

Φ: work function (energy required to remove the electron from the highest occupied energy to the vacuum level

However, the XPS is recorded as the intensity vs binding energy. Core electrons are not affected by the surrounding and hence the binding energy of the core electrons is characteristic of the parent element and the atomic energy level. In addition, XPS also allows to characterize the chemical state (oxidation state) of an atom; XPS is known as Electron Spectroscopy for Chemical analysis (ESCA). Therefore, XPS is used to study the elemental composition of the surfaces.

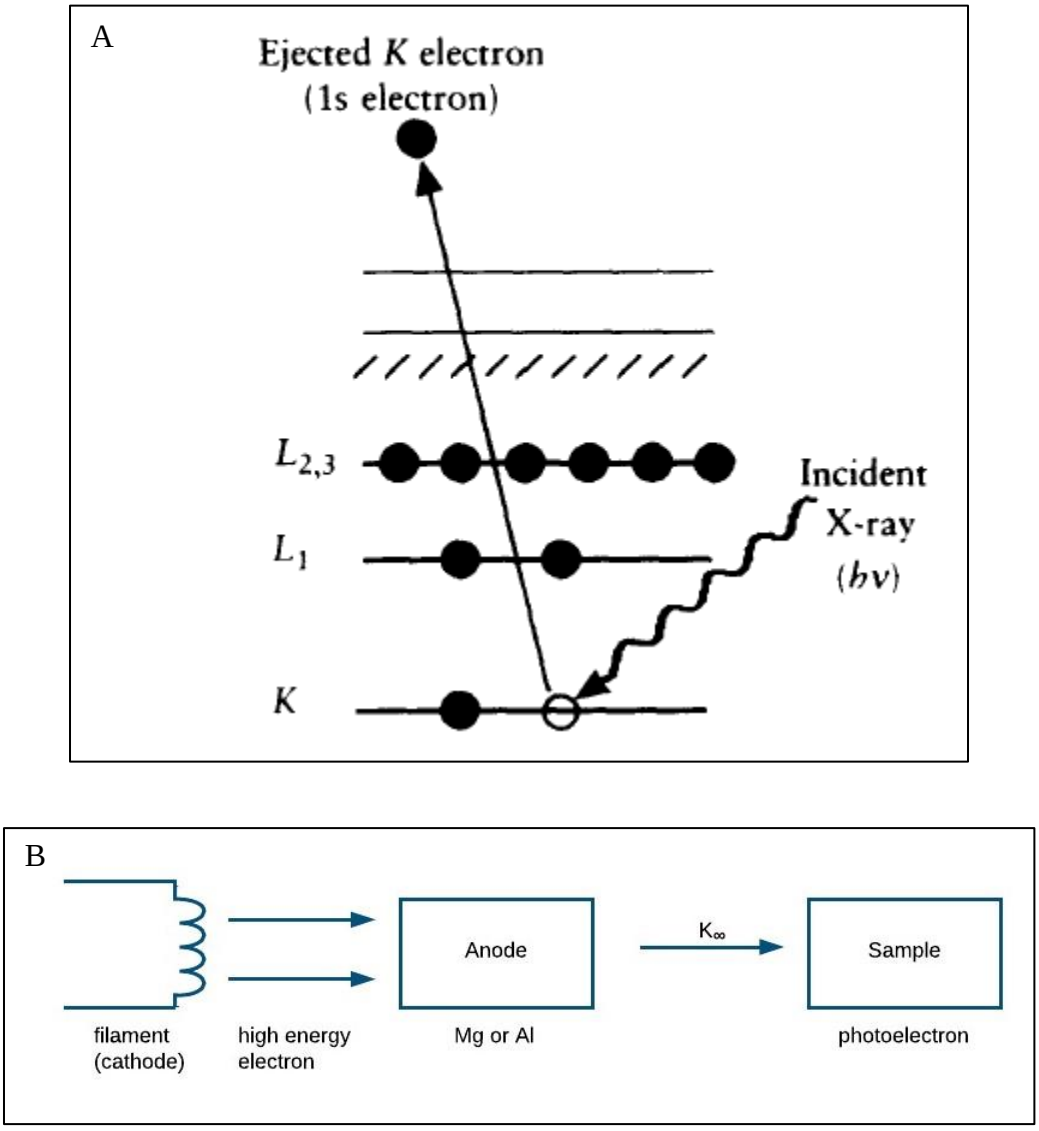

Figure 25. A. Photoelectric effect in XPS. B. Anodic materials producing Kα radiation[44]

An XPS survey scan of a silver (Ag) surface is shown in figure 26. Two effects are clearly seen in the survey scan: stepped background and peak splitting. The stepped background arises due to the inelastic process of electrons close to the valence shell. The background effect is higher for the atomic levels with higher binding energies; core levels are located deeper in the atoms and when electrons are ejected from the core levels the energy losses are high due to the inelastic scattering of the matrix, which leads to a higher background. Besides, XPS allows to study the peak splitting of atoms. Atoms with non-zero angular momentum ($l>0$) interact with an unpaired electron to produce spin-orbit coupling. In the case of Ag, 3d transition is split as a doublet with 2:3 degeneracy. Peak splitting is a characteristic feature of XPS. In addition, shake-up peaks are also observed in XPS. The shake-up peaks occur when the outgoing photoelectron interacts or shakes up the valence electron and rises it to a higher energy level; a part of the kinetic energy of the outgoing photoelectron is lost resulting in a "shake-up" peak at a higher binding energy. Furthermore, the shake-up peaks are also observed when there is a metal-ligand charge transfer. For example, CuO and Cu_2O can be differentiated by observing the shake-up peaks. The CuO (Cu^{2+} oxidation state of Cu) has a vacant d-orbital (d-hole) and a charge transfer can occur from oxygen to the vacant d-orbital resulting in a strong shake-up peak. In contrast, Cu_2O (Cu^{+} oxidation state of Cu) has a filled d-orbital, which does not allow the charge transfer from oxygen- leading to no shake-up peaks in XPS. Overall, the XPS provides a wide range of information about the surface in terms of parent element, atomic levels, stepped background, peak splitting, and shake-up peaks.[44]

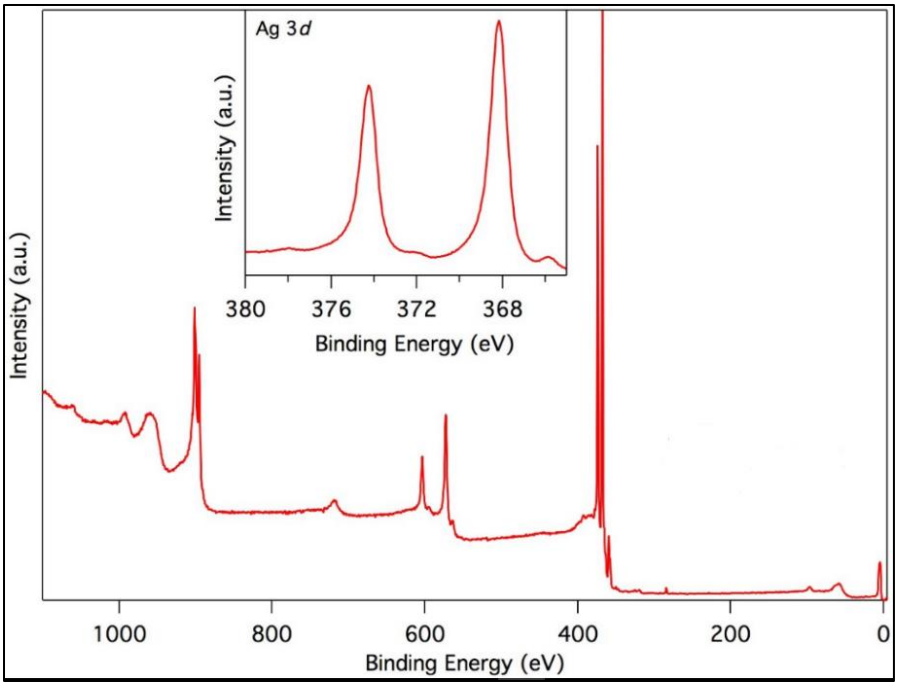

Figure 26. XPS survey scan of Ag. Inset shows the peak splitting of 3d orbital of Ag and the shake-up peak, which is a small "hump" in between the splitting[45]

2.5. Low energy electron diffraction (LEED)

Diffraction techniques allow to study the crystalline properties of the surfaces to understand the fundamentals of the surfaces in terms of unit cell and surface defects. Low energy electron diffraction (LEED) is a surface analytical technique, which utilizes the elastically back scattered electrons to map the crystalline order of the surface. The wave nature of the electrons are involved in producing diffractions. The wave-like behavior of the electron can be given by the DeBrogile equation,

$$\lambda = h/mv \qquad (18)$$

is the wavelength of the incident electron

h is the Plank's constant

m is the mass of electron

v is the velocity of the electron

Combining the kinetic energy of the electron ($E=1/2\ mv^2$) with the DeBrogile equation gives a modified DeBrogiles equation,

$$\lambda= (150.6/E)^{1/2} \quad (19)$$

As the name implies, LEED uses low energy electrons to interact with the matter (surface). LEED operated at 20-1000 eV energies results in DeBrogile wavelengths of 2.74-0.388 Å. To obtain a reasonable diffraction pattern the wavelength should be approximately equal to the interspacing distance (d) of the atoms in a surface.

LEED has two major components: electron gun and a detector. The instrumentation of a LEED is shown in figure 27.[46] Electron gun provides electrons with a wide range of energies. The detector consists of three grids and a fluorescent screen. The grid near the sample (G1) is set to earth potential to ensure a field-free region for the diffracted electrons. The second grid (G2) has a slightly negative potential compared to the incident beam to filter the inelastically scattered electron; G2 serves as a cut-off filter. Similar to G1, the third grid (G3) is connected to earth potential to reduce the effect of high voltage set on the screen. The florescent screen is set to high voltage to accelerate the elastically back scattered electrons. When the elastically back scattered electrons encounter the florescent screen, the diffraction will be seen as bright spots. The constructive interference of the incident beam will result in the reciprocal lattice of the surface structure; the reciprocal lattice can be used to calculate the lattice in the real space. Besides, according to Bragg's scattering equation ($n\lambda= d\sin\theta$; $\sin\theta= n\lambda/d$), for a fixed value of interatomic spacing (d) when the energy of the electrons increase (λ decrease) the diffraction angle will become closer and the diffraction spots will become narrower. Thus changing the energies of the electrons generated from the electron gun can provide a wide range of information when they are elastically backscattered from the surface.[47]

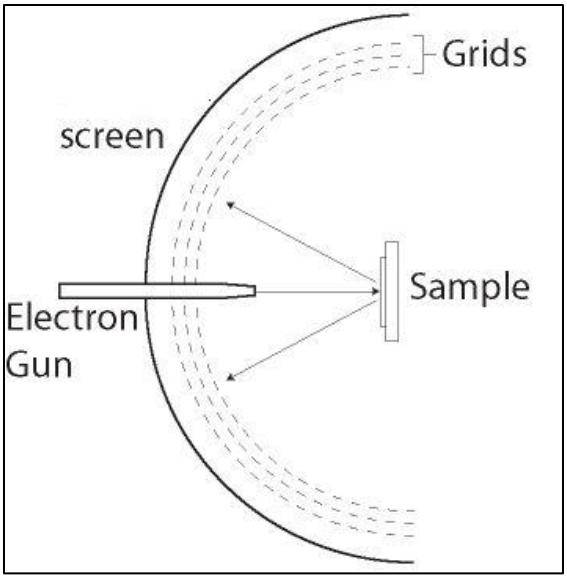

Figure 27. LEED instrumentation[46]

2.6. Raman spectroscopy

Raman spectroscopy operates based on the light scattering process. Light scattering can occur elastically or inelastically. The elastic process is when the frequency of the scattered light is same as the incident light- also known as "Rayleigh scattering". In contrast, the inelastic scattering occurs when the scattering frequency is different than the incident frequency. If the scattered frequency is less than the incident frequency, the process is known as Stokes scattering and if the scattered frequency is higher than the incident frequency it is called Anti-Stokes scattering. The elastic and inelastic scattering process is shown in figure 28. Raman spectroscopy originates from the inelastic scattering process of light and provides details of the excitations of materials, which can be related to the properties of the materials. Although both Stoke and Anti-Stoke can be used in Raman spectroscopy, due to the higher intensity only Stoke scattering is exploited in studying the Raman spectroscopy; ground state energy levels are highly populated and hence Stoke lines have a higher intensity. The sample is irradiated by an intense laser beam and the scattered light is measured perpendicular to the incident light. The samples with change in

polarizability during excitation with laser beam will show Raman active modes. Thus Raman spectroscopy will detail the vibrational excitations of the polarizable samples.[48-50]

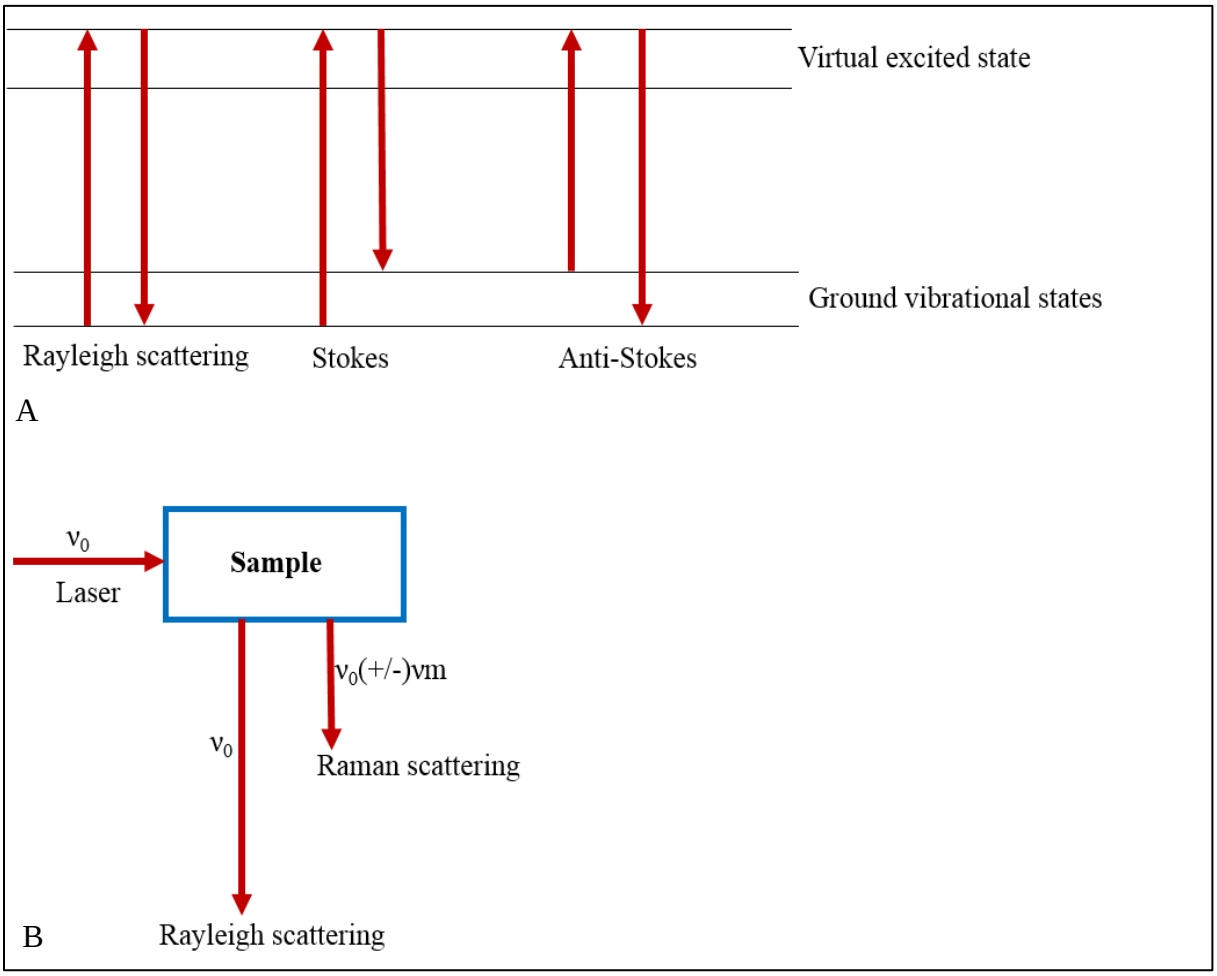

Figure 28. A. Light scattering process. B. Measuring Raman scattering[51]

The Raman spectroscopy instrumentation has 5 major components: excitation source, sample illumination and light collection, sample holder, monochromator, and detector. The excitation source is a laser beam. The laser beam is usually created using Ar or Kr gas (gas lasers). The lasers are used as excitation source because of the small diameter of the laser beam and high monochromatic beams. Since the laser excitation energy is insufficient to transfer electrons to a real excited state the electrons are transferred to a "virtual state" after absorbing the incident laser

beam; the scattering process in Raman occurs from the "virtual energy" state. The laser beam is focused onto the sample using optical lenses to illuminate the sample and to collect the scattered light from the sample. The sample holder is usually a stage similar to an optical microscope sample stage above which the optical lenses are placed to focus the laser beam. The monochromator used in Raman spectroscopy acts as a filter for Rayleigh scattering. In addition, the detection can be carried out by various detectors such as phonon counting, photodiode array detection, and charged-couples device detection (CCD). The experimental set-up of Raman spectroscopy is not complicated with added advantages of less sample preparation time and non-destructive analysis of the sample.[51]

2.6.1. Raman spectroscopy for sp^2 nanocarbons

Graphene is a "mother-structure" of sp^2 nanocarbons because rolling, cutting, and stacking of graphene can result in carbon nanotubes (CNTs), graphene nanoribbons, and graphite respectively. All these nanocarbons have Π- electron cloud due to their sp^2 hybridization; the sp^2 nanocarbons are Raman active because the Π- electron cloud can undergo change in polarizability. Raman spectroscopy allows structural analysis of the sp^2 nanocarbons. A comparison of Raman peaks for graphene, graphite, and CNTs is discussed in the proceeding section.

G-band: The G-band appears due to the first order Raman scattering (figure 29A) and present in all sp^2 nanocarbons at around $1585cm^{-1}$. The stretching of C-C bonds during laser excitation results in a G- band; G-band is sensitive to stretching. Unlike graphene and graphite, the G-band is split into G^+ and G^- in CNT, specifically in single-walled carbon nanotube (SWCNT), which is attributable to the bending of graphene sheet. G^+ corresponds to the bending along the folding axis and G^- is due to the bending along the circumference. In contrast to SWCNTs, the multi-walled carbon nanotubes (MWCNTs) do not show a pronounced splitting of

G-band. The diameter distribution of MWCNTs lead to a small split of G-band with a small intensity and smearing of the bands around 1585 cm^{-1}. [52-55]

G'-band: This is a Raman signature peak, which arises due to the sp^2 carbon. However, unlike G-band the G'-band is a result of second order Raman scattering (figure 29B). G'-band is dispersive in nature because of the double resonance in the second order Raman scattering. The G'-band appears at around 2700 cm^{-1} and can be used in distinguishing between single-layer graphene and multi-layer graphene (and graphite). The degree of graphitization can be evidenced by the shape and the intensity of the G'- band. A one layer graphene (single-layer graphene) has one double resonance process- resulting in a single G'-band. In contrast a bi-layer graphene has four possible double resonance, which gives 4 peaks. Furthermore, as the number of graphene layers increase the number of double resonance will also increase resulting in broader peak with low intensity. The change in G'-band with a change in number of graphene layers is shown in figure 26.[52-55]

D-band: A disorder induced peak is observed around 1350 cm^{-1}, designated as D-band. A second order Raman scattering results in a defect induced peak. However, in contrast to the second order Raman scattering in G'- band, the D-band involves one elastic scattering and one inelastic scattering process (figure 29C). The defect allows breathing mode of carbon hexagons, which contribute towards the D-band. The intensity of the D-band can be used in quantifying the degree of disorder; the degree of disorder can be given as,

$$I_D/I_G = A/L_a \quad (20)$$

I_D is the intensity of the D-band

I_G is the intensity of G-band

A is the excitation frequency of the laser beam

L_a is the size of the crystallite

For a fixed value of laser excitation frequency, the degree of disorder will increase with decreasing size of the crystallite. The decreasing size of crystallite implies that the sp^2 carbon hexagonal structure is disappearing and resulting in amophorization of the material. Therefore, the pristine and the disordered or damaged materials can be distinguished.

Radial breathing mode (RBM): The radial breathing mode (RBM) is a signature band for CNTs. This arises due to the "tube-like breathing" of the CNTs; only CNTs have this feature hence can be differentiated from graphene and graphite. Furthermore, the MWCNTs can be distinguished from SWCNTs because MWCNTs do not have a RBM. The absence of RBM in MWCNTs is attributable to the diameter of the tubes in MWCNT because the larger outer diameter results in a weak RBM signal and the diameter distribution of nanotubes in MWCNTs make RBM broader.[52-55]

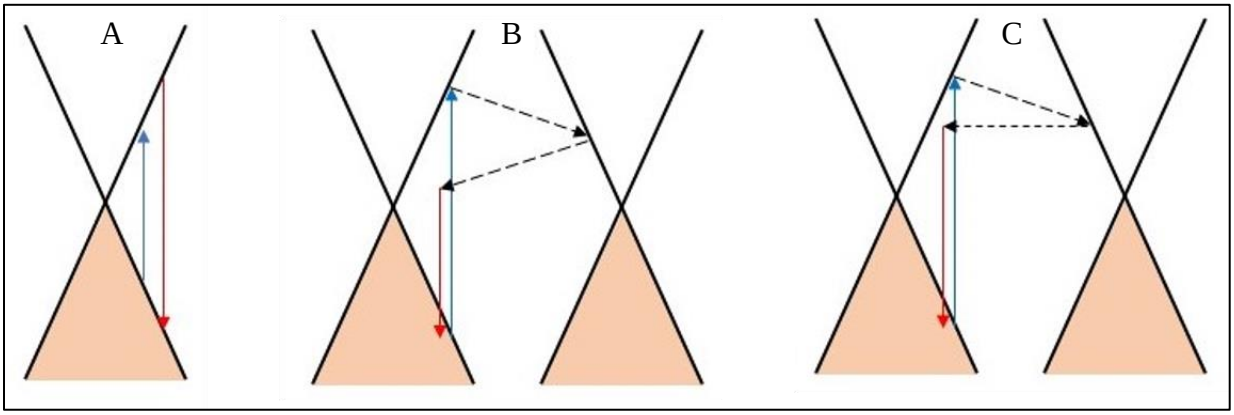

Figure 29. A. G-band due to first order Raman scattering. B. G'- band due to second order Raman scattering. C. D-band due to second order Raman scattering[36]

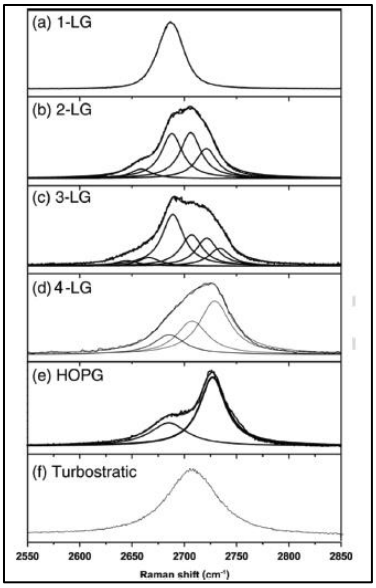

Figure 30. Change in G' band with changing number of graphene layers[52]

CHAPTER 3. EXPERIMENTAL

This chapter provides the details of the experimental procedures and the techniques used for the studies from chapter 4 through chapter 7. The samples utilized in chapters 4-7 involves both CVD (graphene/Cu and graphene/SiO_2) and PVD graphene samples (graphene/Ru(0001)) and their substrates (Cu, SiO_2, and Ru(0001)). The first section describes the sample cleaning and characterization of Cu and graphene/Cu. The second section describes the sample cleaning and characterization of SiO_2 and graphene/SiO_2. The third section illustrates the synthesis of PVD graphene (graphene/Ru(0001), which includes substrate cleaning (Ru(0001)), characterization, and graphene synthesis and characterization. Furthermore, this section will also demonstrate the synthesis and characterization of graphene oxide on Ru(0001). The fourth section describes the TDS procedure used in carrying out the adsorption kinetics experiments. The final section describes the molecular beam scattering technique used for the adsorption dynamics experiments.

All the experiments were carried out in one or both of the UHV chambers, which were pumped with various roughing pumps and turbo-molecular pumps to reach a base pressure of $5x10^{-10}$ mbar. One chamber was housed with LEED, AES, and TDS. The other chamber was attached to a supersonic molecular beam scattering system, which was differentially- pumped with two diffusion pumps. Furthermore this system was housed with AES, XPS, and TDS. Both, AES and XPS used a cylindrical mirror analyzer (CMA). In addition, both the chambers had sputter gun and home-made oxygen dozer for various experiments. A schematic of the chambers are show in chapter 2 (figures 10 and 11).

3.1. Sample cleaning and characterization of Cu and graphene/Cu

3.1.1. Sample cleaning of Cu and graphene/Cu

The as-received Cu substrate was subjected to multiple cycles of Argon ion sputtering and annealing. The inert and energetic Argon ions (2 kV) were generated using a sputter gun, which removed multiple layers of amorphous carbon per cycle. The sputtering leaves pitted surface, which was healed by subsequent annealing to high temperature (≈900-1000 K). The annealing facilitated the surface diffusion and removed the defected sites to form a flat and a clean surface. Several sputtering-annealing cycles were repeated until an atomically cleaned surface was obtained. The atomically cleaned surface was characterized by both AES and XPS.

The graphene/Cu sample was synthesized using chemical vapor deposition (Graphene supermarket Inc.). The graphene growth was carried out under a high temperature tube furnace; graphene is grown on both sides of the Cu foil over the steps and the grain boundaries to produce crystalline graphene. The as-received graphene/Cu was annealed to around 675 K. Although higher temperatures are preferable to obtain a clean surface, at temperatures above 750 K, the graphene/Cu samples started to deteriorate. Thus 675 K, was used to obtain an atomically clean surface.

3.1.2. Sample characterization of Cu and graphene/Cu

The atomically clean Cu and graphene/Cu samples were characterized by both AES and XPS. A clean Cu surface obtained by multiple sputtering- annealing cycles is shown in figure 31. The atomically clean surface had trace amount of oxygen at 503 eV, which was not removed by sputtering-annealing cycles. In addition, the XPS (Mg kα line at 1253.6 eV) showed a similar trend for the atomically clean surface (figure 32). However, in XPS the peak splitting of the Cu_{2p} was seen as 1:2 ratio for $Cu_{2p1/2}$ and $Cu_{2p3/2}$ respectively. In addition, shake-up peaks were observed,

which could be attributed to the presence of oxide; metal-ligand electron transfer between oxygen and Cu can result in shake-up peaks. The carbon on XPS is seen at 284 eV, which is very low in concentration (trace amounts). X-ray induced AES peaks were also observed at around 484 eV corresponding to the LMM transition of Cu.

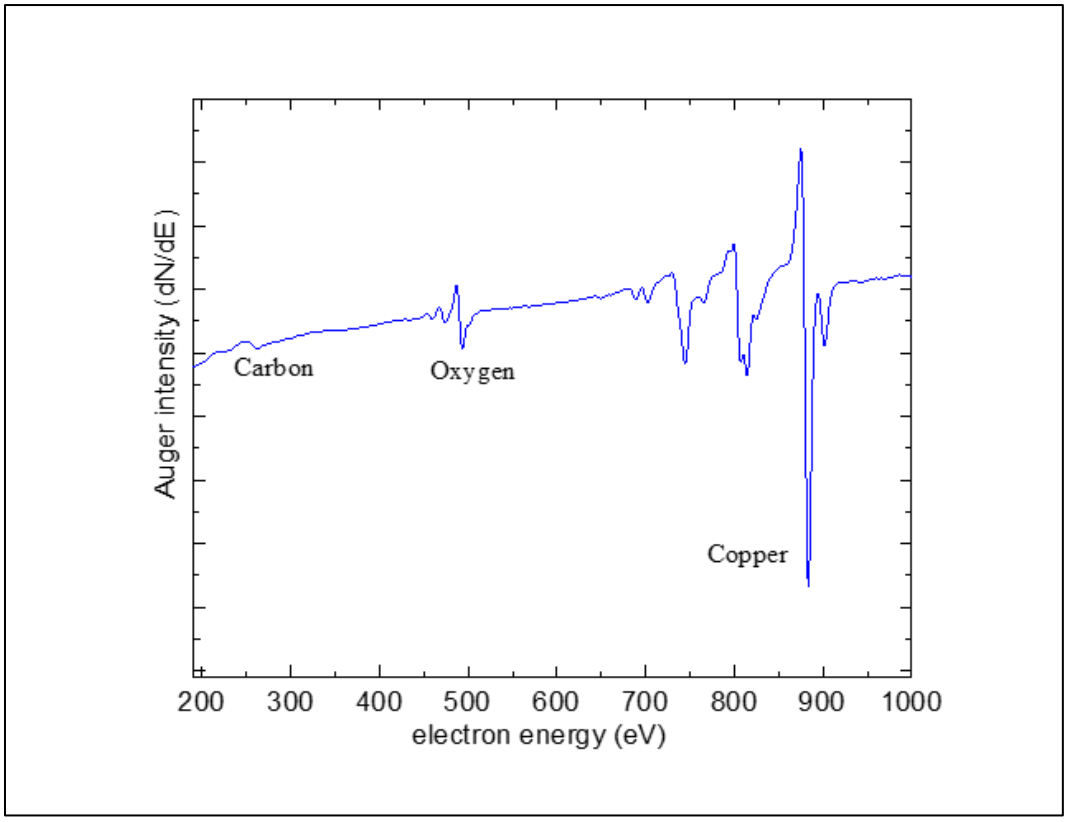

Figure 31. AES for clean Cu substrate

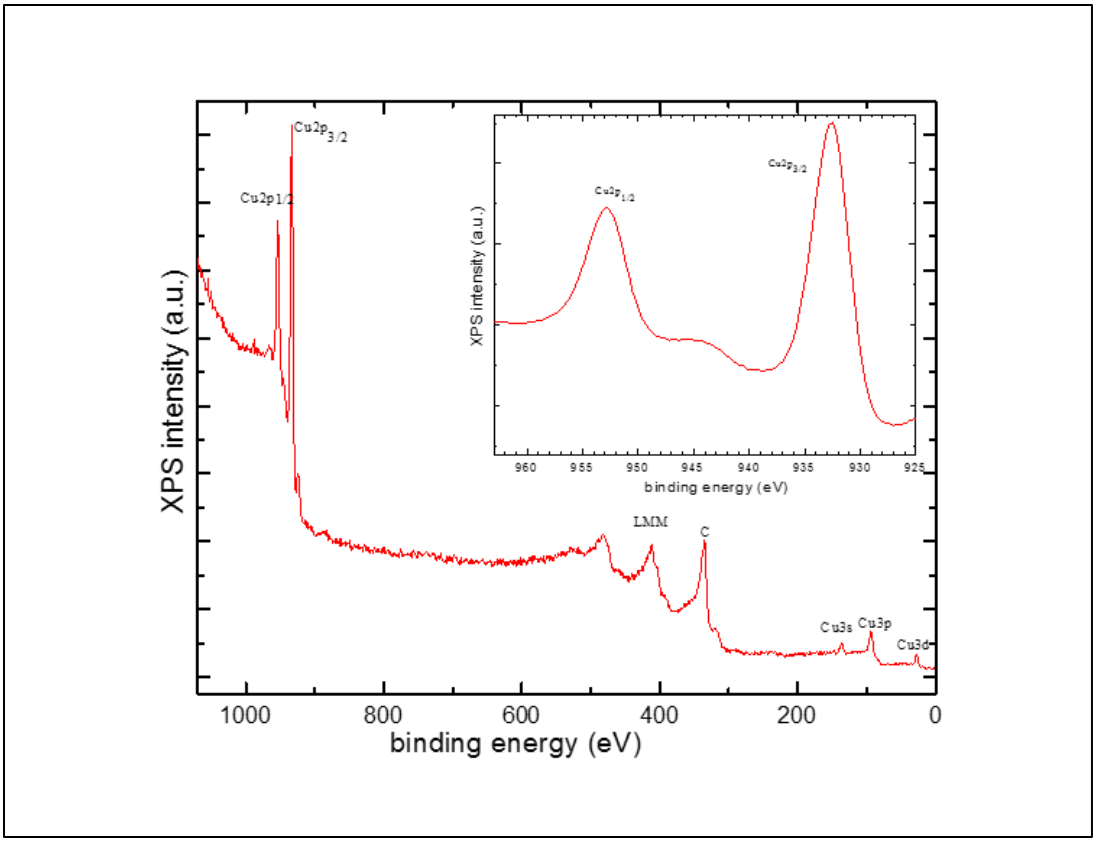

Figure 32. XPS for clean Cu and the inset shows the Cu region

The annealed graphene/Cu were characterized by AES and XPS. The clean graphene/Cu showed C:Cu= 0.85 AES ratio (figure 33), which is in agreement with the literature. In addition, the XPS the Cu_{2p} shows the splitting similar to the Cu substrate. A carbon peak is seen in graphene/Cu sample at 284 eV due to the presence of graphene on a Cu foil (figure 34).

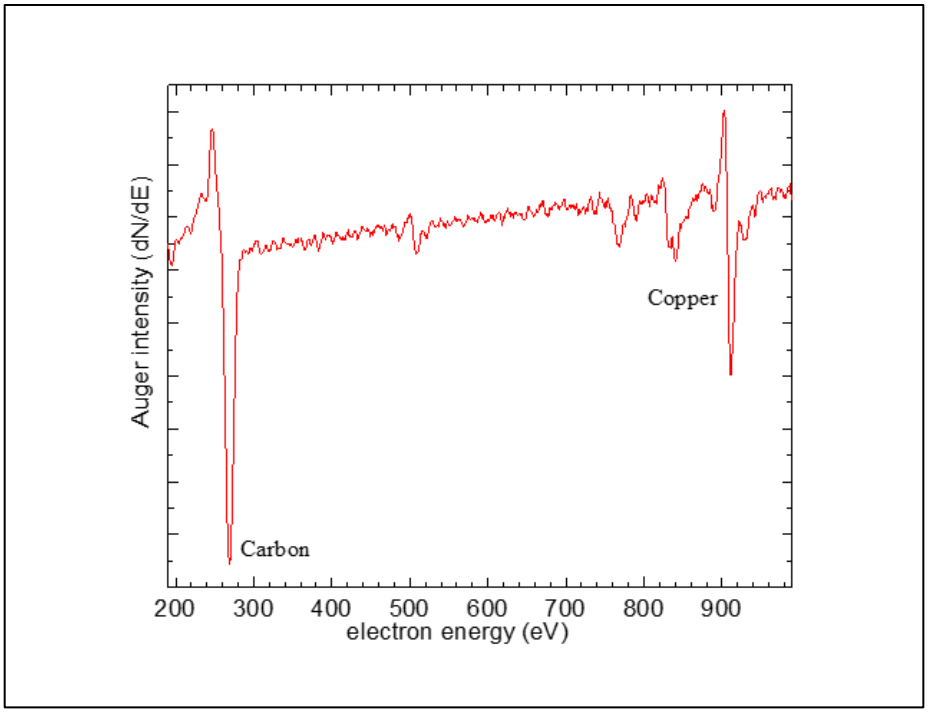

Figure 33. AES for graphene/Cu shows C:Cu= 0.85

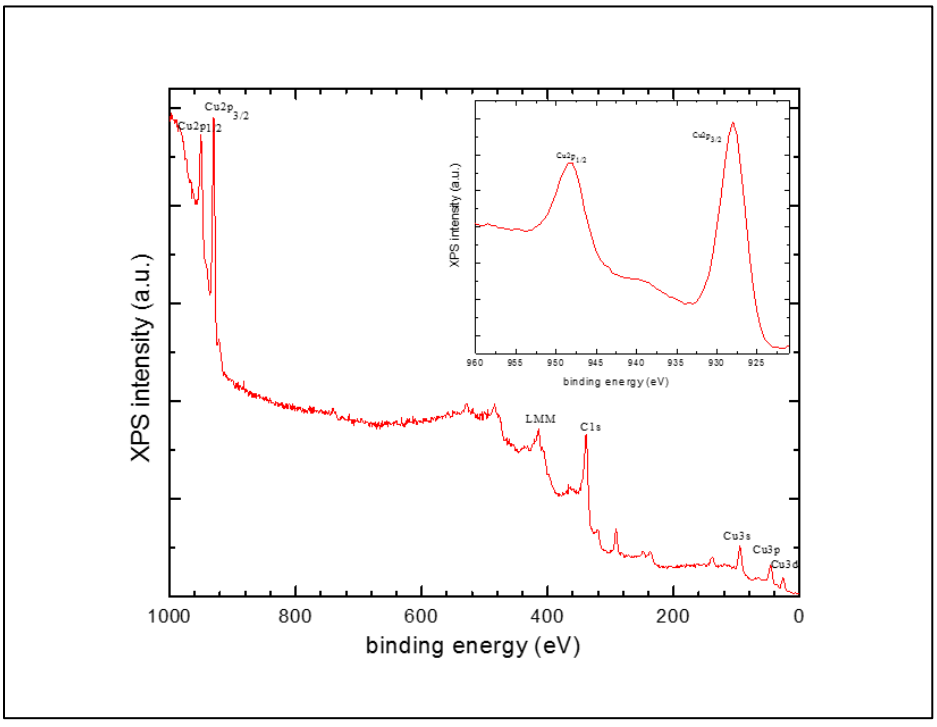

Figure 34. XPS for graphene/ Cu and the inset show the Cu region

3.2. Sample cleaning of SiO_2 and graphene/SiO_2

Similar to Cu substrate, the as-received SiO_2 substrate was also subjected to multiple Argon ion sputtering- annealing cycles. The repeated cycles removed the amorphous carbon on the SiO_2 substrate resulting in an atomically clean surface. In terms of graphene/SiO_2 (Graphene supermarket Inc.), the synthesis was carried out by Graphene supermarket Inc as follow: the graphene was grown on a Cu foil under a high temperature tube furnace. Once the graphene was grown, it was spin coated with polymethylmethcrylate (PMMA) to provide a protective coating during the transfer process. Subsequently, the underneath Cu foil was etched with acids (HCl or HNO_3) and the free-standing graphene with a protective coating was transferred to the substrate of interest. Once the graphene with the protective coating was transferred on to SiO_2, the protective layer was dissolved with acetone. The defect densities reported by the vendor (graphene supermarket Inc.)[1,56] was less than 5%. The as-received graphene/SiO_2 was then annealed to 675 K to produce atomically clean surface.

3.2.1. Sample characterization of SiO_2 and graphene/SiO_2

The atomically cleaned SiO_2 substrate and graphene/SiO_2 were characterized by AES and XPS. According to AES, the atomically clean SiO_2 had only Si and O peaks and did not show any carbon impurities (Figure 35). In addition, XPS also showed a similar trend as AES and X-ray induced AES peaks were evident at around 790 eV for KLL transition (Figure 36).

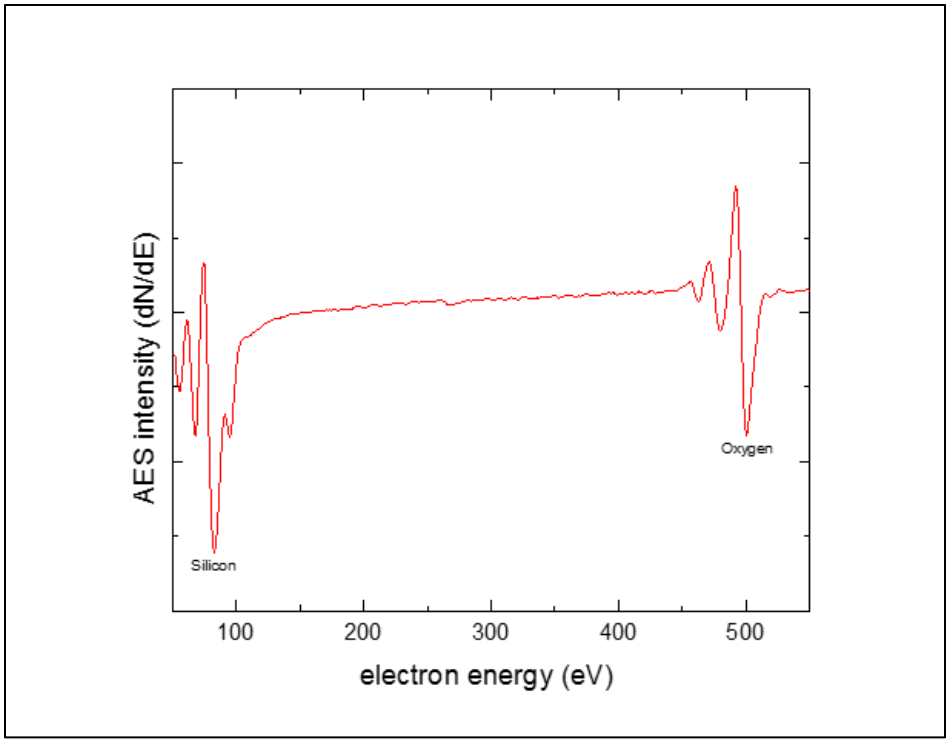

Figure 35. AES for clean SiO_2 substrate

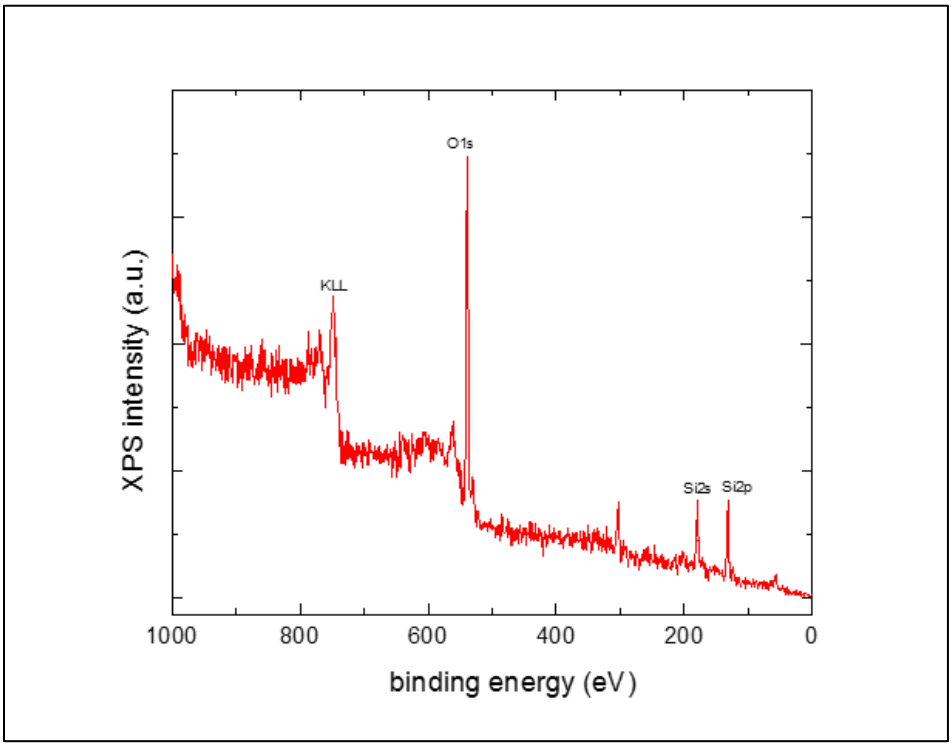

Figure 36. XPS for clean SiO_2 substrate

The graphene/SiO_2 was characterized by AES, XPS, and Raman spectroscopy. The AES of C:Si ratio showed 0.45 and C:O ratio 0.72, which confirms the surface cleanliness of the graphene/SiO_2 (figure 37). The cleanliness was further confirmed by XPS as shown in figure 38. In addition, the defect density was quantified by Raman spectroscopy. The G-peak arises due to the first-order Raman scattering, where the laser induces the stretching of the C-C bond in the sp^2 hybridized carbon. The G' peak is a result of second-order Raman scattering and it is intense than the G-peak due to the double resonance in the second-order Raman scattering. The I_G and the $I_{G'}$ are the characteristic Raman peaks for the graphene surface (figure 39). D-peak is attributable to the defects present in the surface; I_D is proportional to the amount of the defect on the surface. The quantification of the defects is calculated by the ratio of I_D:I_G. The graphene/SiO_2 studied had a defect density close to 0.08%- confirming that the sample is atomically clean with negligible amount of defects.

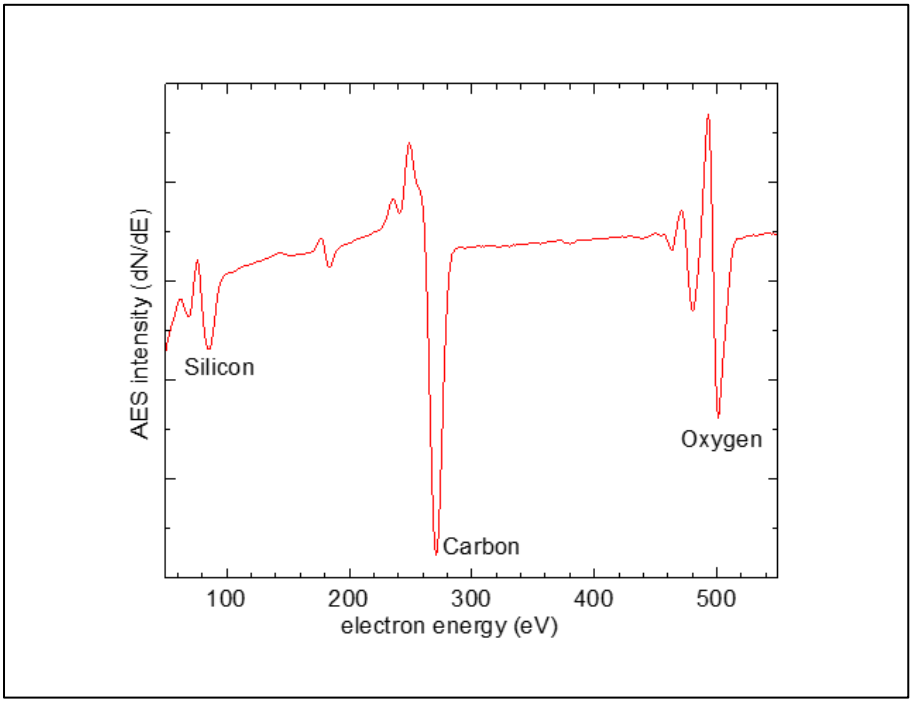

Figure 37. AES for graphene/SiO_2

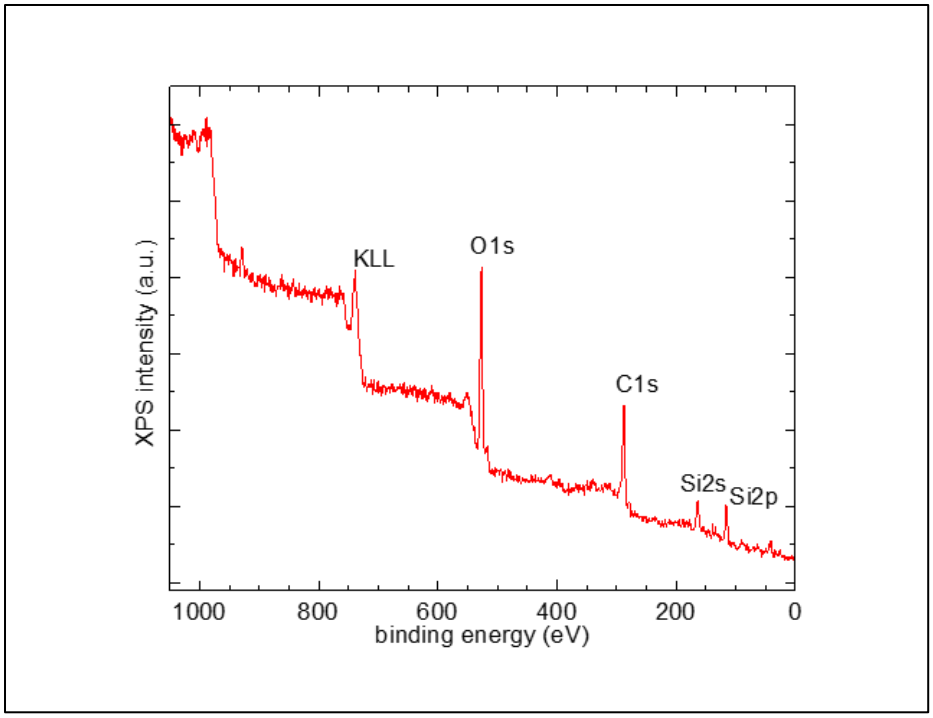

Figure 38. XPS for graphene/SiO_2

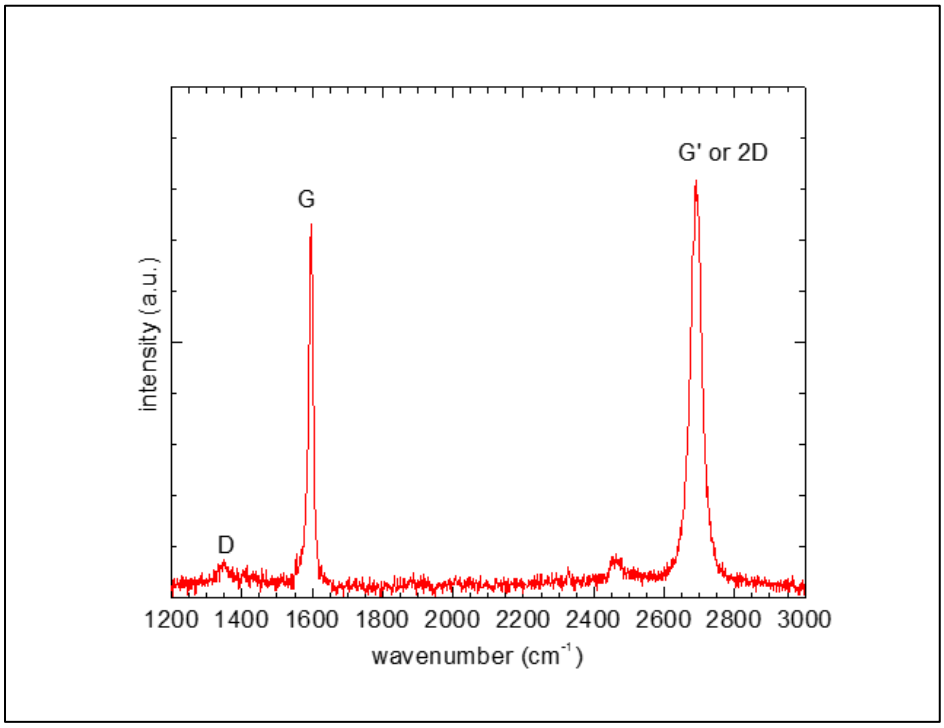

Figure 39. Raman for graphene/SiO_2

3.3. PVD graphene synthesis and characterization

3.3.1. Substrate (Ru(0001)) cleaning

Prior to graphene synthesis, the substrate, Ru(0001), was atomically cleaned. The Ru(0001) surface was sputtered with 2 kV energy of Argon ions for 30 minutes (5-7 cycles). Following the sputtering process, the surface was annealed in the presence of oxygen (P= $1x10^{-7}$ mbar, at 1000 K, for 10 minutes, nearly 5 cycles) to obtain a perfect LEED pattern. Subsequently, the surface was annealed with hydrogen (P= $1x10^{-6}$ mbar, 20 minutes at 300K) to remove the oxygen on the surface. Molecular hydrogen dissociated on Ru(0001). During H_2-annealing the dissociated hydrogen atoms bind to the oxygen on the surface to form –OH groups. At subsequent annealing at 675 K, the –OH groups will be desorbed as water molecules.[57] An atomically clean Ru, with no traces of oxygen, was confirmed by AES and XPS.

3.3.2. Graphene synthesis and characterization on Ru(0001)

A mono layer graphene was synthesized on an atomically clean Ru(0001) surface. The deuterated benzene (C_6D_6) was adsorbed on the clean Ru(0001) substrate at 150 K to avoid condensation, followed by a subsequent ramping of temperature to 770 K. The step surface of Ru(0001) acts as an active site to decompose the C_6D_6 into carbon atoms and deuterium molecule (D_2). Since the adsorption probability of D_2 is approximately zero, on Ru(0001) surface, the desorbed D_2 was captured using TDS at a parent mass of m/e= 4. The carbon, which was formed during the decomposition was annealed to 1100 K- to rearrange into graphene layer. Multiple adsorption-desorption cycles of C_6D_6 were carried out until a mono layer graphene was formed through a "self-terminating" process. At each adsorption cycle 10 L of C_6D_6 was dosed and the D_2 desorption signal was monitored by TDS. Simultaneously, AES was used to characterize the

surface and quantify the carbon coverage on Ru(0001) surface. In addition, LEED was used to characterize the crystallinity of the synthesized surface.

Benzene (C_6H_6) interacts strongly with Ru through the donation of Π electrons to the empty d-orbital of Ru and the back donation from Ru to the Π* orbitals of the C_6H_6 molecule. The strong interaction leads to the dissociation of benzene, in the active sites of Ru, to yield C atoms and hydrogen molecules. In this study, a deuterated benzene (C_6D_6) was used in order to differentiate between the D_2 signal- desorbing from the Ru(0001) surface and the residual background H_2. The amount of desorbed D_2 decreased with the increasing exposure of C_6D_6, which is due to the increased coverage of active sites on Ru(0001) surface; more active sites get covered with graphene with an increased C_6D_6 exposure resulting in lesser decomposition of C_6D_6 and thus decreased desorption of D_2.[58-59] Once all the active sites are covered, there will be negligible or no desorption of D_2 as shown in figure 40. A diverse peak is observed at T>500 K in addition to the narrow peak at 450 K. The peaks do not shift but decrease in intensity with increase coverage of C_6D_6, which could be accounted for the formation of same species (D_2) at decreasing amounts. The step-wise dissociation of C_6D_6 allows to quantify the defects on the surface ((area under the TDS curve at 10 L/area under the TDS curve at 60 L)x100 %)- where the only 2 % defect was evidenced. According to literature, a graphene with 7% or lesser defects can be considered as a pristine graphene.[60] Therefore, the graphene synthesized in this study was also a pristine graphene with lower defect density.

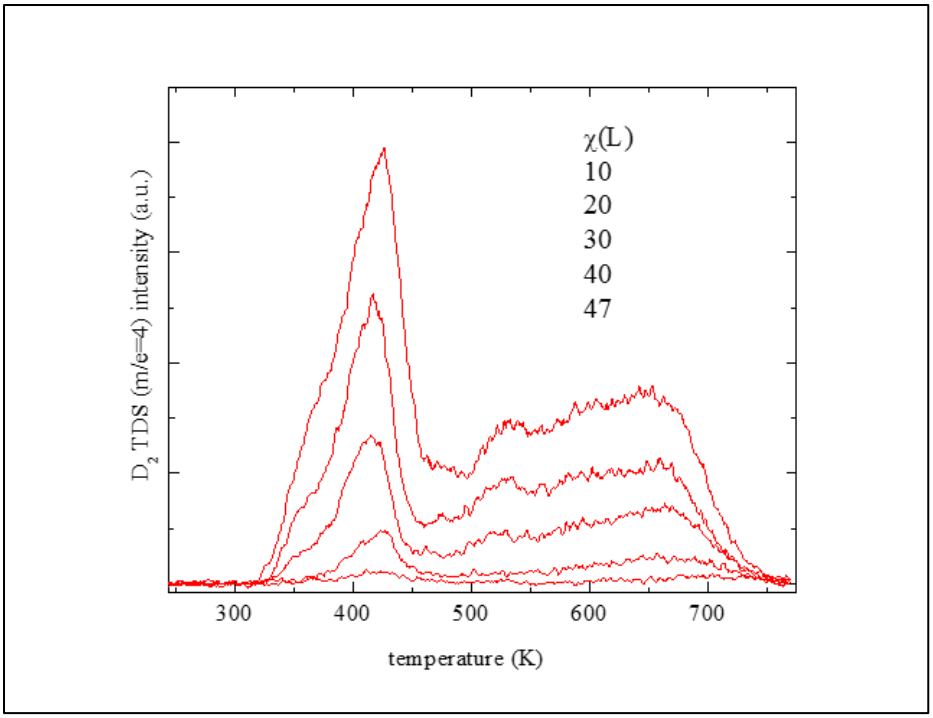

Figure 40. TDS for graphene synthesis. The desorption of D_2 was detected at a parent mass (m/e) of 4

AES was also used to characterize the graphene synthesis on Ru(0001). Unfortunately, the AES carbon and Ru peaks overlap at 272 eV. Thus, the graphene coverage on Ru(0001) was determined using the positive to negative ratio of the AES peak at 272 eV. The Ru has a symmetrical AES peak at 272 eV, while the carbon is dominated by a negative-going peak.[61] An atomically clean Ru(0001), therefore, should have a high positive to negative AES ratio. The step-wise growth of the graphene layer decreases the AES peak intensity since the carbon coverage increases. As depicted in figure 41a, AES for a clean Ru(0001) and a graphene/Ru(0001) is seen. The atomically clean Ru(0001) had an AES ratio of 0.74, which decreased with increasing carbon coverage (figure 41b). Once the mono layer graphene was formed the AES ratio remained constant at 0.42. In addition to AES, XPS was also used to characterize the graphene synthesis. Similar to AES the carbon and Ru peaks overlap in XPS. The peak splitting of Ru leads to $Ru_{3/2}$ and $Ru_{5/2}$ at 284 eV and 279 eV, respectively. The carbon peak overlaps at $Ru_{3/2}$ and hence a difference in the

peak at 284 eV is clearly seen for a clean Ru(0001) and a graphene/Ru(0001), which is shown in figure 42. The peak splitting of clean Ru shows $Ru_{3/2}$ and $Ru_{5/2}$ at a 2:3 ratio. However, once the graphene is covered the 284 eV peak increases compared to the peak at 279 eV. Thus, both, AES and XPS was used to characterize the surface of Ru(0001) and graphene/Ru(0001) during the graphene synthesis.

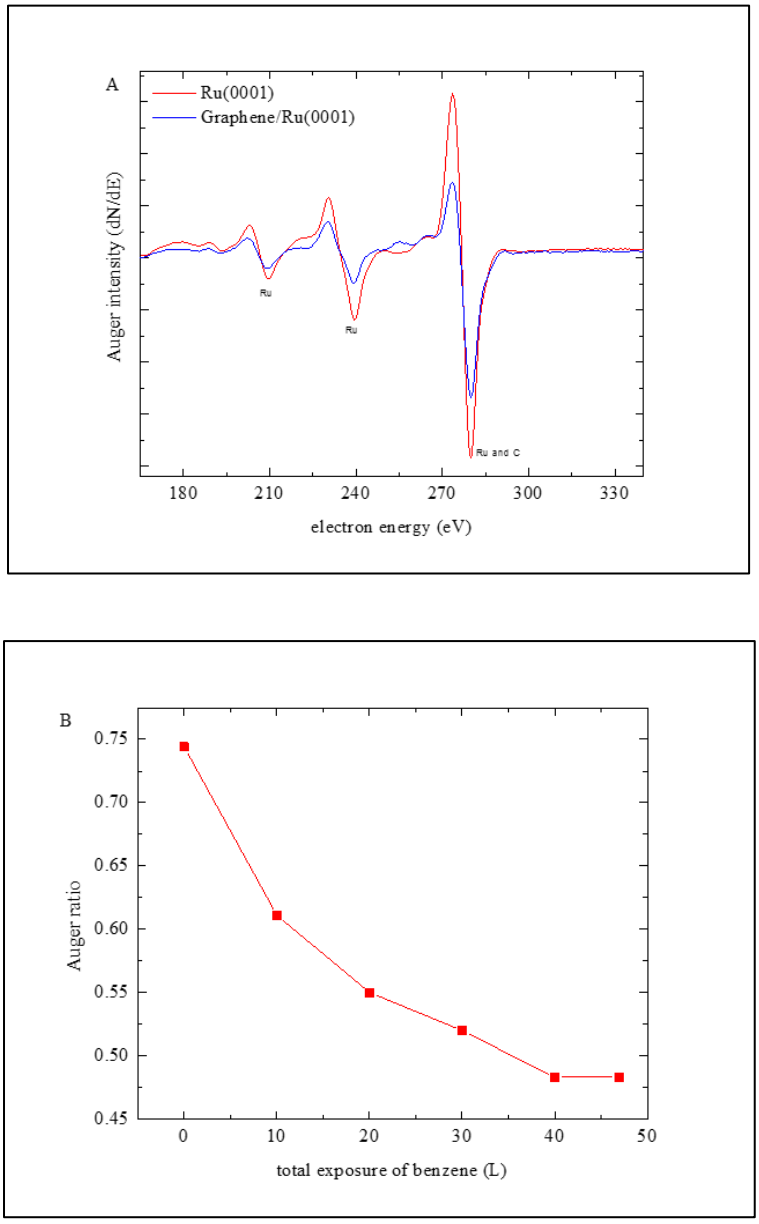

Figure 41. A. AES of Ru and graphene/Ru. B. Change in AES ratio as the graphene is synthesized

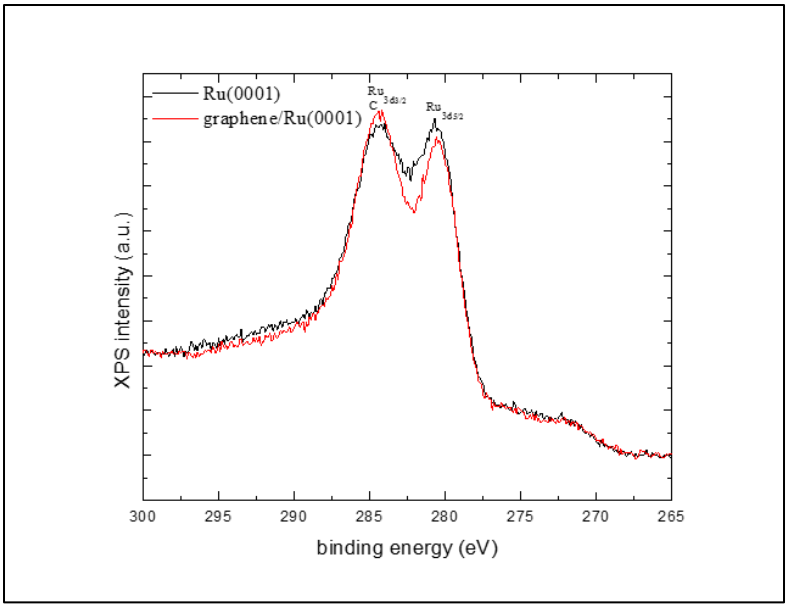

Figure 42. Overlap of C and Ru peaks in XPS

The surface crystallinity of graphene was characterized by LEED. The interaction of C_6D_6 and Ru(0001) occurs through Π donation- back donation, which leads to the maximum overlap when C-C is positioned above Ru(0001). Both, graphene and Ru(0001) have hexagonal unit cells. However, due to the lattice mismatch of the unit cells- graphene forms an incommensurate layer on Ru(0001), which results in a Moiré pattern.[59] The Moiré pattern is seen as "satellite peaks" in LEED. A LEED pattern for an atomically clean Ru(0001) and a crystalline graphene/Ru(0001) is shown in figure 43.

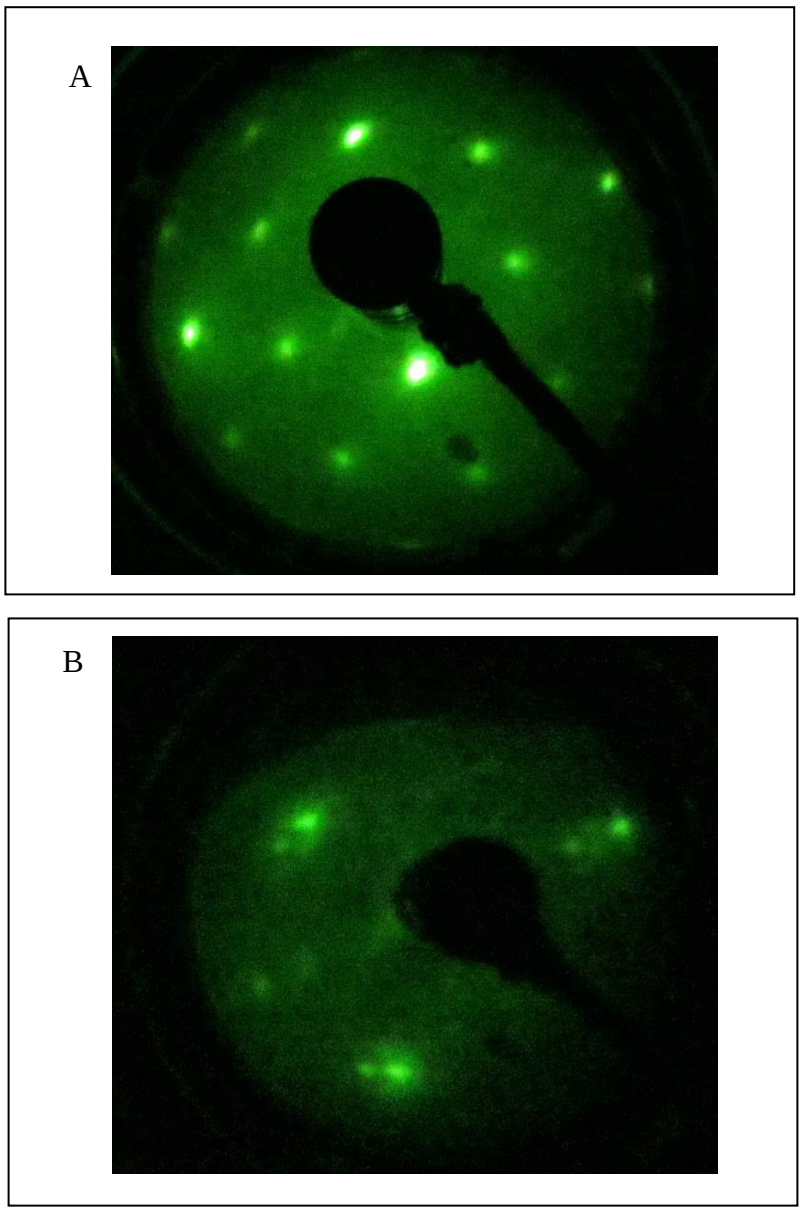

Figure 43. A. Hexagonal LEED pattern for Ru(0001). B. Lattice mismatch causes Moiré pattern when graphene is synthesized on Ru(0001)

3.3. Graphene oxide synthesis and characterization

Graphene oxide was synthesized on a graphene/Ru(0001) surface using atomic oxygen. A W-filament was used to dissociate molecular oxygen to atomic oxygen; atomic oxygen is more reactive than molecular oxygen. The W-filament was operated at room temperature (300 K) and

the oxygen was dosed at increasing coverage (20 L oxygen/ cycle). An oxygen-AES signal was monitored with an increasing coverage of oxygen. The oxygen-AES peak increased and reached saturation at 150- 200 L, which is shown in Figure 44. The saturated oxygen coverage on graphene was considered as a mono layer oxygen coverage, which showed C:O ratio≈ 4-5. Literature reports C:O ratio 2:1 for graphene oxide[16]; a free standing graphene accommodates oxygen on the top and the bottom of the basal plane. In contrast to the literature values our study reports high carbon content. This could be attributable to the fact that the oxygen gets attached only to the top surface of graphene because graphene is supported on Ru(0001). In addition, the surface characterization also was done using XPS, where the Ru(0001) and graphene/Ru(0001) did not show traces of oxygen, while the oxygenated graphene surface did show a significant oxygen peak in XPS (figure 45). In addition, the intercalation of oxygen during the graphene oxide synthesis could be ruled out- as there was no change observed on the graphene surface as evidenced by the carbon-AES peak; intercalation of oxygen can lead to the corrugation of the graphene surface, where the carbon-AES peaks could be different in the presence of oxygen intercalation compared to a pristine graphene (figure 46). Although the presence of oxygen was confirmed by AES, the chemical environments of oxygen was not studied due to the lack availability of high resolution XPS.

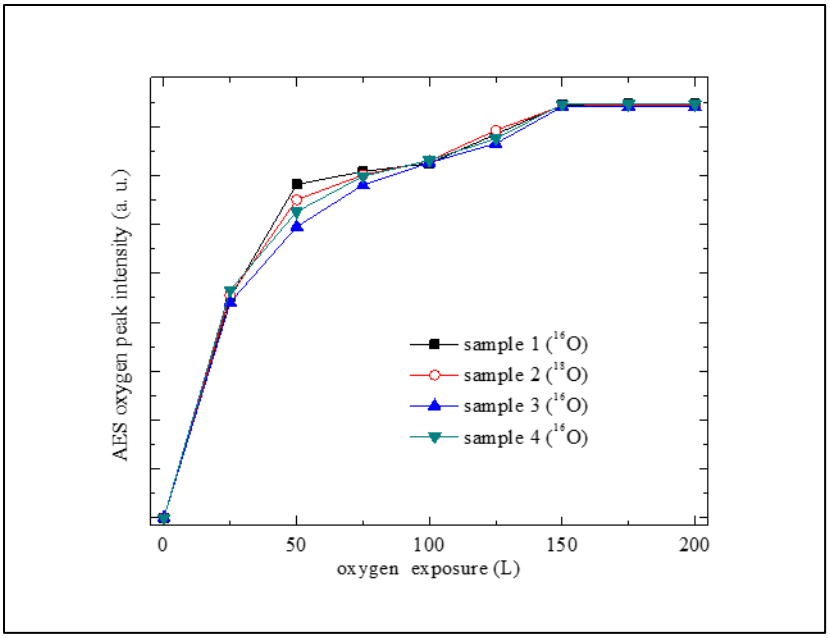

Figure 44. Change in oxygen peak intensity in AES as a function of oxygen coverage

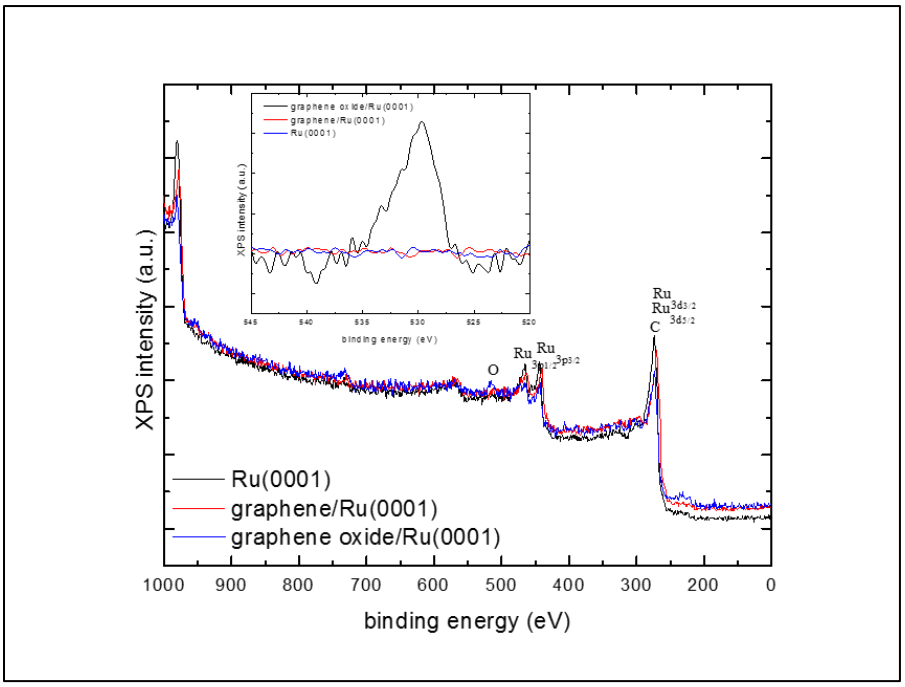

Figure 45. XPS shows the presence of oxygen in graphene oxide/Ru(0001). Inset shows the oxygen region

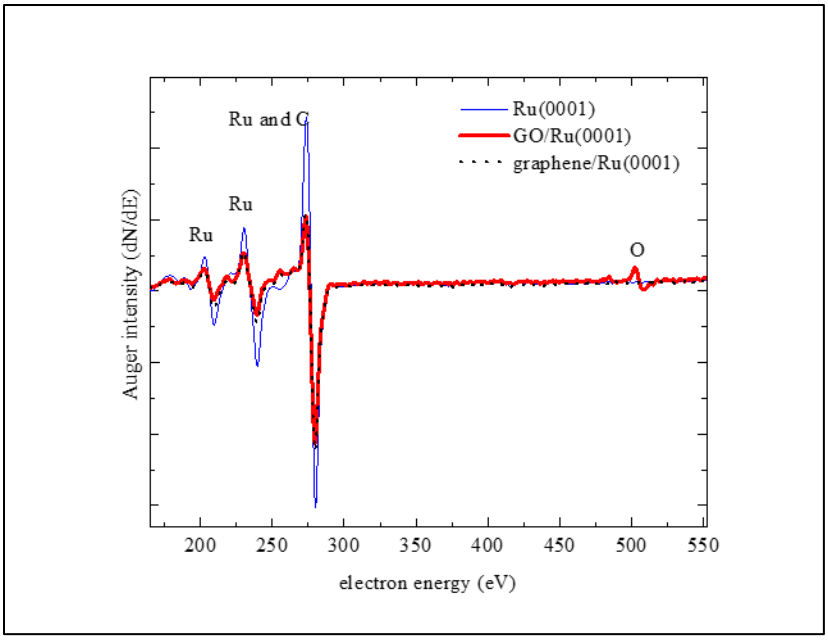

Figure 46. AES shows no intercalation of oxygen during graphene oxide synthesis

3.4. Adsorption kinetics experiments

Adsorption kinetics was studied by TDS. The instrumentation of TDS is described in chapter 2. All the TDS experiments were carried out by cryogenically cooling the surface with l-N_2 and when needed with He-bubbling. The sample temperatures reached 90 K with l-N_2 cooling, while the temperature decreased to about 85 K with additional He-bubbling; l-N_2 freezes at 77.2 K and l-He freezes at 4.2 K. Mostly, l-N_2 is used for cooling the system and l-He is used to achieve temperatures below the freezing of l-N_2. For molecules such as water and n-alkanes the cooling was carried out exclusively with l-N_2. However, for carbon dioxide an additional He-bubbling was carried out to obtain low temperatures to facilitate condensation; carbon dioxide condenses at 80-85 K. The parent mass was detected for the molecules of interest. A linear temperature ramp at a heating rate of 1.6 K/s was consistently used for all the experiments. The data analysis was carried out using a Redhead equation as described in chapter 2.

3.5. Adsorption dynamics experiments

Adsorption dynamics experiments were carried out using molecular beam scattering techniques. The molecular beam scattering experiments utilized a supersonic molecular beam with molecules of interest. Seeded beam was used to create n-butane beam (He/n-butane) and carbon dioxide beam (He/CO_2) for the studies described in chapters 6 and 7, respectively. The King and Wells type experiments were carried out to measure the adsorption probabilities. In addition, the adsorption probabilities were also studied by varying the surface temperature and the impact energy of the molecule. The impact energy of the molecule of interest was adjusted by increasing the nozzle temperature and the nozzle temperatures were converted to impact energies, using time-of- flight (TOF). The surface temperature was increased by resistively heating the sample through a W- filament.

CHAPTER 4. ADSORPTION KINETICS OF WATER ON CVD AND PVD GRAPHENE

4.1. Introduction

This chapter describes the adsorption kinetics of water on two different types of graphene. Chemical vapor deposited (CVD) graphene and physical vapor deposited (PVD) graphene are used in this study. The wettability of graphene and the support effects are studied. The motivation of this study is due to the fact that graphene can be used as a potential material for protective coating due its atomic layer thickness, strechability, flexibility, and higher conductivity. Introducing a layer of graphene as a coating can protect the underlying substrate from harsh environmental conditions such as moisture. The wettability of graphene is addressed in a few studies through contact angle measurements. However, contact angle measurements do not determine the intrinsic surface properties due to the uptake of contaminants from the atmosphere with time. Thus, the studies that reported the wettability of graphene through contact angle measurements are contradictory. Considering the contradictions in the literature, a more precise method would be to study the wettability of graphene in the absence of airborne contaminants. Therefore, this chapter focuses on the adsorption of water on graphene under atomically clean environment (ultrahigh vacuum conditions).

CVD graphene (graphene/SiO_2 and graphene/Cu) and PVD graphene (graphene/Ru(0001)) were used in this study. Adsorption kinetics was studied using thermal desorption spectroscopy (TDS) to study the hydrophobicity (or hydrophilicity) and the support effects towards water adsorption. This study showed that the graphene is semi-transparent to wetting and the wetting is dictated by the substrate underneath. This chapter is composed of a brief literature review followed by the experimental and results and discussion of adsorption kinetics of water of CVD and PVD graphene.

4.2. Literature review

Coatings are used to protect electronics devices from harsh environmental conditions on metals and semi-conductors. The potential material for such coating should be strong yet ductile, hydrophobic, and ultrathin. Graphene is a promising material as a protective coating; graphene is tough and flexible, interacts weakly with water because it prevents the hydrogen bonding with water, and most importantly graphene is an atomic layer thick material.[62-63] It is vital to study the water-graphene interaction because the graphene based coatings will be exposed to ambient conditions. The wettability of graphene was studied using contact angle measurements, in several studies.[64-68] However, the studies reported contradictory findings for contact angle measurements in the water wetting of graphene. The findings varied from the transparency[65,67] of graphene to partial transparency (translucency (semi-transparency))[66] of graphene and the non-transparency[64] of graphene. The discrepancy in the wetting property of graphene is due to the uptake of airborne contaminants (volatile hydrocarbons), which can result in the contradictory measurements of contact angle.[69]

Wetting transparency of graphene can be defined as, the identical interaction of water-graphene and water-substrate.[67] Introducing a layer of graphene on a substrate should not alter wetting of the substrate. Generally, hydrophobic surfaces act as insulators and adding a graphene coating should result in a conductive hydrophobic surface.[65,66] The wetting transparency was first reported by Rafiee et al.[65], where the contact angle measurements for water wetting was studied on substrates (Si and Cu) and on single layer graphene supported on Cu and Si. The contact angle measurements showed that the introduction of a mono layer of graphene did not significantly affect the contact angle (1-2% effect on contact angle). Furthermore, the same study measured the contact angle by increasing the number of monolayers of graphene. A significant increase in contact angle

was seen for 4-6 layers of graphene and beyond 6 mono layers the contact angle was unaffected. This study showed that the addition of a mono layer graphene, with a thickness of 0.34nm, did not affect the wetting of the substrate and concluded that graphene is a transparent material to wetting. A similar study was reported with Cu and SiO_2 substrates and a mono layer graphene on these supports.[67] The contact angle measurements were in agreement with Rafiee et al. Overall, both these studies showed that the graphene is transparent to wetting and the wettability is independent of the substrate.

In contrast to the wetting transparency, Shih et al.[66] reported a breakdown in the wetting transparency of graphene. Unlike the previous studies where the contact angle measurements were done between 30˚ and 90˚, this study was carried out for extreme cases of the substrate; super hydrophilic (θ=0˚) and super hydrophobic (θ=180˚) substrates were studied to examine the wetting property of graphene. A super hydrophilic substrate, where the water-substrate interaction is high, showed graphene to be transparent. On the other hand, a super hydrophobic substrate (weak water-graphene interaction) makes graphene opaque. Furthermore, the same study showed that the van der Waals interaction potential was reduced by 70% by adding a layer of graphene on substrate and only 30% of van der Waals interactions is transmitted through the graphene layer. Therefore, contradictory to the previous two studies, the findings reported by Shih et al clearly showed that graphene is translucent to wetting and the wetting is influenced by the substrates.

The contradictions on the wettability of graphene needs more insights to address the intrinsic wetting properties. Since the studies reported previously used contact angle measurements to study the wettability of graphene and eliminated the effects and contributions of contaminants-it is important to see the effects of airborne contaminants on the wettability of graphene. Li et al.[69] studied the effect of volatile hydrocarbons on the contact angle measurement. As prepared

graphene/Cu showed hydrophilicity- with a contact angle of θ=44˚. However, when the graphene/Cu was exposed to air for 20 minutes and then to 24 hours the contact angle drastically changed from θ=60˚, at 20 minutes, to θ=80˚, at 24 hours. In addition, a simultaneous Fourier transformed infrared spectroscopy (FTIR) measurement showed an increase in the $–CH_2$ and $–CH_3$ stretch at 2850 cm^{-1} and 2950 cm^{-1}. Furthermore, XPS showed a shoulder peak at 287.6 eV in addition to the carbon peak at 285.7 eV. Both, FTIR and XPS showed the uptake of hydrocarbon from the air when the graphene/Cu was exposed to ambient conditions. Therefore, the discrepancy in the literature on the wetting behavior of graphene is attributable to the presence of airborne contaminants.

The intrinsic interaction of water-graphene and water-substrate will serve as a paradigm to address the contradictions in the wettability of graphene. However, the literature lacks such kinetics study on a graphene surface. Studying the wettability of water under atomically clean conditions, such as ultrahigh vacuum conditions, will provide the insights of the innate interactions of water on both graphene and substrate. Therefore, in this study CVD and PVD graphene were subjected to water adsorption under UHV conditions. The adsorption kinetics of support and supported graphene was studied individually and the wetting behavior was compared with among supports and graphene/support. The preparation and characterization of the CVD and PVD samples are explained previously in chapter 3.

4.3. Adsorption of water on CVD and PVD graphene

Adsorption of water was measured for Cu, SiO_2, graphene/Cu, graphene/SiO_2, and graphene/Ru (0001). The water adsorption was not studied for Ru (0001) because it is a well-studied surface and hence literature data were used for comparison. Water was dosed on a cryogenically cooled surface (T≈95K). The TDS was recorded at different exposures of water

($1x10^{-6}$ Torr for 1 second corresponds to 1Langmuir (1L)). The heat of sublimation of water was calculated using Arrhenius equation.

4.4. Results and discussion

TDS allows to distinguish between hydrophobic and hydrophilic surfaces. Table 1 shows different surfaces, which possess hydrophobic and hydrophilic characters. The hydrophobic surfaces are characterized by a single TDS peak, which corresponds to the condensation peak. In contrast, hydrophilic surfaces usually show multiple TDS peaks; multiple peaks can occur due to different binding sites on the surfaces.

Table 1. List of hydrophobic and hydrophilic systems studied using TDS[70]

Hydrophobic systems			
System	**Hydro-phobic**	**0^{th} order**	**TDS peaks**
Au(111)	Yes	Yes	1
Antimony(111)	Yes	Yes	1
Cu(111)	Yes	Yes	1
O_2-Au(111)	Yes	Yes	1
D_2-Ni(111)	Yes	Yes	1
D_2-Pt(533)	Yes	Yes	1
Octane-Pt(111)	Yes	Yes	1
Water-Pt(111)	Yes	Yes	1
Hydrophilic systems			
Ru(0001)	No	No	3
JSC-A1	No	No	5
TiO_2(110)	No	No	3
Pt(111)	No	No	2

The TDS for SiO_2 and graphene SiO_2 is shown in figure 47. Zeroth-order kinetics is evident for SiO_2 already below monolayer completion because the leading edges at the sub monolayer coverage align and there is an abrupt drop in the high temperature edges. In addition, there is only one condensation peak, which shifts towards high temperature with increasing water coverage. In contrast to SiO_2, graphene/SiO_2 shows non zeroth-order kinetics for water adsorption at sub

monolayer coverages. The leading edges do not align at lower coverages and the desorption temperature shifts to lower temperatures with increasing coverage. The lowering of desorption maxima with increasing coverage is attributable to the defects on the graphene/SiO_2 surface although the defect density is <5% according to Raman spectroscopic analysis (chapter 3). Nevertheless, at exposures greater than 1.5L, the leading edges align and the desorption temperature shifts towards higher temperature- showing a zeroth order kinetics. At exposures greater than 1.5L, multilayer formation of water could occur, which shifts the desorption maxima to higher temperature. SiO_2 and graphene/SiO_2 do not show similar behavior for water adsorption, in other words, the support (SiO_2) and the graphene/SiO_2 do not mimic each other in terms of water adsorption; graphene is not transparent to water adsorption. Zeroth-order for SiO_2 and non-zeroth order for graphene/SiO_2, clearly shows the non-transparency of graphene for water adsorption.

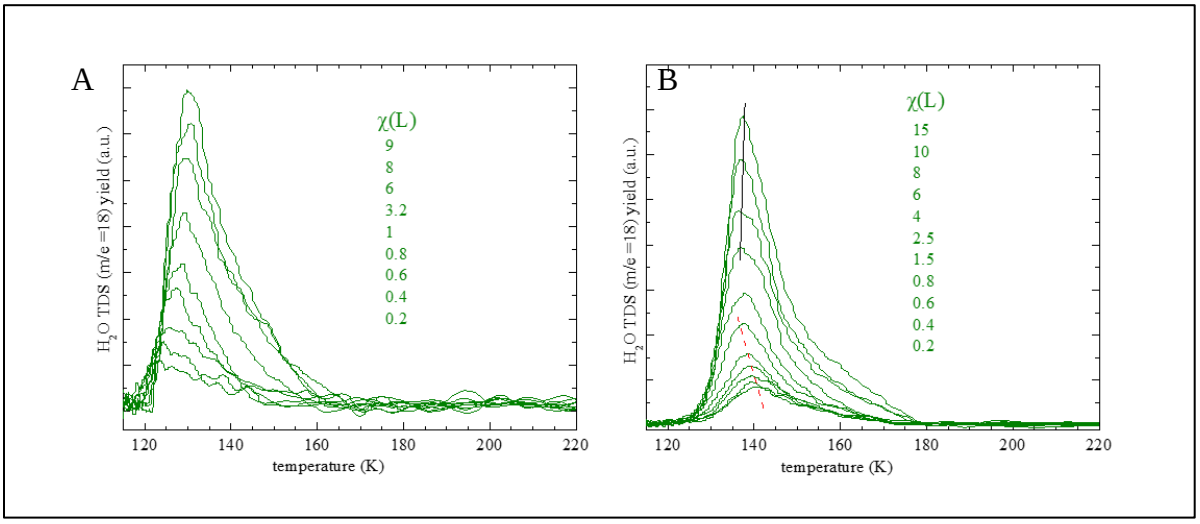

Figure 47. A. Water TDS of SiO_2 support. B. Water TDS of graphene/SiO_2

Adsorption of water on a Cu support and graphene/Cu is depicted in figure 48. Cu tends to show both hydrophobic and hydrophilic behavior depending on the crystallographic orientation; except Cu (111) all other Cu show hydrophilic character. The Cu used in this study is a polycrystalline support, which has not been studied in the literature. The TDS shows, a broader

feature with a non-aligned sub mono layer leading edges. Collectively, the polycrystalline Cu shows non-zeroth order kinetics. In contrast, graphene/Cu shows a zeroth order kinetics at sub mono layer coverages. Comparison of water adsorption on Cu and graphene/Cu shows that graphene is not transparent to water adsorption.

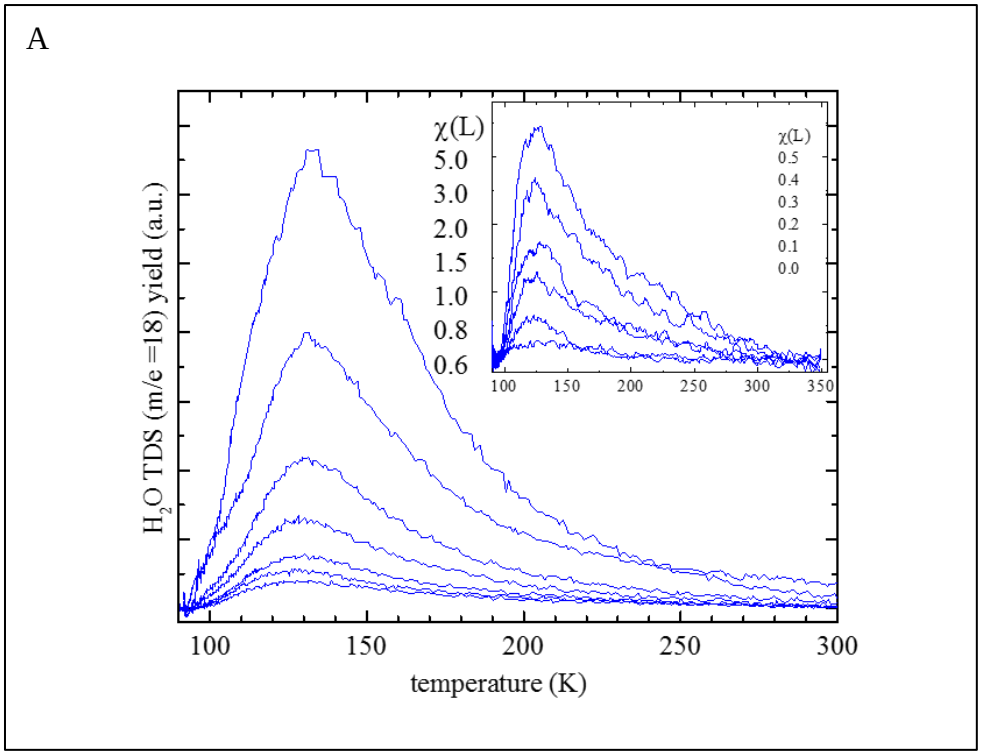

Figure 48. A. Water TDS of Cu support. B. Water TDS of graphene/Cu

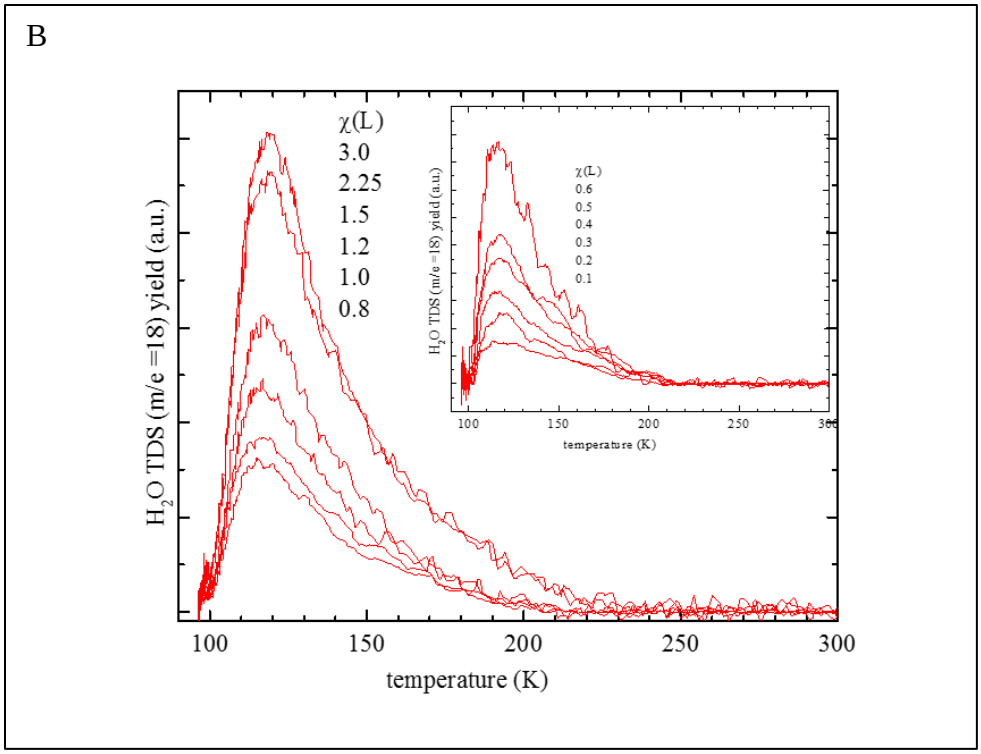

Figure 48. A. Water TDS of Cu support. B. Water TDS of graphene/Cu (continued)

Graphene grown on Ru (0001) through physical vapor deposition was subjected to water adsorption. Ru (0001) shows multiple peaks.[71-73] Three peaks are observed for water desorption from Ru(0001): higher temperature peak (225K) corresponds to the chemisorbed water layer, which is in direct contact with Ru(0001) metal, the second peak at 200K is attributable to the second layer, which is adsorbed above the first layer, and the third peak at lower temperature (160K) is due to the ice-like multilayer of water. Unlike Ru(0001), graphene/Ru(0001) showed a strictly hydrophobic behavior for water adsorption (figure 49). The leading edges at sub monolayer coverages were aligned (common leading edges) with an abrupt drop in the tailing edge. Furthermore, the desorption maxima shifted towards higher temperature, which corresponds to the multilayer formation of water; desorption temperature increases with the increased formation of multilayer. Therefore, Ru(0001) shows hydrophilic behavior and graphene/Ru(0001) shows

hydrophobic behavior for adsorption, which clearly shows that graphene is not transparent to water.

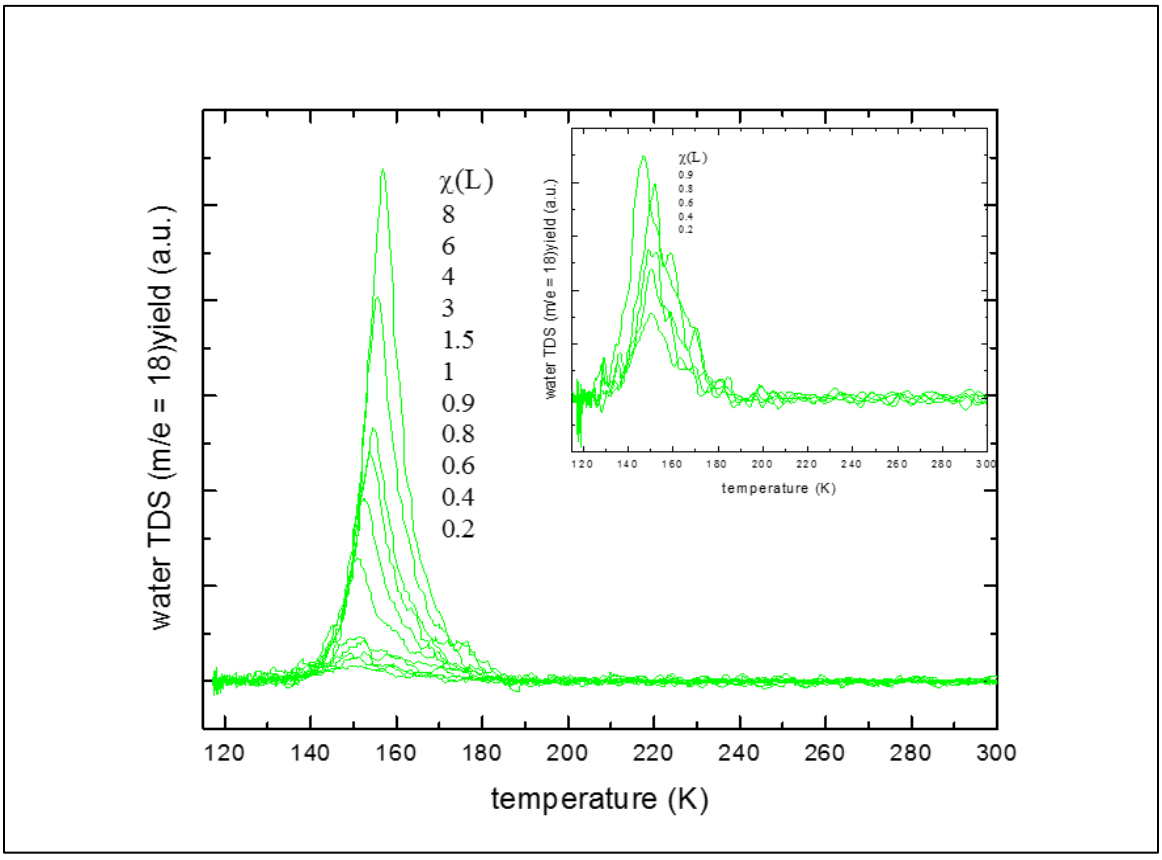

Figure 49. Water TDS of graphene/Ru(0001)

Wetting behavior of water is a highly debatable topic, which resulted in contradictory findings in the literature through contact angle measurements. This study, agrees with the breakdown in wetting transparency of water and/or the translucency of graphene. The TDS data clearly shows that the support perturbs the water adsorption on graphene. Furthermore, metallic (Cu and Ru) and semi-conductor (SiO_2) supports showed different behavior for water adsorption; the metallic supports were hydrophilic while the semi-conductor was hydrophobic. The wetting property of graphene on metallic and semi-conductor was reciprocally related, which means if the support is hydrophilic (metallic supports) then the water adsorption on graphene was hydrophobic,

and vice versa. Although TDS shows the non-transparent behavior of graphene, which agrees with literature, it could be possible that 30% of water-substrate interactions could be transmitted through graphene. Therefore, comparing this study with experimental (contact angle measurements), and DFT calculations[74-75], it could be concluded that graphene is not transparent to water adsorption and the substrate influences the water adsorption.

TDS allows to quantify the heat of sublimation of water. Arrhenius equation can be used to calculate the heat of sublimation of water. Arrhenius equation is given as[70],

$$k = k_d [A_{ads}]^0 = k_d \quad (21)$$

$$k_d = \nu e^{-E/RT} \quad (22)$$

$$\ln (k_d) = \ln (\nu) - E/R\ 1/T \quad (23)$$

here,

k_d desorption rate coefficient,

ν pre-exponential coefficient,

E binding energy (here sublimation energy of water),

T surface temperature,

$[A_{ads}]$ adsorbate coverage/concentration,

R gas constant,

Since the desorption order is coverage independent for zeroth order kinetics, Arrhenius equation can be written as,

$$\beta (d\Theta/dT) = k_d = \nu e^{-E/RT} \quad (24)$$

$$\beta r = \nu e^{-E/RT} \quad (25)$$

$$r = (\nu/\beta)e^{-E/RT} \quad (26)$$

$$\ln (r) = \ln (\nu/\beta) - E/RT \quad (27)$$

where,

β heating rate

dΘ/dT surface concentration

r desorption rate (mbar/T)

The TDS curves are used to plot the Arrhenius equation. The peak positions in Kelvin are plotted against the TDS peak intensities. The slope should be negative for zeroth order kinetics, while it is positive for non-zeroth order kinetics. The figure 50 shows the Arrhenius plots for graphene/Cu and graphene/Ru(0001). Unlike graphene/Cu and graphene/Ru(0001), graphene/SiO_2 shows a positive slope for sub monolayer coverage (non-zeroth order kinetics) and negative slope for higher coverage (6L), which is depicted in figure 51. The negative slope of the Arrhenius plots quantifies the heat of sublimation to be 0.46 eV/molecule, which is in agreement with the literature (0.49 eV/molecule). Thus, the Arrhenius plot not only gives the heat of sublimation of water, but also it represents the hydrophobicity and hydrophilicity through negative and positive slopes, respectively.

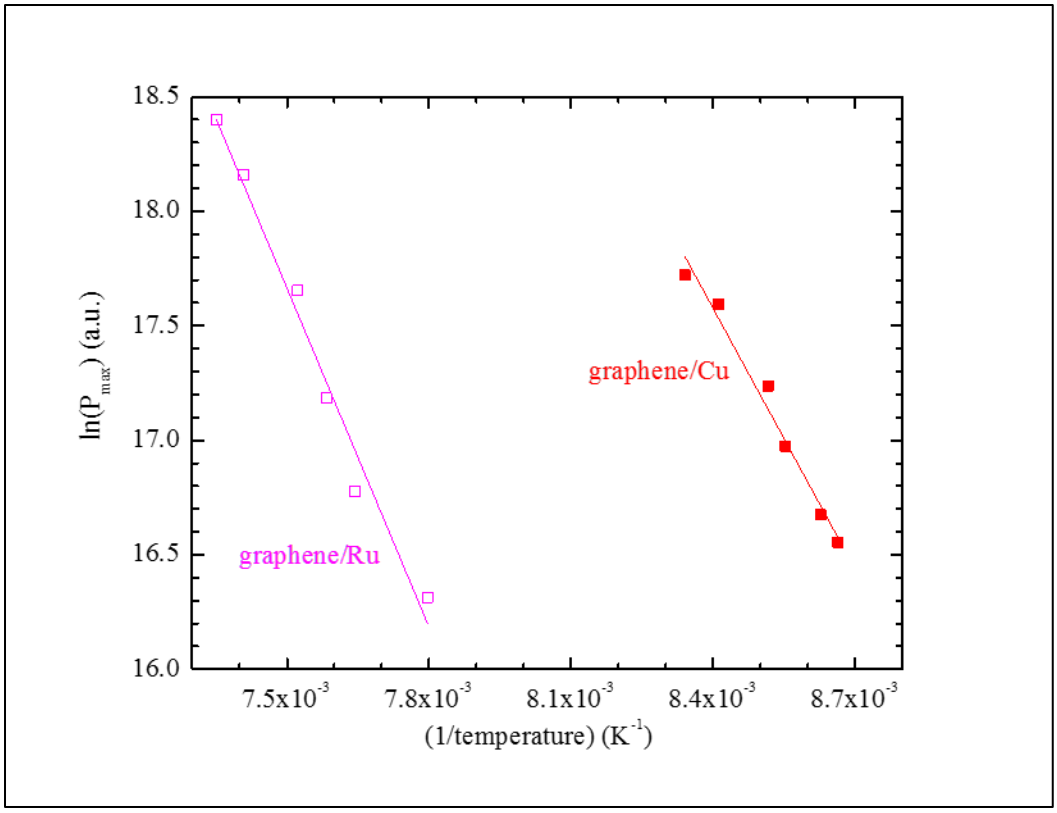

Figure 50. Arrhenius plot for graphene/Cu and graphene/Ru

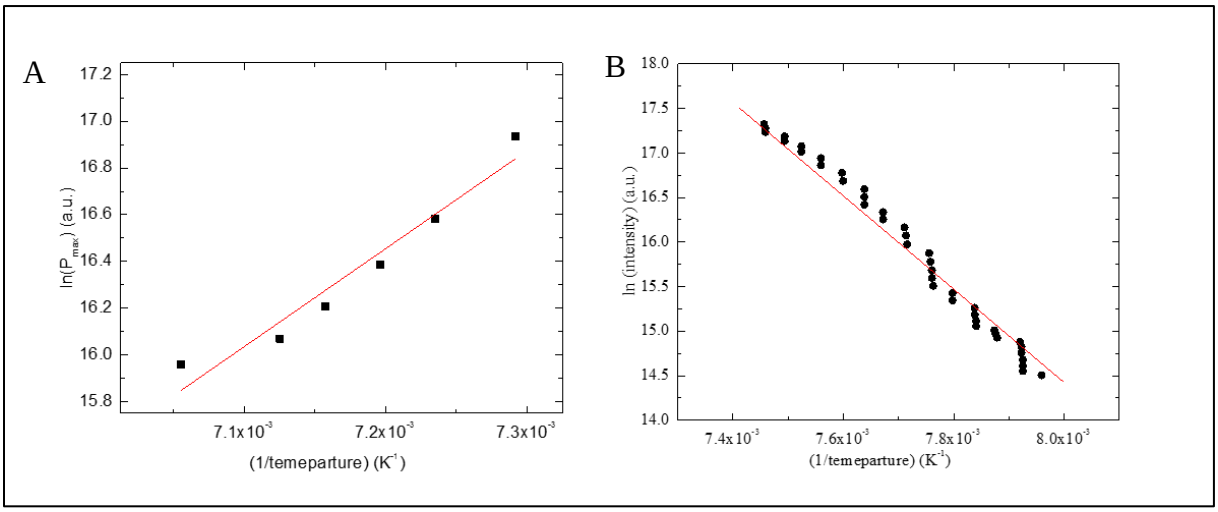

Figure 51. Arrhenius plot for graphene/SiO_2

4.5. Summary

Graphene is not transparent to water adsorption, which is shown by the TDS for support (SiO_2, Cu, and Ru(0001)) and supported graphene (graphene/SiO_2, graphene/Cu, and graphene/Ru(0001). The water TDS of support does not mimic the water TDS of graphene/support, proving the non-transparent behavior of graphene. Furthermore, the support influence on water adsorption was evident by the reciprocal behavior of support and graphene/support, i.e if the support was hydrophobic then the graphene/support was hydrophilic and vice versa. Therefore, graphene is not 100% opaque (non-transparent), but is translucent (semi-transparent) as the support effects are transmitted through the graphene layer. This is also supported by the DFT studies, where only 30% of van der Waals interactions are transmitted, making the graphene translucent.

CHAPTER 5. ADSORPTION KINETICS OF BENZENE ON CVD AND PVD GRAPHENE

5.1. Introduction

This study reports the adsorption kinetics of benzene on graphene on chemical vapor deposited (CVD) graphene and the findings are compared with physical vapor deposited graphene (PVD), carbon nanotubes (CNTs), and highly oriented pyrolytic graphite (HOPG). Benzene is an aromatic hydrocarbon, which is used as a prototype to study the carbon allotropes such as graphite, graphene, and CNTs. In addition, the non-covalent interactions (Π-Π interactions) of benzene on the carbon allotropes have substantial importance in biochemical engineering, electronics, and photovoltaics.[76-79] There were several theoretical studies (DFT calculations) reported on the interaction of benzene on graphene.[80-84] However, all these studies utilized the free standing graphene; benzene interaction on supported graphene has not been extensively explained in, both, theoretical and experimental studies. This chapter will explain the theoretical findings of benzene interaction with graphene and furthermore elaborates the insights of experimental findings on supported graphene. The support effects and the transparency of graphene for benzene adsorption was studied.

Supports (Cu and SiO_2) and supported CVD graphene (graphene/Cu and graphene/SiO_2) were used to study the adsorption kinetics of benzene. Thermal desorption spectroscopy (TDS) was used to qualitatively and quantitatively study the support effects and the transparency. The study showed that the graphene was transparent to benzene adsorption and in addition, the supports influenced the adsorption of benzene on graphene. The results were compared with the previous findings of benzene adsorption on HOPG and CNTs. The binding energies were similar to HOPG however, the binding energies were smaller than CNTs. The structure-activity relationship (SAR)

of this effect is explained under the results and discussion section. The findings of this study will serve as a basis for many fields, which utilize supported graphene instead of a free standing graphene.

5.2. Literature review

Benzene interacts with carbon allotropes through non covalent Π-Π interactions.[85] The interaction of benzene on such nanocarbons serve as a fundamental study to understand the intricate interactions of benzene derivatives in biochemical applications, photovoltaics, and electronics. The nucleobases (adenine, thymine, guanine, ad cytosine), can physisorb on graphene due to their aromaticity. The binding energy of gunanine on graphene is high (699 meV) compared to adenine (588 meV), thymine (545 meV), and cytosine (540 meV). The difference in the binding energies are attributable to the different functional groups in these nucleobases, which interact with graphene differently.[76-77] These interactions can be used to further understand the complex interactions of nucleic acids structures with graphene, which can be used to design biomolecule sensors. Beside biochemical applications, photovoltaics use benzene ring extensions for the improvement of photovoltaic properties. In addition, the polyaromatic hydrocarbons (PAHs), which evolve due to various anthropogenic sources- lead to environmental pollutions.[86] Designing carbon based sensors (graphene sensors) for such environmental pollution detection is an important application in the recent years. Overall, the aforementioned applications stem from benzene as a prototype, thus insisting the importance of studying the benzene interaction on nanocarbons.

The non-covalent Π-Π interactions of benzene on graphene can occur through either stacked configuration or hollow configuration (Figure 52). The DFT studies have shown that the stacked configuration is the most stable configuration of benzene on graphene. The distance

between benzene and graphene in a stable configuration is 3.4 Å. Benzene retains its planar configuration with C-C, C-H, and the C-C-C angle being 1.39 Å, 1.1 Å, and 120˚respectively; this is almost identical to the free standing graphene, which has C-C, C-H, and the C-C-C angle as 1.4 Å, 1.1 Å, and 120˚, respectively. The interaction of benzene with graphene is driven through the Π- electron clouds of graphene and benzene. The Π- Π repulsion is seen when benzene is adsorbed on graphene, which obstructs the benzene adsorption and forms a weak non covalent interaction. However, the weak interaction is yet strengthened by the CH-Π interaction, where the hydrogen on benzene points towards graphene. There is no evidence of band gap opening of graphene upon benzene adsorption. However, if the benzene is placed intentionally closer to the graphene at 1.56 Å the planar structure of benzene is destroyed, where the aromatic rings of benzene and graphene move towards each other with a band gap opening in graphene (0.8 eV). Thus, the innate interaction of benzene on graphene retains the planar structure of benzene and the zero band gap of graphene.[85,87-88]

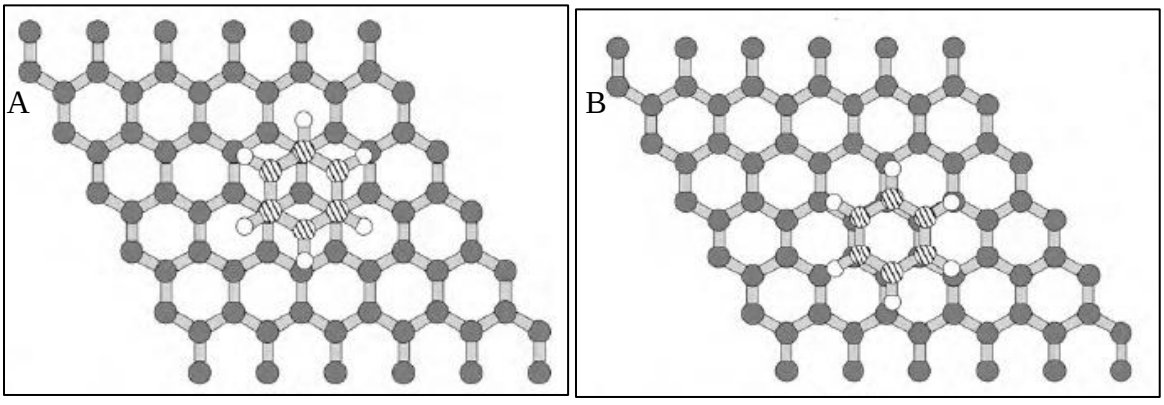

Figure 52. A. Stacked and B. Hollow configuration of benzene on graphene[80]

The interaction of benzene on various nanocarbons (fullerenes, CNTs, HOPG, and graphene) could be affected by the difference in their structures. Although, in all these nanocarbons the benzene interaction occurs through non covalent Π- Π interactions, the degree of interactions

is different. The binding energies of benzene on fullerene, fullerenes, CNTs, HOPG, and graphene is influenced by the diameter or the curvature of the molecule (figure 53). The binding energies of the nanocarbons decrease with increasing diameter or with reduction in the curvature; the binding energy of benzene increases as: graphene ≈HOPG< CNTs< fullerenes.[38,89] In addition, the CNTs have three different binding sites: internal, external, and the groves. However, the internal sites of CNTs have higher binding energies compared to grove and external as the internal sites are compact and they provide more binding sites for the adsorbates- enhancing the reactivity.

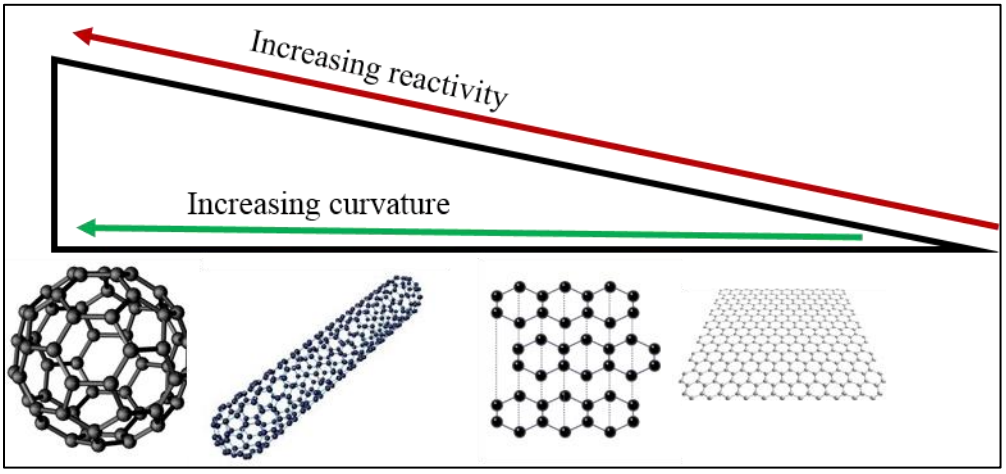

Figure 53. The reactivity of nanocarbons increases with increasing curvature or decreasing diameter[38,89]

Similar to the varied behavior of benzene adsorption on different nanocarbons, benzene derivatives could also have different binding strengths, compared to benzene, upon adsorption on graphene. The electron donating and withdrawing groups can influence the Π- Π interactions of benzene on graphene. On one hand, the presence of electron donating groups can increase the Π electron density on benzene, which can increase the Π- Π repulsion of graphene and benzene. On the other hand, an electron withdrawing group on benzene can reduce the Π electron density on benzene and thus enhance the interaction of graphene and benzene. Therefore, the derivatization of benzene plays an important role in the adsorption kinetics on benzene on graphene.[90-91]

Considering all the aforementioned factors into account, this study aims to address the transparency and the support effects of benzene on graphene. The transparency is qualitatively described using the peak shapes and positions of TDS and the binding energies are calculated to show the transparency. In addition, the binding energies are also used in addressing the support effects of graphene upon benzene adsorption.

5.3. Adsorption kinetics of benzene on CVD graphene and its supports

The adsorption kinetics of benzene was studied on Cu, Ru(0001), SiO_2, graphene/Cu, graphene/Ru(0001), and graphene/SiO_2. The binding energies were calculated using a well-known Redhead equation. In addition, the results are compared with free standing graphene, HOPG, and CNTs. All the experiments were carried out under UHV conditions (chapter 3) to ensure the atomically clean conditions.

5.4. Results and discussion

The adsorption kinetics of benzene (C_6D_6) was studied on the following surfaces: Ru(0001), Cu, SiO_2, graphene/Ru(0001), graphene/Cu, and graphene/SiO_2. Parent mass 84 was detected on all the surfaces except Ru(0001)- on which the benzene dissociates (chapter 3). The mass scan of the probe molecule (benzene in this case) is shown in figure 54. The background mass scan is included to show that the UHV system was free of any benzene traces.

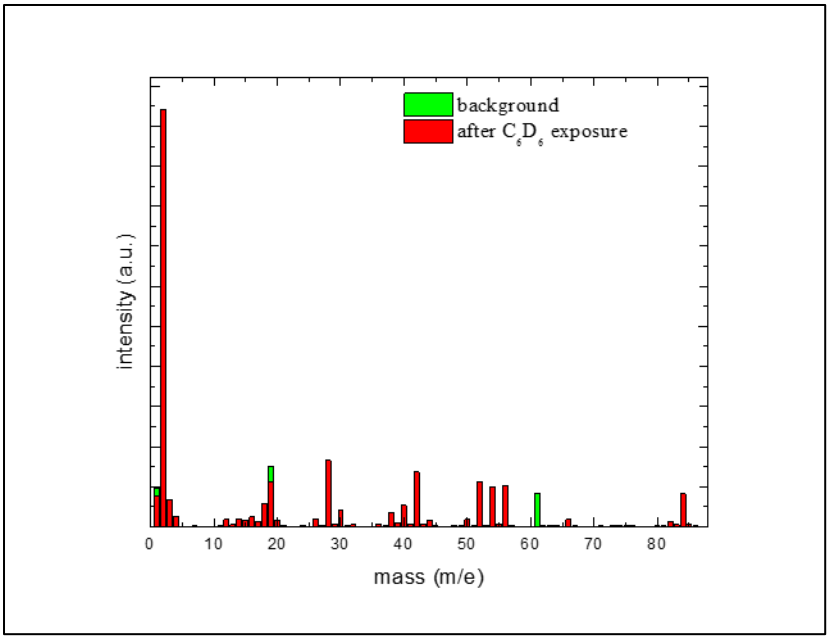

Figure 54. Mass scan of background and benzene dosed background

The TDS data for bare Cu and graphene/Cu is shown in figure 55. The TDS of bare Cu shows two distinct peak: α and β. The β peak at higher temperatures (230 K) corresponds to the defect sites of the polycrystalline Cu support. Once the defect peaks are covered with 1.1 L, the desorption peaks from the pristine surface (175 K) appears. The desorption peaks shifts towards lower temperatures with increasing coverages. This behavior is attributable to the repulsive lateral interactions, which arises due to the Π electron cloud of the benzene molecule. The Π electron cloud can destabilize the adjacent benzene molecule, shifting the desorption temperatures towards lower temperature. At coverages between 15 and 20 L, condensation starts to occur (c- peak), where the leading edges align, showing a zeroth order kinetics. Comparing the TDS of bare Cu with graphene/Cu, it appears only one TDS peak is present in graphene/Cu. The peak due to defects (β peak) is absent in graphene/Cu, which suggest that graphene/Cu does not have defects or negligible defects (pristine graphene). The desorption occurs at 180 K and moves towards lower temperatures; repulsive lateral interactions are accountable for the shifting of desorption

temperatures towards lower temperatures. The condensation occurs between 15 and 20 L, where the leading edges align. At a glance, the TDS of Cu and graphene/Cu looks different, qualitatively. However, the binding energy calculations show, that the binding energies for Cu and graphene/Cu are within the experimental uncertainty (figure 56). Therefore, from binding energy calculations, it is clearly seen that the graphene is transparent to benzene adsorption.

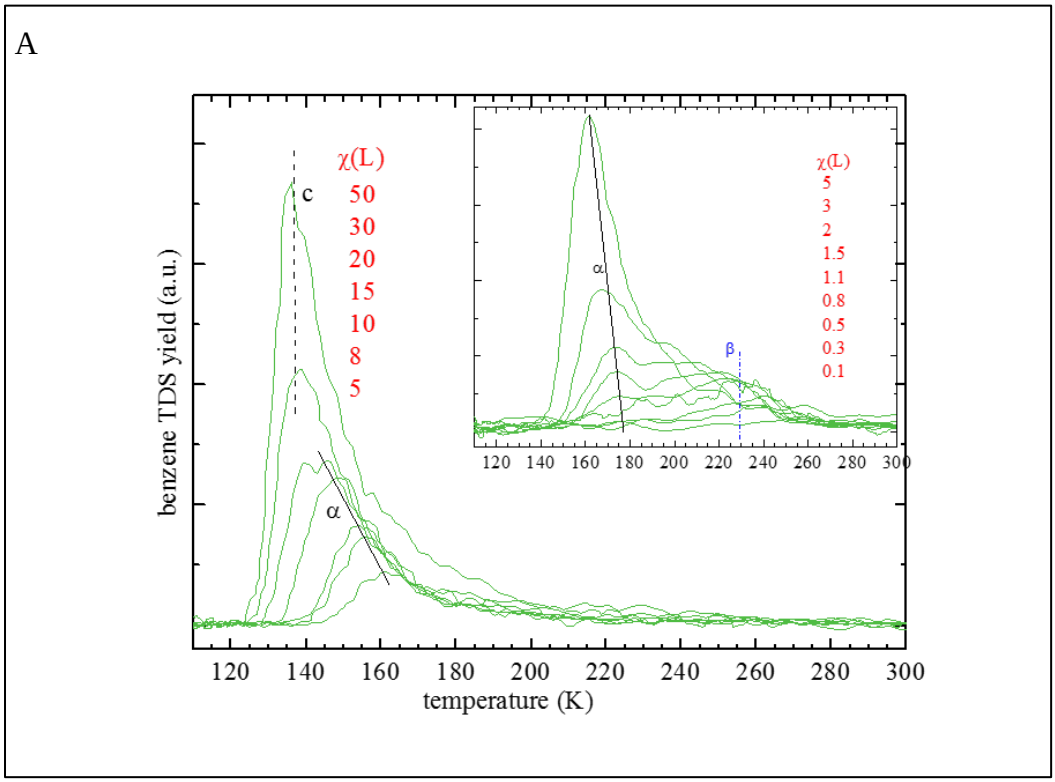

Figure 55. A. Benzene TDS of Cu and B. Benzene TDS of graphene/Cu

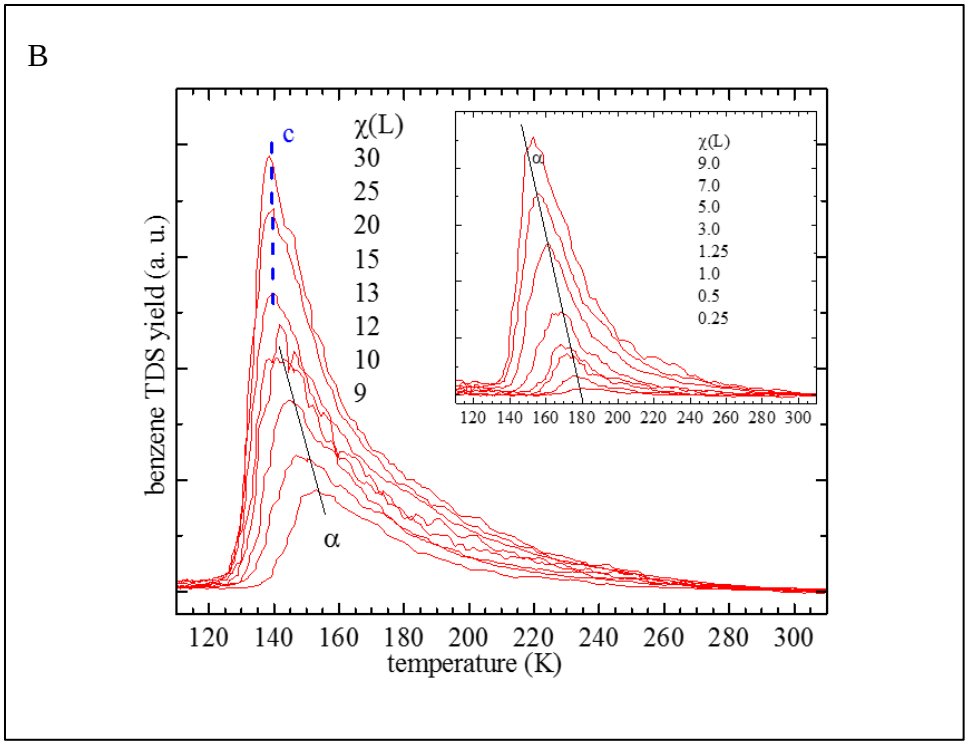

Figure 55. A. Benzene TDS of Cu and B. Benzene TDS of graphene/Cu (continued)

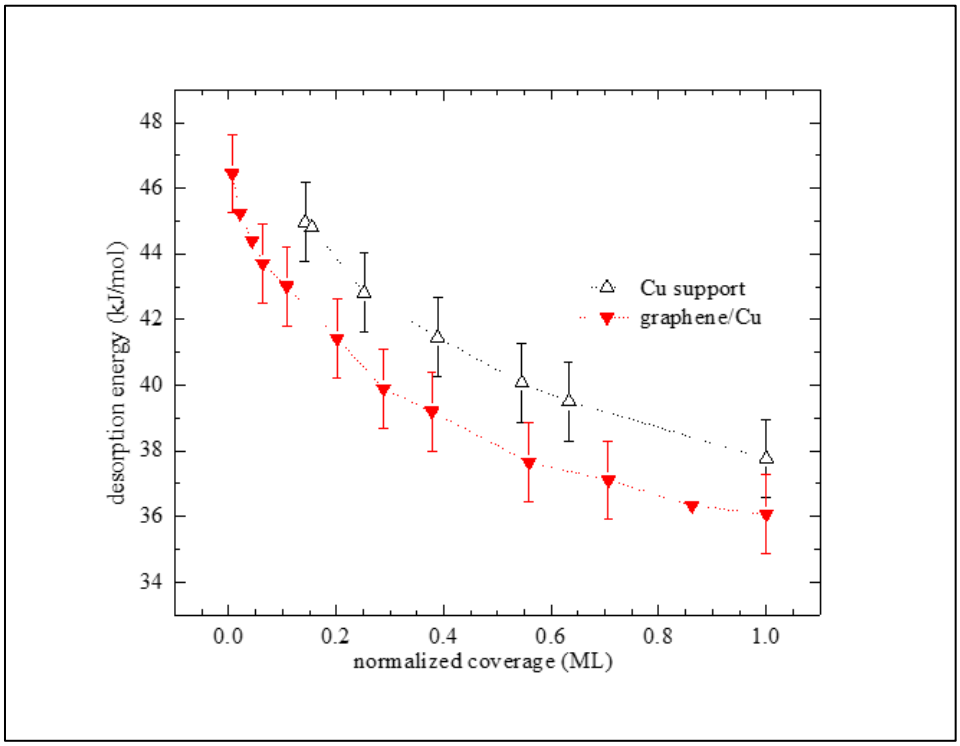

Figure 56. Binding energies of Cu and graphene/Cu

The adsorption kinetics of benzene on SiO_2 and graphene/SiO_2 is depicted in figure 57. Bare SiO_2 has one TDS feature- with desorption temperatures starting from 155 K and shifting towards the lower temperatures due to repulsive lateral interactions. The condensation occurs between 15 and 20 L with an alignment of leading edges. A similar trend is seen on graphene/SiO_2. However, comparing the binding energies of bare SiO_2 and graphene/SiO_2 (figure 58) shows that the binding energies at <0.1 ML, are slightly different for SiO_2 and graphene SiO_2 (38 and 42 kJ/mol respectively). The high binding energies of graphene/SiO_2 could be due to the defects present on the graphene surface (during transferring process in CVD), which, however, is not seen as a distinct peak in TDS. Other than <0.1 ML, the binding energies are within the uncertainties, suggesting that the graphene is transparent to benzene adsorption on SiO_2.

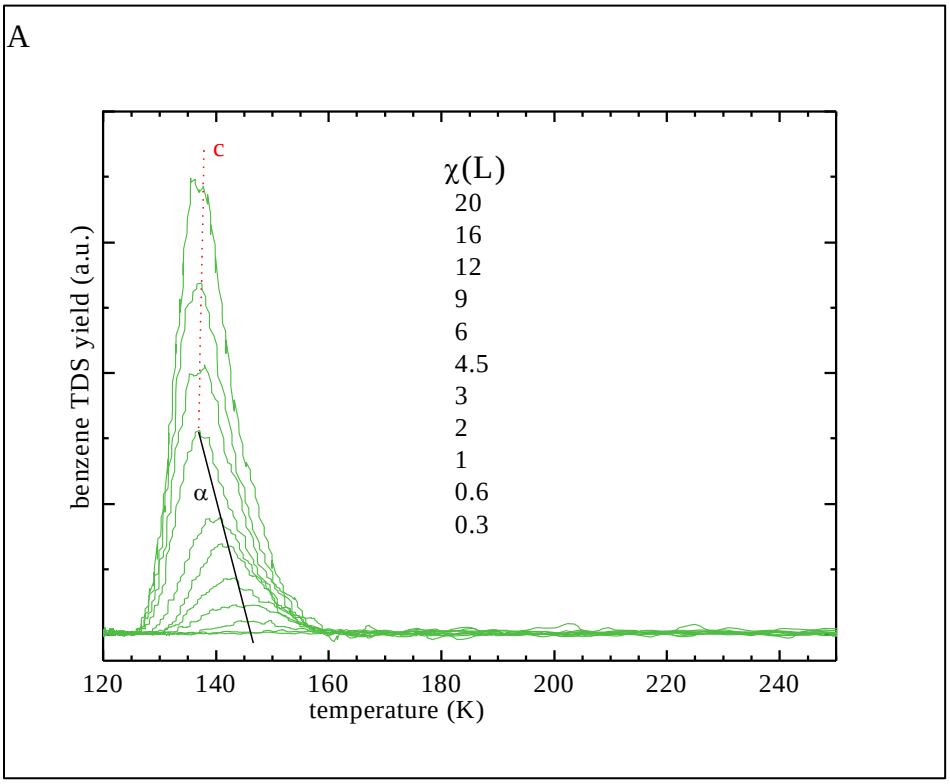

Figure 57. A. Benzene TDS of SiO2 B. Benzene TDS of graphene/ SiO_2

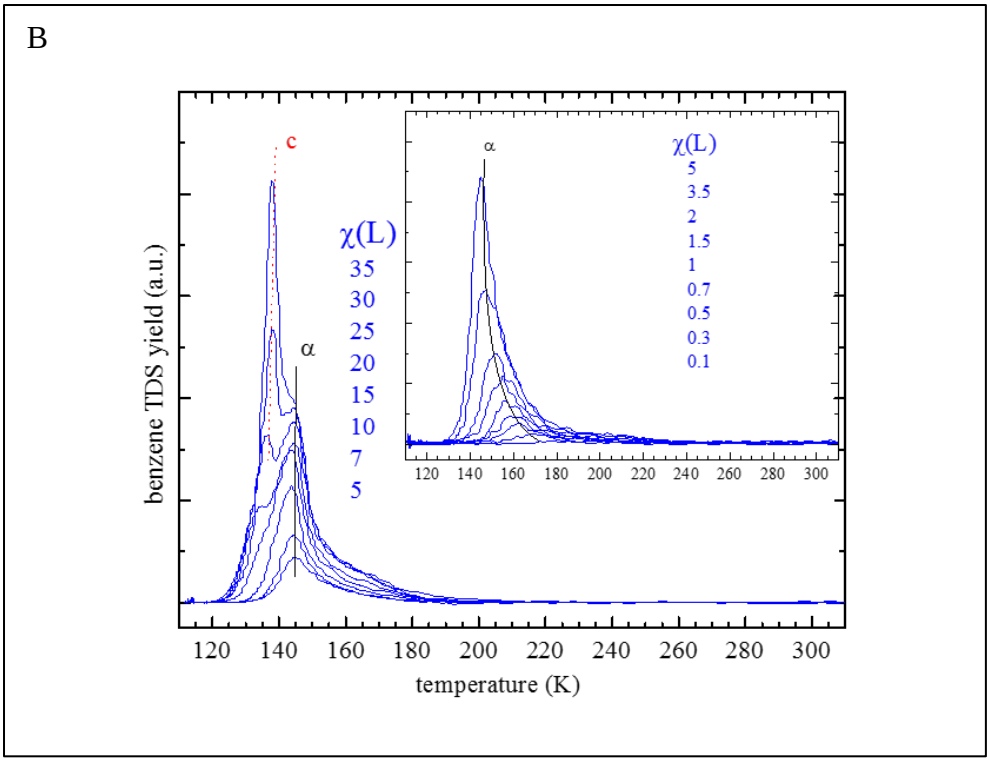

Figure 57. A. Benzene TDS of SiO2 B. Benzene TDS of graphene/ SiO_2 (continued)

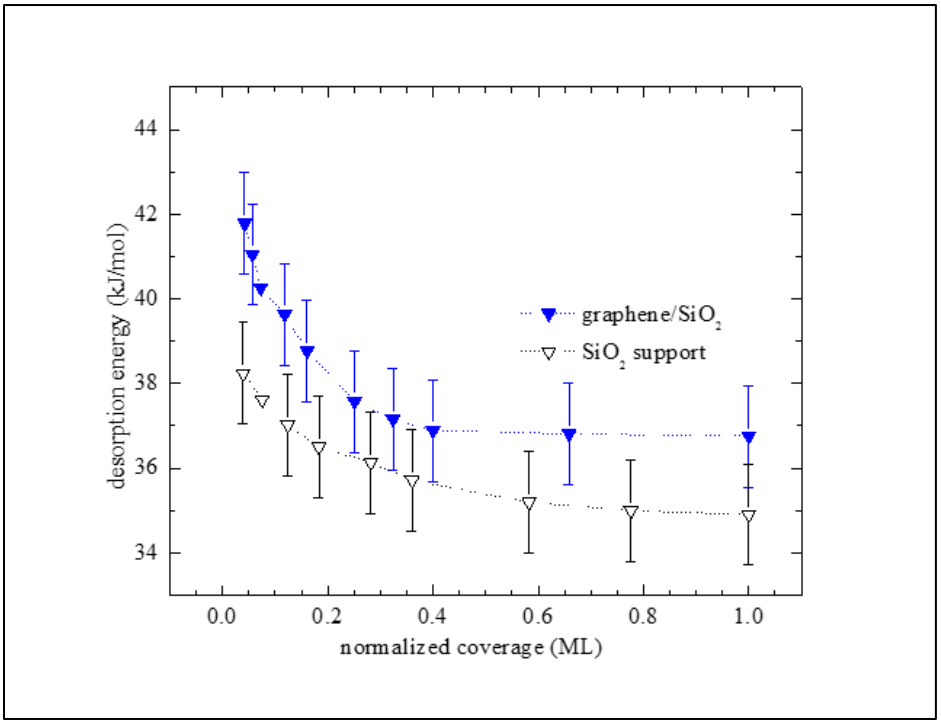

Figure 58. Binding energies of SiO_2 and graphene/ SiO_2

The contrast of benzene adsorption occurs on a reactive support, Ru(0001). Benzene dissociates on the active step sites of Ru(0001), which is explained in chapter 3 under graphene synthesis. However, the adsorption kinetics of benzene on graphene/Ru(0001) shows a desorption temperature starting from 180 K and moving towards lower temperature and finally condensing between 30 and 50 L (figure 59). The binding energy of graphene/Ru(0001) was 52.1 kJ/mol.

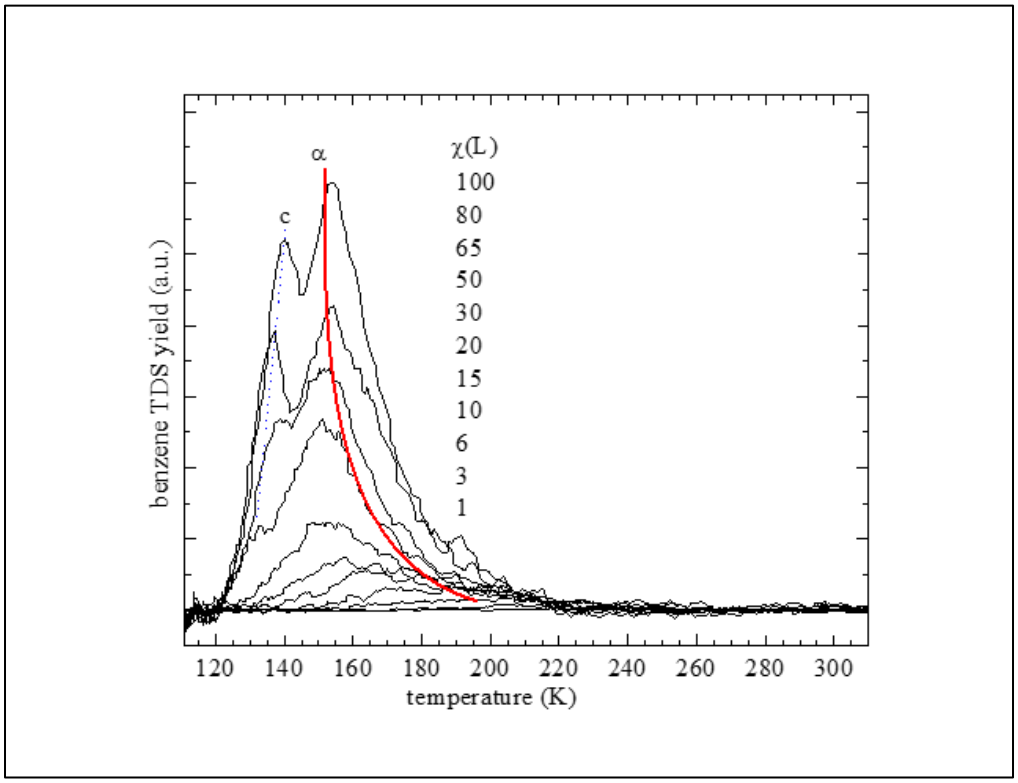

Figure 59. Benzene TDS of graphene/Ru(0001)[89]

The support effects were studied by plotting the binding energies of graphene/Ru(0001), graphene/Cu, and graphene/SiO_2 (figure 60). The highly reactive support (Ru(0001)) showed higher binding energy for benzene adsorption. The binding energies of benzene on graphene increased as, graphene/SiO_2<graphene/Cu<graphene/Ru(0001). The increased binding energy of graphene/Ru(0001) compared to other two supports could be due to the strong interaction between Ru(0001) and graphene; the strong interaction of Ru(0001) with graphene can reduce the Π

electron density in graphene. The reduced Π electron density can lead to enhanced adsorption of benzene on graphene as the Π- Π repulsion, between graphene and benzene, will be reduced. Thus, the degree of reactivity of the support with graphene dictates the adsorption kinetics of benzene on graphene. The binding energies of benzene on various surfaces are listed in table 2.

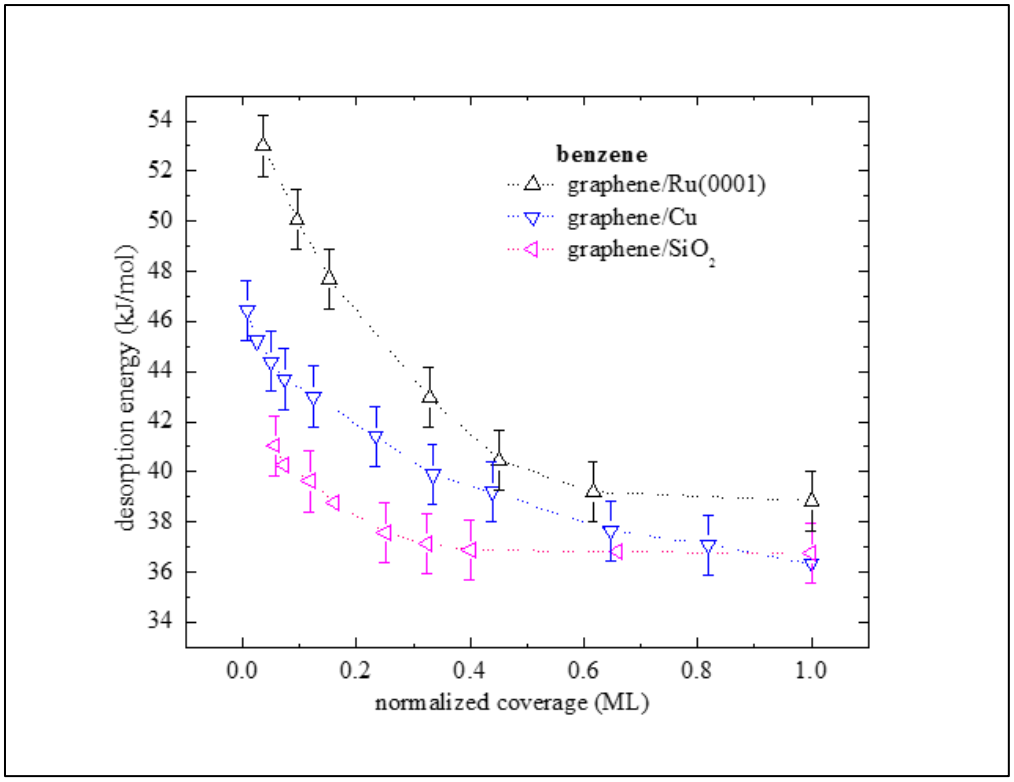

Figure 60. Binding energies for graphene/Ru(0001), graphene/Cu, and graphene/SiO_2

Table 2. List of binding energies on different surfaces[38,79,89]

Surface	Binding energy (kJ/mol)
HOPG	39 and 50
CNTs	
Internal	70-79
Groove	37-40
External	41-43
Free standing graphene	48
Graphene/Ru(0001)	52
Graphene/Cu	45
Graphene/SiO2	42

The adsorption kinetics of benzene is different on various nanocarbon. Interestingly, the binding energies of benzene on free standing graphene, CNTs, and HOPG are compared. The free standing graphene, with a most stable configuration (stacked configuration) showed a binding energy of 47.3 kJ/mol- according to DFT studies[85] (Table 2). The binding energy of benzene on free standing graphene was significantly different than supported graphene; support influences the adsorption of benzene on graphene. The CNTs showed a clearly different behavior for benzene adsorption (chapter 2, figure 15). The CNTs had three different binding sites: internal, groove, and external, which were seen as three different adsorption sites on TDS[38]. The binding energy of internal sites were high compared to graphene (Table 2) due to the increased availability of adsorbing sites for benzene. In contrast, the external sites were weakly adsorbing the benzene compared to graphene; the increased Π-Π interactions on external sites of CNTs could have resulted in weak binding of benzene. The binding energy of benzene on HOPG was similar to graphene[89]. Therefore, it can be concluded that, the adsorption kinetics of benzene depends on the

structure of nanocarbons and a high binding energy could be expected for a spherical nanocarbon (such as fullerene and CNTs) compared to planar nanocarbons (HOPG and graphene).

5.5. Summary

The adsorption kinetics of benzene on CVD graphene showed transparency of graphene. In addition, the support influenced the adsorption of benzene on graphene; the binding energies of benzene on graphene increased as: graphene/SiO_2 <graphene/Cu <graphene/Ru(0001). Not only the support, but also the adsorption kinetics is influenced by the structure of nanocarbons. The nanocarbons with increased curvature-deceased diameter (spherical structure: fullerene and CNTs) show enhanced binding energies compared to decreased curvature or increased diameter (planar structure: HOPG and graphene). The innate interactions of benzene on supported graphene showcased in this study can be useful in designing delicate interactions of benzene based derivative on graphene for multiple applications.

CHAPTER 6. ADSORPTION KINETICS AND DYNAMICS OF N-ALKANE ON CVD AND PVD GRAPHENE

6.1. Introduction

This chapter comprises of three projects: (1) the kinetic and dynamic transparency of graphene on Ru(0001) and graphene/Ru(0001) using seeded n-butane (2) effects of support on the desorption of n-pentane (3) chain length dependence of n-alkanes adsorption on graphene. The alkane adsorption plays an important role in, both metal and nanocarbon surfaces. The transition metals can act as catalyst for alkane synthesis, namely in the Fischer-Tropsch synthesis.[91] In addition, the interaction of n-alkanes on nanocarbon materials have possible applications in coatings, oligomeric adsorption-desorption, and a model for biomolecule adsorption.[92-94] All these applications call for a fundamental study of alkane interactions on both metal and nanocarbon surfaces. Thus, the n-alkane adsorption is studied on various surfaces.

A PVD graphene (graphene/Ru(0001)) and Ru(0001) are used in the first study. A molecular beam scattering technique, with seeded n-butane molecule, is used to study the kinetic and dynamic transparency of graphene. The second study employs the influence of support effects on n-pentane adsorption on graphene; both, CVD (graphene/SiO_2, graphene/Cu) and PVD (graphene/Ru(0001)) were used for this study. The third study was investigated to see the chain length dependence of n-alkane on graphene/Ru(0001). The findings of the three studies are discussed explicitly following the introduction section. The experimental involved in this study is described in chapter 3.

6.2. Literature review

Alkanes are saturated hydrocarbons, which can vary from one carbon (methane) to large number of carbon atoms (oligomers). One of the most robust method to synthesize alkanes is to

use the Fischer-Tropsch process (figure 1), which involves the formation of alkanes on a transition metal using water-gas shift reaction.[91] In such context, the interaction of n-alkanes with transition metals plays an important role in terms of adsorption-desorption of alkanes on transition metals. Besides, alkanes act as backbone to most biomolecules (amino acids, nucleic acids, lipids, and carbohydrates) making the alkanes an important class of organic molecules to act as a prototype to study the biomolecule interaction on various surfaces. In addition, alkanes are building blocks of large complex polymers; the interactions of large polymers on different surfaces can be simply studied by examining the adsorption-desorption properties of monomers (small alkanes), which constitute the large polymers.[93-94] Furthermore, the alkanes are used as lubricants for magnetic disks and can be evaporated overtime to affect the durability or life time of the magnetic disk. Thus, understanding the interactions of alkanes on such magnetic disk surfaces are an important aspect for disk fabrication. Moreover, alkanes are used in chromatographic column to create non-polar stationary phase (C18 chain).[93-94] Surprisingly, all the aforementioned applications involve the interactions of alkanes on nanocarbon surfaces (HOPG, CNTs, and graphene). Therefore, it is pivotal to study the interactions of small alkanes on the nanocarbons for futuristic applications.

$$CO + H_2 \leftrightarrow CO + H_2$$
$$H_2 + M \leftrightarrow H\text{-}M\text{-}H$$
$$CO + M \leftrightarrow M\text{-}CO$$
$$M\text{-}CO + M \leftrightarrow M\text{-}C + M\text{-}O$$
$$M\text{-}C + M\text{-}H \leftrightarrow M\text{-}CH + M \rightarrow MCH_2 + M \rightarrow M + MCH_3 \rightarrow MC_aH_b + MC_nH_m$$

Figure 61. Fischer-Tropsch synthesis mechanism (M is the metal)[91]

Transition metals act as catalyst to synthesize alkanes and also can contribute towards hydrogenation-dehydrogenation processes. The alkanes can diffuse over the active sites of transition metals and get trapped.[95-96] Once the trapped alkanes orient in a favorable confirmation, the C-H bonds can be activated and eventually dissociate. However, this trapping-dissociation

process is temperature dependent. At lower temperatures (T< 500 K) the alkanes molecularly adsorb on transition metals; at higher temperatures (T> 500K), the alkanes dissociate. In addition, the dissociation on a reactive surface can occur just above 500K, whereas the dissociation occurs at much high temperatures (T>1000 K) for less reactive metal surfaces.[97-100] Thus, the molecular adsorption and dissociative adsorption on transition metal surfaces have been a field of interest for many years.

Lately, nanocarbons have been exploited in many applications such as electronic device fabrication and sensors (bio sensors). Adsorption on such device fabrication plays an important role. The most commonly used nanocarbons involve HOPG, CNTS, and graphene. Alkanes interact on such nanocarbons through non-covalent CH-Π interactions. The DFT studies have shown that although the n-alkanes can interact, on the nanocarbons, in parallel or perpendicular (Figure 62) orientation, the parallel interaction (trans configuration) is the most favorable configuration. The stable conformation of n-alkanes on graphene has shown that the distance between alkane and graphene is around 3.4 Å. In addition, upon adsorption, the n-alkanes show very less deformation; the C-C bond length of free- state (gas phase) and an adsorbed phase varies only by 0.001 Å and 0.002 Å for n-pentane and n-nonane, respectively. Although the adsorption of n-alkanes on nanocarbons is non-covalent, the morphology of the nanocarbon can impact the adsorption properties resulting in different binding energies of n-alkanes on nanocarbons.[101]

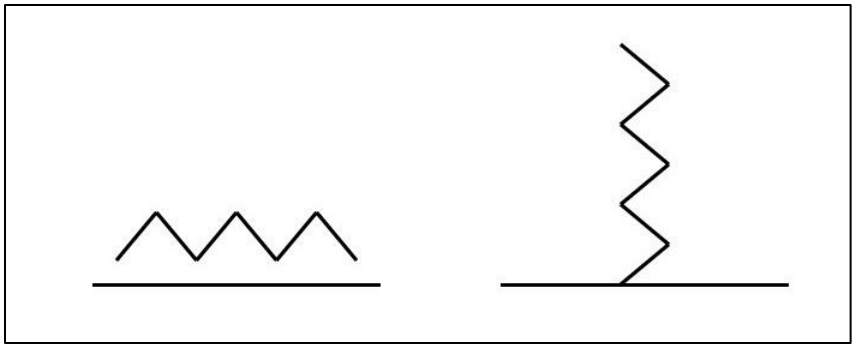

Figure 62. Parallel and perpendicular orientation of n-alkane on graphene[101]

The chain length of n-alkanes significantly impact the adsorption energy. The binding energy of the smallest n-alkanes (methane), for example, on the graphene surface amounts to 6.7 kJ/mol. The physical origin of this binding energy is attributable to the CH-Π interaction. Thus, with increasing chain length the binding energy should increase linearly; for the addition of each CH_2 group of alkanes, the binding energy should increase by 6.7 kJ/mol, theoretically.[101] In addition, the contribution of the end methyl group and the backbone methylene groups towards the binding energies is another aspect to be considered when quantifying the binding energy of n-alkanes. A comparison of linear and cyclic alkanes, of same number of carbon atoms, have shown that the binding energies are more or less the same, however, the linear alkanes showed 1-2 kJ/mol higher binding energies than the cylic alkanes.[102] The finding can be correlated to the presence and absence of the end methyl group in linear and cyclic alkanes, respectively. The difference of 1-2 kJ/mol binding energy in linear alkanes, could probably be considered as the contribution from the end methyl group. Thus, the end group of alkanes are also involved in binding, although a significant fraction of binding is due to CH-Π interactions.

As stated above, there is a clear motivation on studying the interaction of n-alkanes on, both, transition metals and nanocarbons. Therefore, the proceeding section showcases the interaction of various alkanes (straight chain alkanes: n-butane, n-pentane, n-hexane, and n-

heptane; branched alkane: iso-butane; cyclic alkane: cyclo-hexane) on graphene. The results are compared with previously reported HOPG[103] and CNTs[104]. The first study involves the interaction of seeded n-butane on Ru(0001) and graphene/Ru(0001). The results showed that n-butane adsorbs molecularly on, both, Ru(0001) and graphene/Ru(0001) and in addition it also shows that the graphene is both, kinetically and dynamically transparent- due to the similar binding energies of n-butane on Ru(0001) and graphene/Ru(0001). The second study looks at the binding energies of n-pentane on different supports (SiO_2, Cu, and Ru(0001)). The binding energy of n-pentane on graphene coated on different supports show that the support influences the binding; the highly reactive support (Ru(0001)) shows higher binding energy compared to moderate (Cu) and inert (SiO_2) support. The third study, maps the influence of chain length of n-alkanes on graphene/Ru(0001). A linear correlation is seen for the desorption energies of n-alkanes with increasing chain length. In addition, the effects of cyclic and branched n-alkanes on the desorption energies are studied.

6.3. Results and discussion

6.3.1. Adsorption of seeded n-butane on Ru(0001) and graphene/Ru(0001)

6.3.1.1. Adsorption kinetics of n-butane on Ru(0001) and graphene/Ru(0001)

The adsorption kinetics of seeded n-butane were studied on Ru(0001) and graphene/Ru(0001). The TDS curves for Ru(0001) and graphene/Ru(0001) are shown in figure 63. The desorption temperature for Ru(0001) starts at 150 K for lower coverage and decreases with increasing coverage; the graphene/Ru(0001) desorbs n-butane at approximately 145 K and decreases in desorption temperatures with increasing coverage. Although a first-order kinetics is expected for n-alkane desorption, coverage independent with no change in desorption temperature, the decrement of desorption temperature with increasing coverage could be attributable to the

repulsive lateral interaction of the adsorbates. Thus, the n-butane desorption shows a first-order kinetics with an exceptional behavior of decreasing desorption temperature with an increasing coverage as seen in some systems, which obey first-order kinetic process. At coverages of n-butane higher than 40 seconds and 35 seconds for Ru(0001) and graphene/Ru(0001), respectively a condensation peak starts to appear. The desorption kinetics shifts from first-order to zeroth-order with the leading edges aligning and the condensation peak shifts, insignificantly, to higher temperature indicates that higher temperatures are needed to desorb the condensed layer. The condensation occurs around 104 K, which is characteristics of the condensation of n-butane. In addition, the lower desorption temperatures of multi-layers compared to monolayer coverage indicates that adsorbate-adsorbate interactions are weaker than adsorbate-surface interaction. At a glance, the peak temperature, condensation time, and the desorption temperatures for, both Ru(0001) and graphene/Ru(0001) looks similar, which means qualitatively the graphene is kinetically transparent.

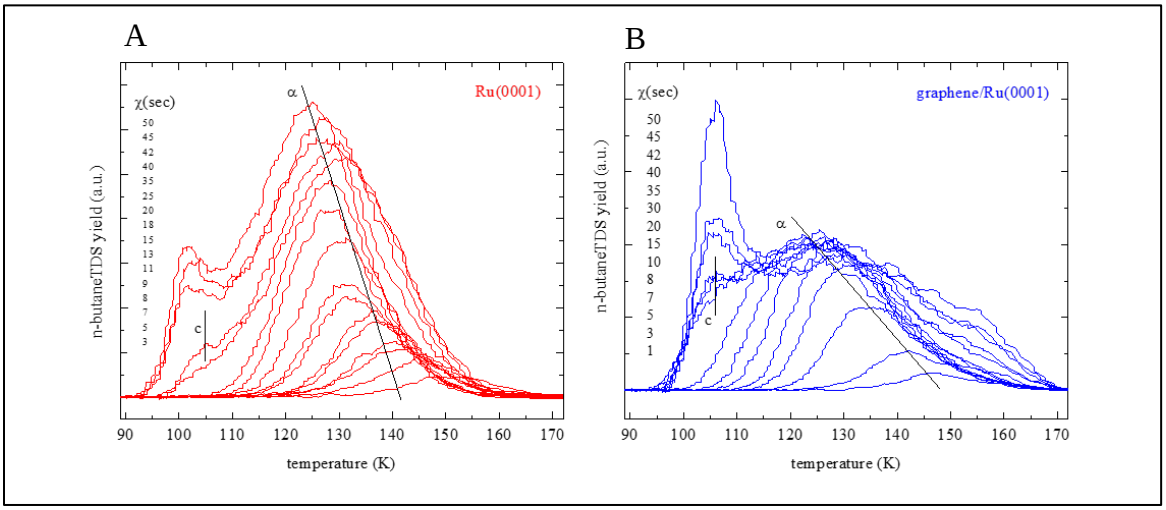

Figure 63. A. Seeded n-butane TDS of Ru(0001). B. Seeded n-butane TDS of graphene/Ru(0001)

A quantitative estimation of the coverage dependent binding energies of Ru(0001) and graphene/Ru(0001) is given in figure 64. The binding energies are within the experimental uncertainties for both system; the binding energy is nearly 1kJ/mol higher for Ru(0001). In addition, the decrease in the binding energy with increasing coverage is an evident for the repulsive lateral interactions until the monolayer formation. Thus, the desorption kinetics show, both qualitatively and quantitatively, that graphene is transparent to n-butane adsorption. Comparing the binding energy of n-butane on graphene/Ru(0001) (39.5 kJ/mol) with CNTs shows that the exterior of the CNT, which is comparable to the structure of graphene, has a lower binding energy (23 kJ/mol); the interior and groove of the CNTs have a binding energies 47.7 and 33.6 kJ/mol respectively.[104] The higher binding energy of graphene/Ru(0001) compared to the exterior of CNT could be due to the influence of support, where Ru(0001) is a highly reactive support. Besides, the dissociative or molecular adsorption of n-butane was examined by AES before and after n-butane adsorption on Ru(0001) and graphene/Ru(0001). As shown in figure 65, there was no evidence for n-butane dissociation; dissociation would have resulted in an increase of carbon peak (at 272 eV) upon n-butane adsorption. Thus, n-butane molecularly adsorbed on both Ru(0001) and graphene/Ru(0001).

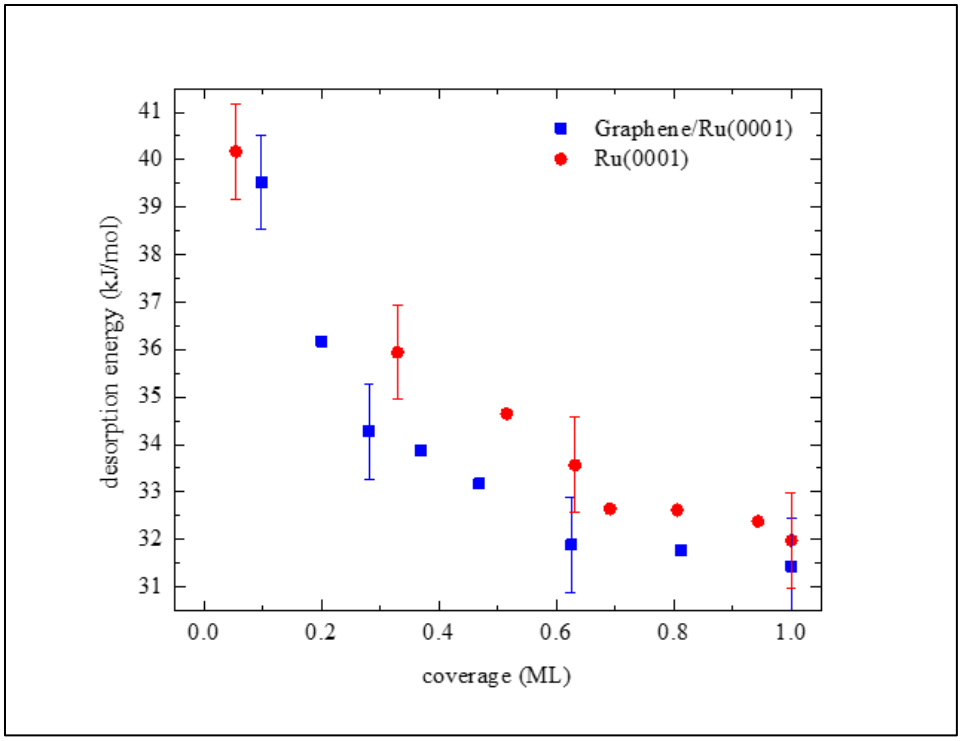

Figure 64. Coverage dependent binding energy for Ru(0001) and graphene/Ru(0001)

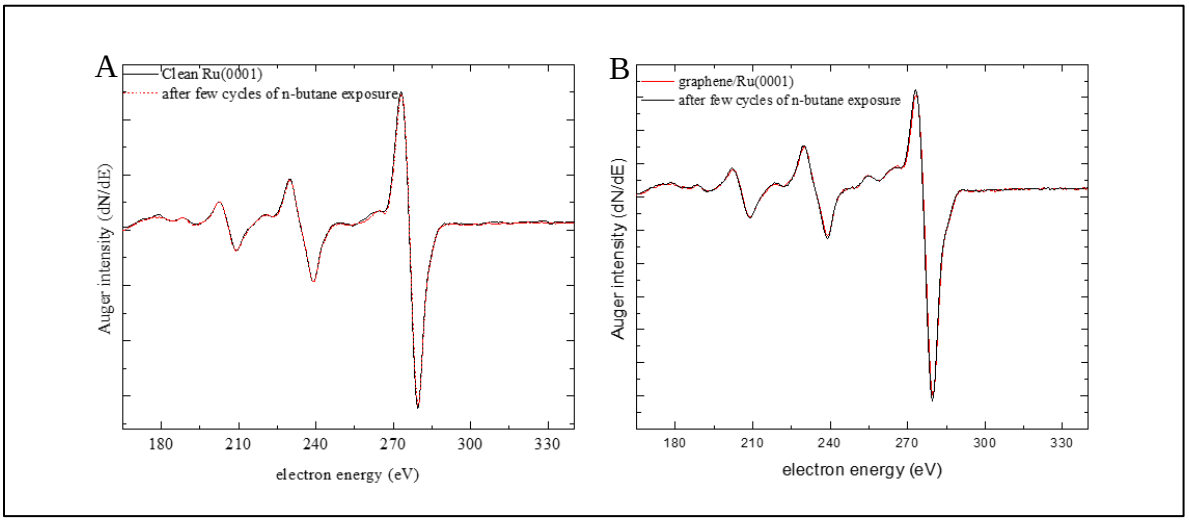

Figure 65. A. AES of Ru(0001). B. graphene/Ru(0001) before and after experiments

6.3.1.2. Adsorption dynamics of n-butane on Ru(0001) and graphene/Ru(0001)

The dynamic transparency of n-butane on Ru(0001) and graphene/Ru(0001) was studied by measuring the initial adsorption probabilities (S_0). Although a kinetically transparent material is also expected to be dynamically transparent, the hypothesis was tested by measuring the S_0. The S_0 was measured above the condensation temperature (T>104 K) because the condensation leads to saturation of the surface, which does not allow the adsorption probabilities to be measured. The surface temperature was increased from condensation temperature to higher temperatures at constant impact energies (E_i) as shown in figure 66. The S_0 decreases with increasing temperatures for, both, Ru(0001) and graphene/Ru(0001). The decrease in S_0 with increasing temperature is due to the non-activated molecular adsorption; for an activated adsorption an increase of adsorption probabilities will be seen initially. In addition, a drop in S_0 is seen at temperature higher than 120 K, which is consistent with the desorption temperature of n-butane on both surfaces. Moreover, the S_0 is within the experimental uncertainties for Ru(0001) and graphene/Ru(0001), which provides evidence that the graphene is dynamically transparent.

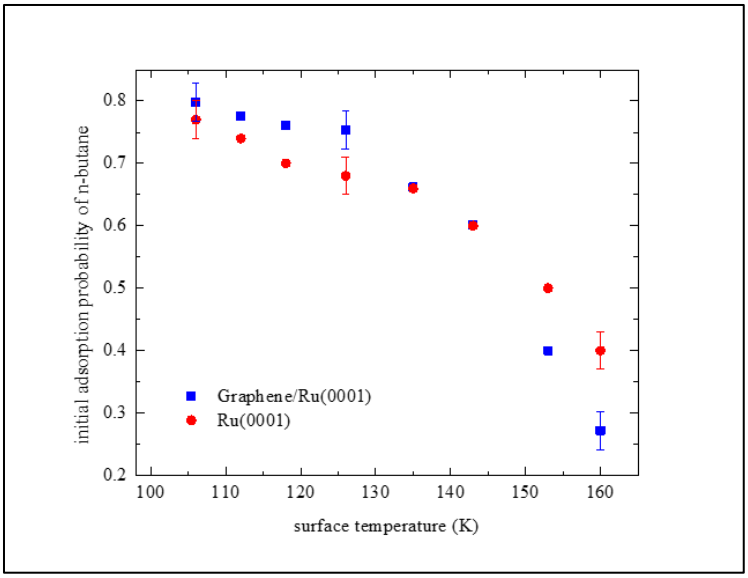

Figure 66. Change in S_0 with increasing temperature for Ru(0001) and graphene/Ru(0001)

The change in S_0 with increasing E_i at constant temperature is shown in figure 67. The S_0 is almost constant at lower E_i (up to 0.8 eV). As the E_i increases further the S_0 decreases, which is characteristic of non-activated adsorption of n-butane on Ru(0001) and graphene/Ru(0001). The increase in E_i, makes the adsorbate more energetic allowing the molecule to dissipate more energy before adsorbing on to the surface. Thus, with increasing E_i, a decrease in S_0 is seen clearly on both surfaces studied. The S_0 is comparable for Ru(0001) and graphene/Ru(0001), which is within the experimental uncertainties; the S_0 measurements with increasing E_i shows that the graphene is dynamically transparent. The S_0 for other carbon allotropes (HOPG and CNTs) show a lower S_0 (0.45 and 0.42); the lower adsorption probabilities of HOPG and CNTs could be due to a morphological difference, where the multi-layered structure of HOPG and curvature of CNTs could reduce the adsorption probabilities of n-butane.[103-104] Thus, although a non-activated adsorption is seen for n-butane on Ru(0001), graphene/Ru(0001), HOPG, and CNTs, the S_0 is significantly different for HOPG and CNTs compared to Ru(0001) and graphene/Ru(0001).

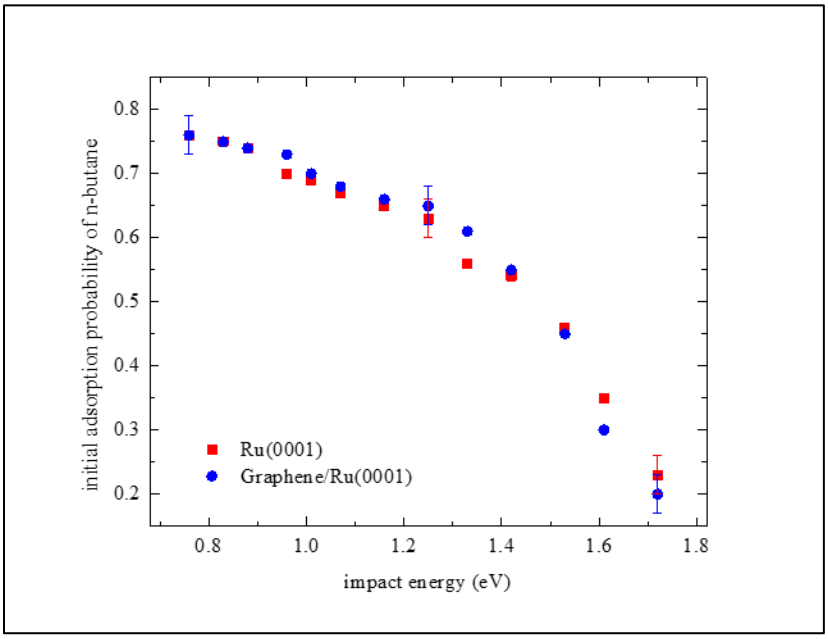

Figure 67. Change in S_0 with increasing impact energy for Ru(0001) and graphene/Ru(0001)

The transient kinetics of n-butane on Ru(0001) and graphene/Ru(0001) shows a Kisluik type transient[43] (figure 68), where the adsorption of n-butane leads to precursor mediated adsorption at lower temperature (106 K) and at lower E_i (0.69 eV). At lower surface temperature and lower E_i the n-butane can get trapped into clean (intrinsic) or occupied (extrinsic) sites and diffuse or hop to a vacant site until all the sites are saturated. The S_0 drops to zero once the surface is saturated. Thus, at lower temperature and E_i the precursor state could be expected to show a long lifetime. The precursor mediated adsorption is seen for, both, Ru(0001) and graphene/Ru(0001).

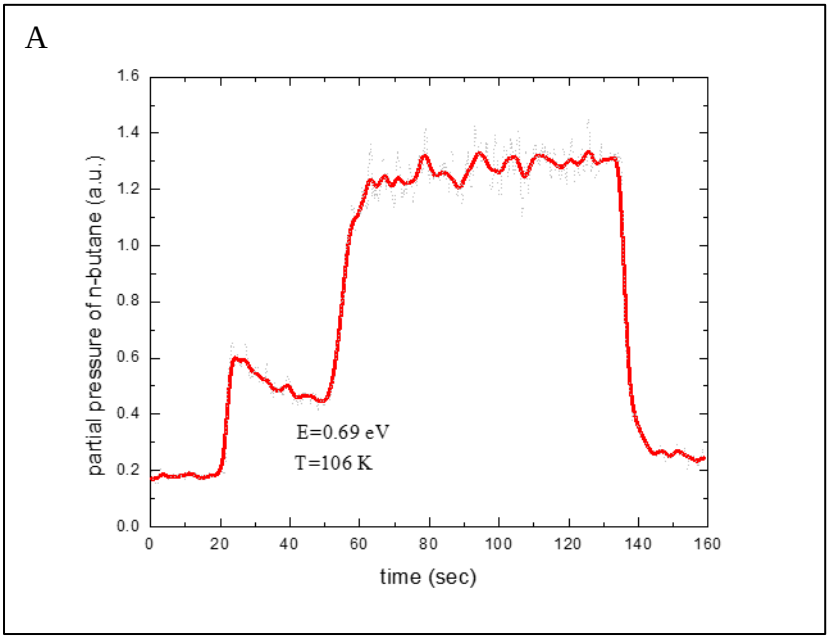

Figure 68. A. Transient kinetics of seeded n-butane on Ru(0001). B. graphene/Ru(0001)

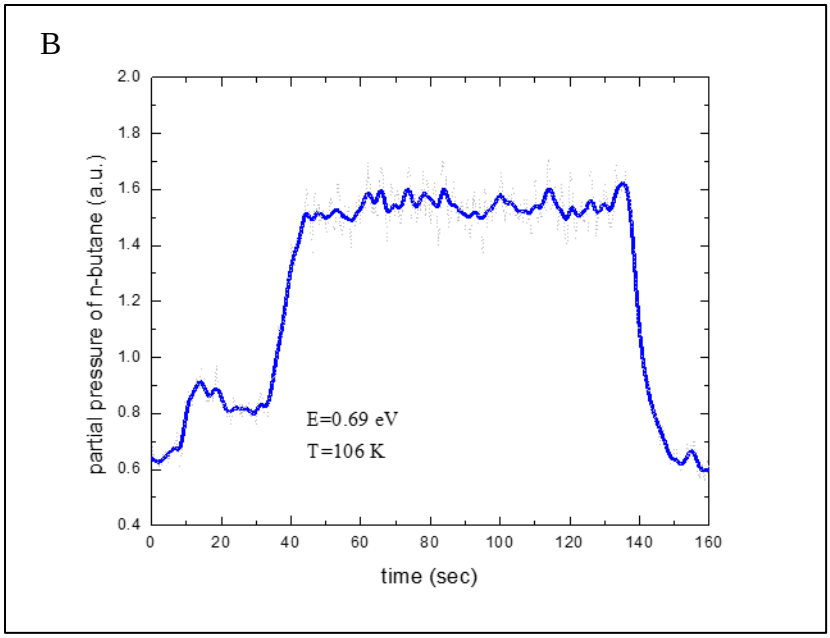

Figure 68. A. Transient kinetics of seeded n-butane on Ru(0001). B. graphene/Ru(0001) (continued)

6.3.2. Effects of support on the adsorption of n-pentane

The effect of support of n-pentane adsorption was studied for three different systems. The supports chosen were highly reactive (Ru(0001), moderately reactive (SiO_2), and an inert support (Cu). The TDS of n-pentane of all three supports are shows separately in figure 69. The desorption temperatures on graphene/Ru(0001), graphene/Cu, and graphene/SiO_2 are ,approximately, 180 K, 158 K, and 145 K. The higher desorption energy at lower coverages show that the binding of adsorbate (n-pentane) is stronger. All the adsorption kinetics of n-pentane on the supported graphene show first-order kinetics for sub-monolayer coverages; the decrease in desorption temperature with increasing coverages are attributable to the repulsive lateral interactions of n-pentane. Coverages above mono layer are seen with a lower multi-layer desorption temperatures at 125 K. The multi-layer coverage follows a zeroth order kinetics with an alignment of leading edges. Thus, the TDS qualitatively shows a difference in desorption for n-pentane adsorption on different supports of graphene.

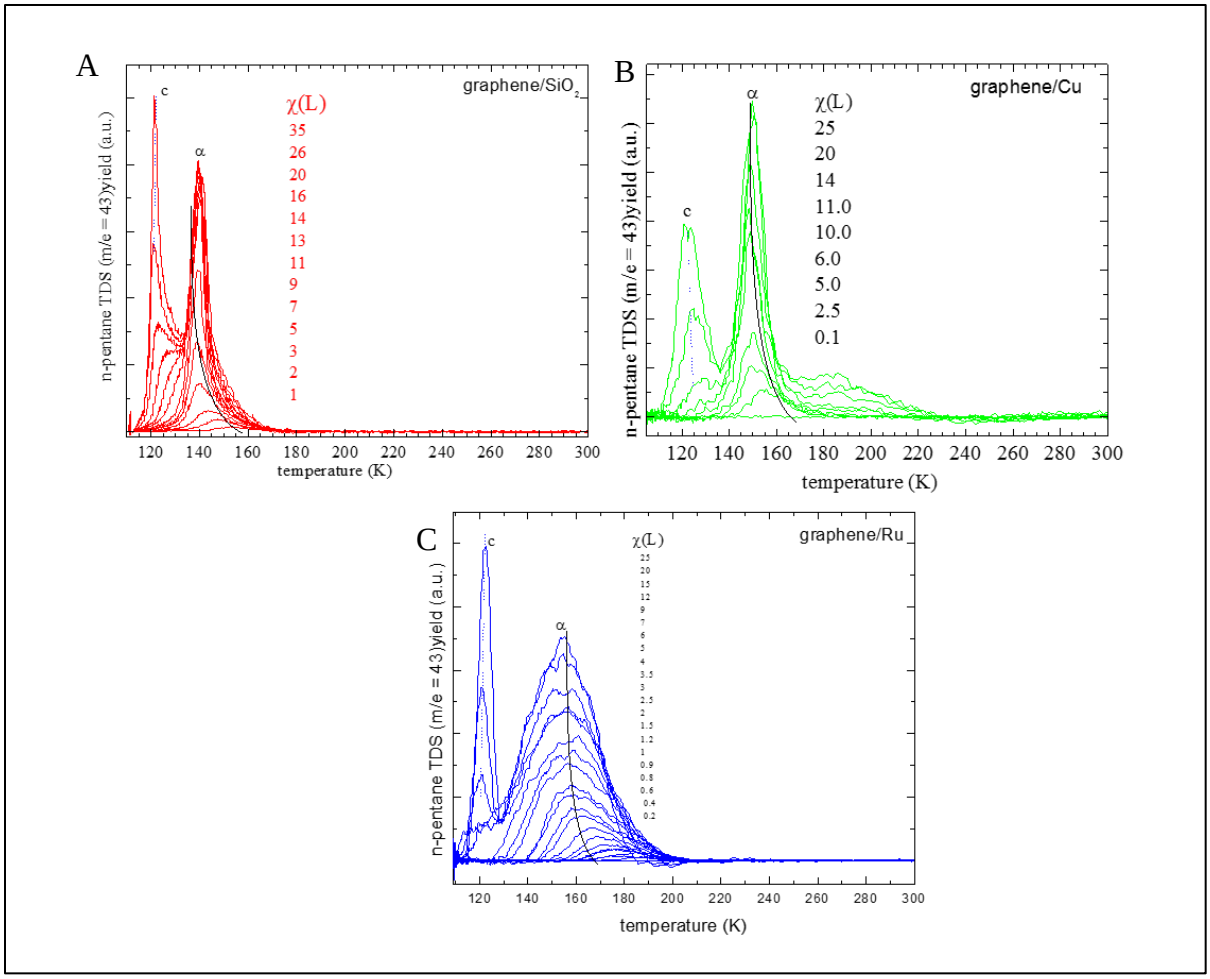

Figure 69. Adsorption of n-pentane on, A. graphene/SiO_2. B. graphene/Cu. C. graphene/Ru(0001)

Translating the TDS curves into coverage dependent binding energy- using Redhead analysis is shown in figure 70. A higher binding energy is seen for the graphene supported on highly reactive support Ru(0001); a significant difference is observed for binding energies in different supports. The DFT calculations have shown that the n-pentane adsorbs on graphene at 3.6 Å and the interaction of n-pentane with graphene is a non-covalent interaction. However, the support can play an important role in binding of n-pentane molecule, which means that support effects can be transmitted through graphene; graphene is a translucent (semi-transparent) material, where it transmit 30% of van der Waals interactions. The reactive support Ru(0001) can polarize

the n-pentane molecule more than the Cu and SiO_2 support. Thus, the polarizability of the support could have contributed towards the reactivity of n-pentane. The study clearly shows that support indeed influence the binding energies of n-pentane.

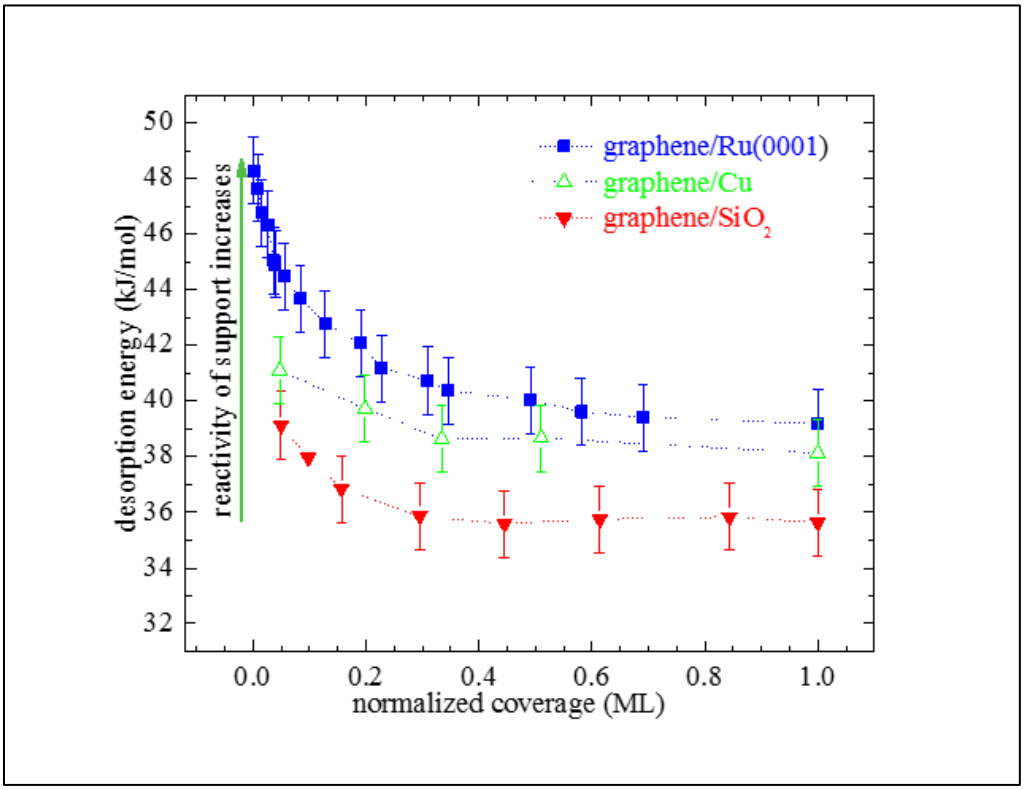

Figure 70. Coverage dependent binding energies of n–pentane on different supported graphene

6.3.3. Chain length dependence of n-alkanes on graphene

The effect of increase in chain length of n-alkanes was studied on a graphene/Ru(0001) surface. The coverage dependent binding energies are shown in figure 71. As the number of carbon increases the binding energy should increase by 6.7 kJ/mol, according to theoretical studies. The methylene ($-CH_2$) groups in the alkane backbone are the physical origin for such increase in the binding energies. As the chain length increases, the polarizability of the n-alkanes will increase due to the increased hybridization of sp^2-sp^3 orbitals of graphene and n-alkanes, respectively. Although a linear increase is seen from n-butane to n-heptane (figure 71b), the difference between

the binding energy is not 6.7 kJ/mol. The discrepancy in the observed values could be related to the consideration of a constant pre-exponential factor (10^{13} s^{-1}) in our analysis. Previous studies[105-106] showed that a complex inverse optimization (inverse of Redhead equation) can be applied to calculate the pre exponential factor for different chain lengths; pre-exponential factor varies with the size of the molecule. Binding energy values with different pre-exponential factors were comparable to theoretical studies. Nevertheless, the present study assumed a constant pre-exponential factor. Although the values were different than the previously reported values, an increase in binding energy was seen with increasing chain length.

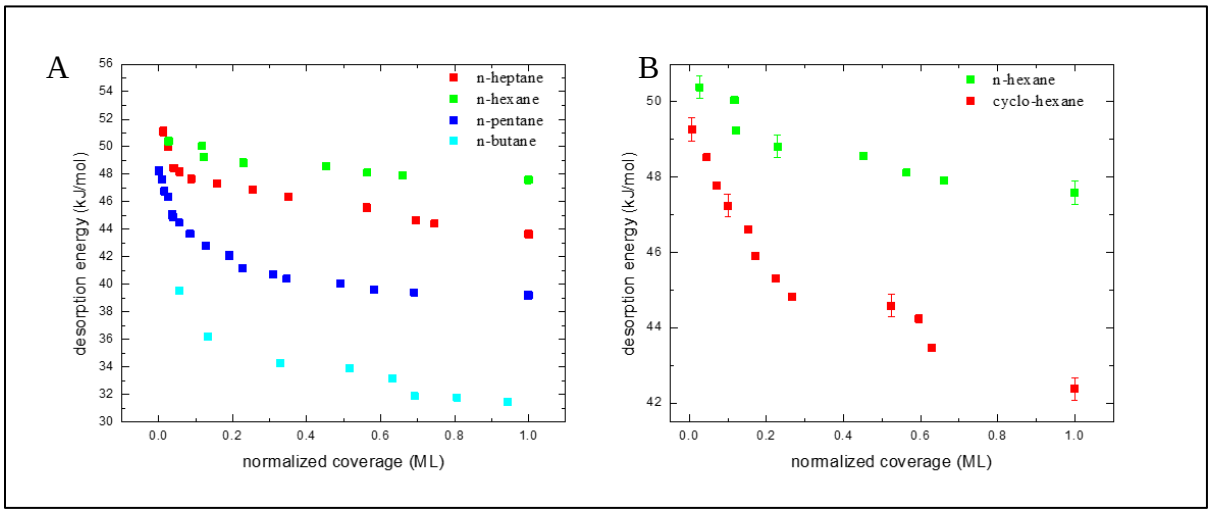

Figure 71. A. Coverage dependent binding energies for different straight chain alkanes. B. Coverage dependent binding energy for linear (n-hexane) and branched alkane (cyclo-hexane)

The end group effects of n-alkane upon adsorption is another aspect of n-alkane adsorption on different surfaces. In order to study the effect of the end group (methyl group, CH_3), a linear and a cyclic alkane with same number of carbons (n-hexane and cyclo-hexane) was compared. The cyclic alkane lacks $–CH_3$ group, thus the difference in the binding energies could be correlated to the contribution of $–CH_3$ groups on binding. As the alkanes bind parallel to the surface, only one $–CH_3$ group interacts with the surface as opposed to many $–CH_2$ groups that interact through the

n-alkane backbone.[107-108] Comparing the binding energies of n-hexane and cyclo-hexane (figure 71B) showed that the n-hexane has a binding energy, which is nearly 1 kJ/mol greater than cyclo-hexane; the CH_3-Π interactions amounts to 2 kJ/mol. The difference in the binding energy can be accounted for the binding of $–CH_3$ group on the surface. Therefore, the end group has an effect, although not significant, on the adsorption kinetics of n-alkanes.

The linear and branched alkanes could be expected to show different binding energies due to their structural differences. Although the orientation of the linear and branched alkanes could be expected to be parallel to the surface, the branched alkanes can be expected to act like spherical molecules. The adsorption probability of n-butane (linear) and iso-butane (branched) on HOPG showed higher S_0 for n-butane (0.59) compared to iso-butane (0.53).[103] Similarly, in the present study, the coverage dependent binding energies of n-butane and iso-butane on graphene/Ru(0001) (figure 72) showed an increase in binding energy for n-butane. The branched molecule, iso-butane, can be assumed to bounce back easily from the surface because of its spherical structure and hence the polarizability of iso-butane could be less than n-butane. However, n-butane can retain its conformation- leading to an increased polarizability and hence high binding energy. Thus, the binding energy could also be influenced by the linear and branched nature of alkanes.

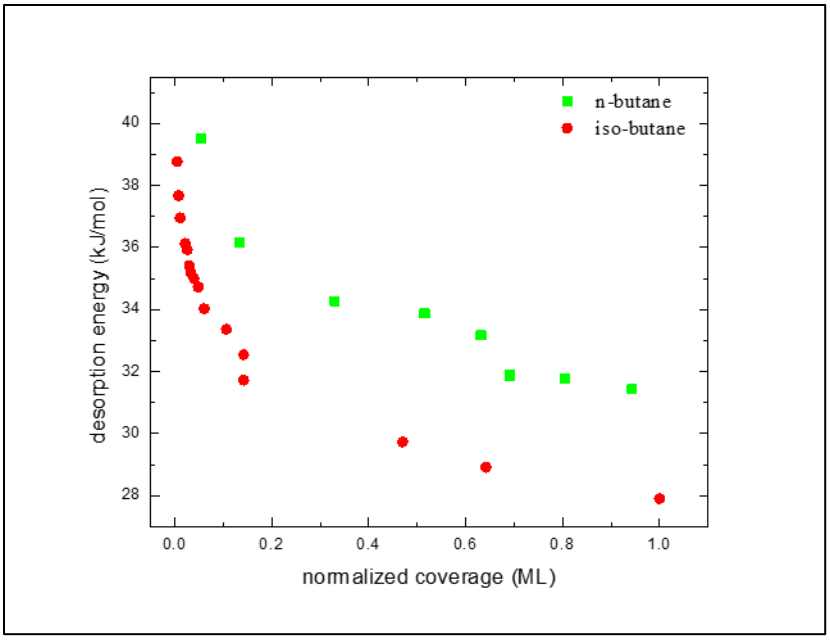

Figure 72. Coverage dependent binding energies of butane and iso-butane on graphene/Ru(0001)

6.4. Summary

Seeded n-butane adsorbed molecularly on, both, Ru(0001) and graphene/Ru(0001). Graphene was kinetically and dynamically transparent to n-butane adsorption. Furthermore, the dynamics studies showed a non-activated adsorption of n-butane on Ru(0001) and graphene/Ru(0001).[108] Besides, comparison of the exterior of CNT to the graphene layer showed a lower binding energy for n-butane adsorption (39.5 kJ/mol for graphene/Ru(0001) vs. 23 kJ/mol for exterior of CNT). The difference could be attributable to the influence of support on Ru(0001).

Adsorption of n-pentane was influenced by the support. Highly reactive support showed a high binding energy (graphene/Ru(0001)= 48 kJ/mol) compared to moderately reactive (graphene/Cu= 41.5 kJ/mol), and an inert support (graphene/SiO_2= 39 kJ/mol).[109] Therefore it could be concluded that support effects are transparent through the graphene layer making graphene a translucent material.

Chain length dependence of n-alkane on graphene/Ru(0001) was observed. Binding energies increased with increasing chain length. In addition, the cyclic and linear alkanes with same number of carbon (n-hexane and cyclo-hexane) showed nearly 1kJ/mol higher binding energy for n-hexane compared to cyclo-hexane. The difference of 1 kJ/mol is attributable to the contribution of the end group. Besides, the straight chain alkane (n-butane) showed higher binding energy than cyclic-alkane (iso-butane) because of the linear conformation of the n-butane; linear molecule can retain its configuration on the surface making is more polarizable and in turn having a high binding energy. In contrast, spherical molecule (iso-butane) can bounce back from the surface easily resulting in a lower binding energy.

CHAPTER 7. ADSORPTION KINETICS AND DYNAMICS OF CO_2 ON GRAPHENE OXIDE/Ru (0001)

7.1. Introduction

Carbon dioxide is a molecule of interest in, both, chemical industries and environmental pollutions. The chemical industry, especially the methane production, on one hand, requires carbon dioxide as a major reactant. However, on the other hand elevated levels of carbon dioxide, in the atmosphere, through various anthropogenic sources have become a recent concern for global warming and hence climatic changes.[111-114] Carbon dioxide capture methods are used in order to reduce the levels of carbon dioxide in the atmosphere. One such carbon dioxide capture methods is to use the process of adsorption; metals and metal free adsorbents can be used to capture carbon dioxide. Metal free adsorbents, which are carbon based materials, are one of the promising materials for carbon dioxide capture. The carbon based materials are inexhaustible and hence exploiting such materials for carbon dioxide capture could be an area of interest for, both, academia and industry. Therefore, this chapter describes the adsorption of carbon dioxide on an oxygen functionalized graphene (graphene oxide) supported on Ru(0001).

The adsorption kinetics and dynamics of carbon dioxide on Ru(0001), graphene/Ru(0001), and graphene oxide/Ru(0001) is discussed in this chapter. The synthesis and characterization of the surfaces used in this study is described in chapter 3. The adsorption kinetics was studied using TDS, where the bind energies of carbon dioxide was quantified. The carbon dioxide did not bind to graphene/Ru(0001); the binding energies were enhanced on graphene oxide/Ru(0001) compared to Ru(0001). In addition, the adsorption dynamics was studied by molecular beam scattering techniques. The adsorption probabilities were almost zero for graphene and an enhanced adsorption probability was seen for graphene oxide/Ru(0001). The adsorption dynamics also

clearly showed that the carbon dioxide was only weakly physisorbed on Ru(0001) and graphene oxide/Ru(0001) and no dissociation was seen on both the surfaces. The results are promising for the utilization of graphene oxide in carbon dioxide capture.

7.2. Literature review

Biosystems, especially plants capture carbon dioxide through the metal centers for photosynthesis. The ribulose 1,5- bisphosphate carboxylase/oxidase (Rubisco) has a Mg^{2+} metal center, which can activate the carbon dioxide and aid in the formation of carboxylate ions to facilitate photosynthetic process.[115] A similar concept was extended for the chemical industries where the carbon dioxide was used as a major reactant-through a heterogeneous catalytic reactions synthesize methane, urea, and methanol, to name a few. The methanation reaction involves the use of syngas (CO_2+CO+H_2) over copper metal to produce methane, which is also called as Sabatier reaction.[111] In addition, the carbon dioxide is reacted with ammonia to form urea, which also uses the metals as a catalyst. A combination of carbon dioxide and hydrogen in the presence of transition metals can result in methanol synthesis. All the aforementioned reactions involve a metal center for the activation of carbon dioxide, which can then be facilitated to produce various products. The common fates of carbon dioxide on metal surfaces can be classified as: physisorption, chemisorption, dissociation, and carbonates and oxalate formation.[116] In transition metals, mostly carbon dioxide dissociate into either C+O_2 (on Fe) or CO+O (on Ni); the dissociation of carbon dioxide depends on the surface roughness and defects. Ni and Fe are the most active metals for carbon dioxide dissociation and Ru is inert for carbon dioxide and hence a weak physisorption is seen for carbon dioxide adsorption on Ru.[117] However, incorporation of alkali metals on Ru activates carbon dioxide and forms carbonates or oxalates.[118] Overall, the carbon dioxide adsorption on metal surfaces are determined by the surface properties (roughness,

defects, incorporation of alkali metals) of the metal surfaces, which has substantial applications in chemical industry.

The chemical industries utilize carbon dioxide as an efficient reactant where as many other processes have led to the elevated levels of greenhouse gases. Human expansion of carbon dioxide gas in the atmosphere through multiple anthropogenic activities: fossil fuel burning and coal combustion, industrial by-products, and landfills have led to global warming. Although there is an expansion of other greenhouses gases, the carbon dioxide is cited as the most potent gas for global warming and subsequent climatic changes. Thus carbon dioxide capture technologies have become popular in recent years due to the exponential release of carbon dioxide into the atmosphere. One of the most commonly and long used carbon dioxide capture technologies is to utilize a process known as "wet scrubbing".[116] The primary, secondary, and tertiary amine solvents are reacted, at high temperatures (100-150 ˚C), with carbon dioxide to form carbomates and hydrogen carbamates, through zwitter ionic reaction (figure 73). The process of using amine solvents are of environmental concern and also the process itself is energy incentive due to high temperature application. An alternative methods for amine solvents is to use ionic liquids for the capture of carbon dioxide. The ionic liquids can bind to carbon dioxide through van der Waals interactions leading to weak physisorption. In addition to the liquids in carbon dioxide capture, physical adsorbents (zeolites, metal-organic frame works (MOFs), and carbonaceous materials) are used as adsorbents for carbon dioxide.[116] Use of such materials for the capture of elevated levels of carbon dioxide can mitigate the environmental concerns of global warming.

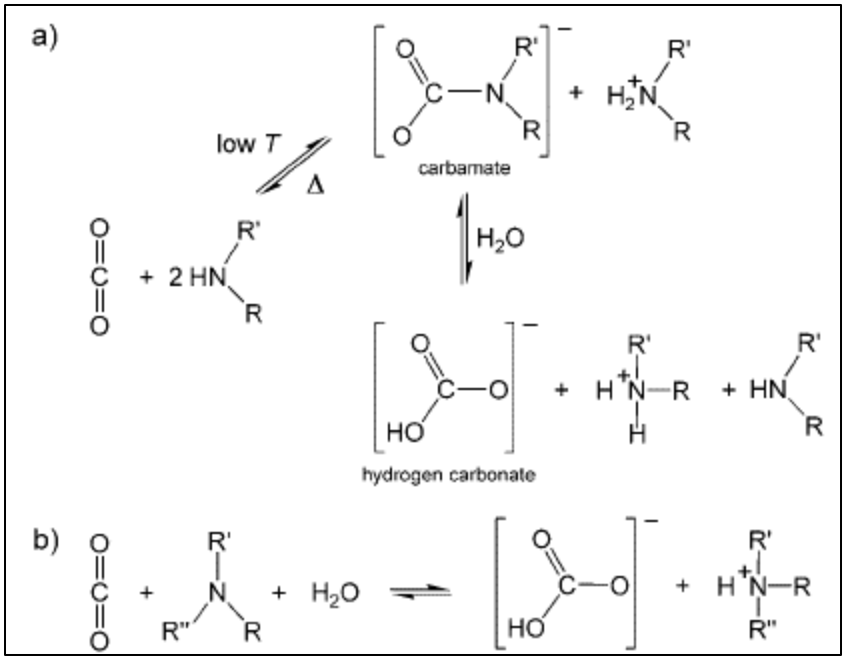

Figure 73. Wet scrubbing of carbon dioxide through zwitter ionic reaction[116]

Carbon based materials are potent sources for the carbon dioxide capture technologies due to the inexhaustible and sustainable nature. The carbon allotropes: fullerenes, CNTs, HOPG, and graphene are widely used as gaseous adsorbents. Graphene is one of the recently used popular material for gaseous adsorption to fabricate gas sensors.[119] However, the carbon dioxide adsorption on graphene surface occurs through very weak physisorption, where the DFT shows the binding energies are less than 15 kJ/mol.[120] Thus, functionalizing graphene with reactive species can enhance the adsorption of carbon dioxide. Graphene oxide is a possible material, which could bind to carbon dioxide stronger than graphene. The oxidation of graphene leads to a change in the hybridization of graphene carbon, while introducing a high density of oxygen on the surface. During oxidation, the sp^2 hybridized carbon on graphene changes to sp^3 hybridized carbon in order to accommodate the oxygen.[121-124] DFT studies have shown, that during the oxidation of graphene, to form graphene oxide, the oxygen groups can get attached to both basal planes and the edges of graphene; the oxidation of graphene can form various oxygen containing functional groups:

epoxide, hydroxyl, and carboxyl. Unlike graphene, graphene oxide is a reactive material; both the aromaticity and the reactive oxygen containing functional groups in graphene oxide can synergically act towards making graphene oxide a reactive material.[120,121-124] Thus, the graphene oxide can be used for carbon dioxide capture technologies.

7.3. Results and discussion

7.3.1. Adsorption kinetics of carbon dioxide

The adsorption kinetics of carbon dioxide was studied on Ru(0001), graphene/(Ru(0001), and graphene oxide/Ru(0001). The carbon dioxide was adsorbed at 85 K, on a cryogenically cooled sample. As shown in Figure 74B, the carbon dioxide did not adsorb on a graphene surface, which is consistent with the DFT calculations; the theoretical studies showed that the carbon dioxide adsorb parallel on a graphene surface to maximize the van der Waals interaction, however, the calculated binding energies were less than 15 kJ/mol. On a Ru(0001) surface (figure 74A), graphene adsorbs at 85 K and starts to desorb at 115 K for lower coverages. As the coverage of the carbon dioxide increases, the desorption shifts towards lower temperatures, up to 90 K, and starts to condense. The shifting of desorption peaks towards lower temperatures is attributable to the repulsive lateral interaction of the carbon dioxide molecules. The condensation occurs at 90 K, above 40 seconds, where the leading edges align and the condensation temperatures shifts towards high temperature because more time is needed to desorb the condensed carbon dioxide layer. A similar behavior is seen for graphene oxide/Ru(0001), where the desorption temperatures decrease with coverage and above 40 seconds the carbon dioxide starts to condense. However, in contrast to the adsorption of carbon dioxide on Ru(0001), the desorption peaks are 5 K higher for graphene oxide/Ru(0001) at lower coverages (120 K). The higher desorption temperatures could be due to the enhanced interaction of carbon dioxide on oxygen functionalities of graphene oxide (O----

O=C=O); the polarizability of the support also could contribute towards the higher desorption temperatures in graphene oxide. Thus, the adsorption kinetics show that the carbon dioxide can bind to both Ru(0001) and graphene oxide/Ru(0001) and does not bind or binds with lower binding energies on a graphene surface.

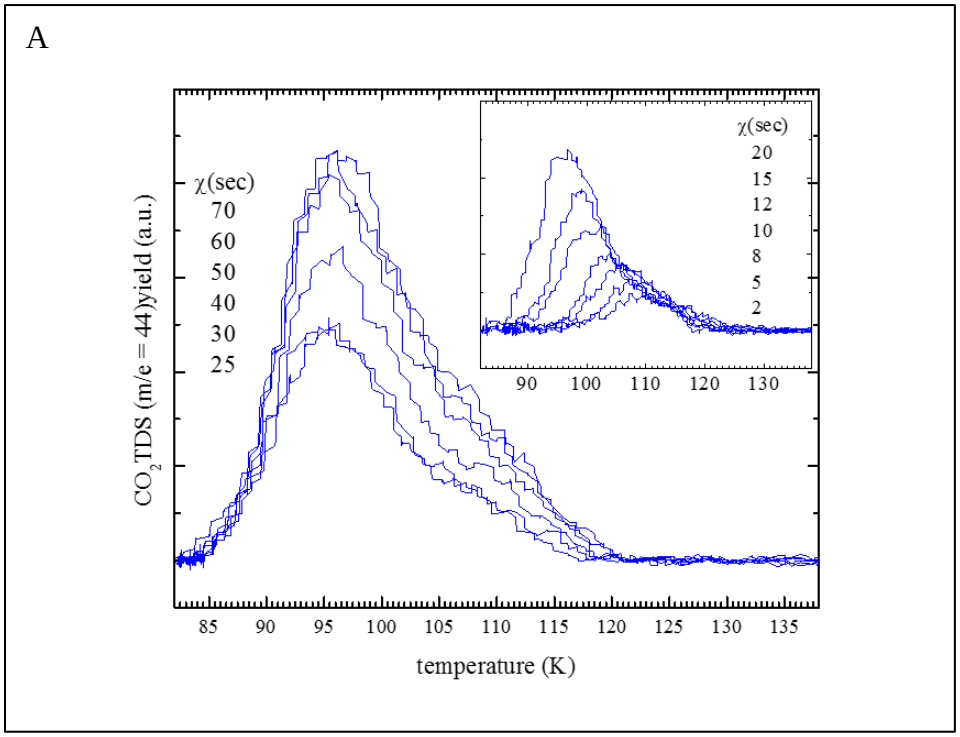

Figure 74. A. Adsorption of carbon dioxide on Ru(0001) B. Graphene/Ru(0001), C. Graphene oxide/Ru(0001)

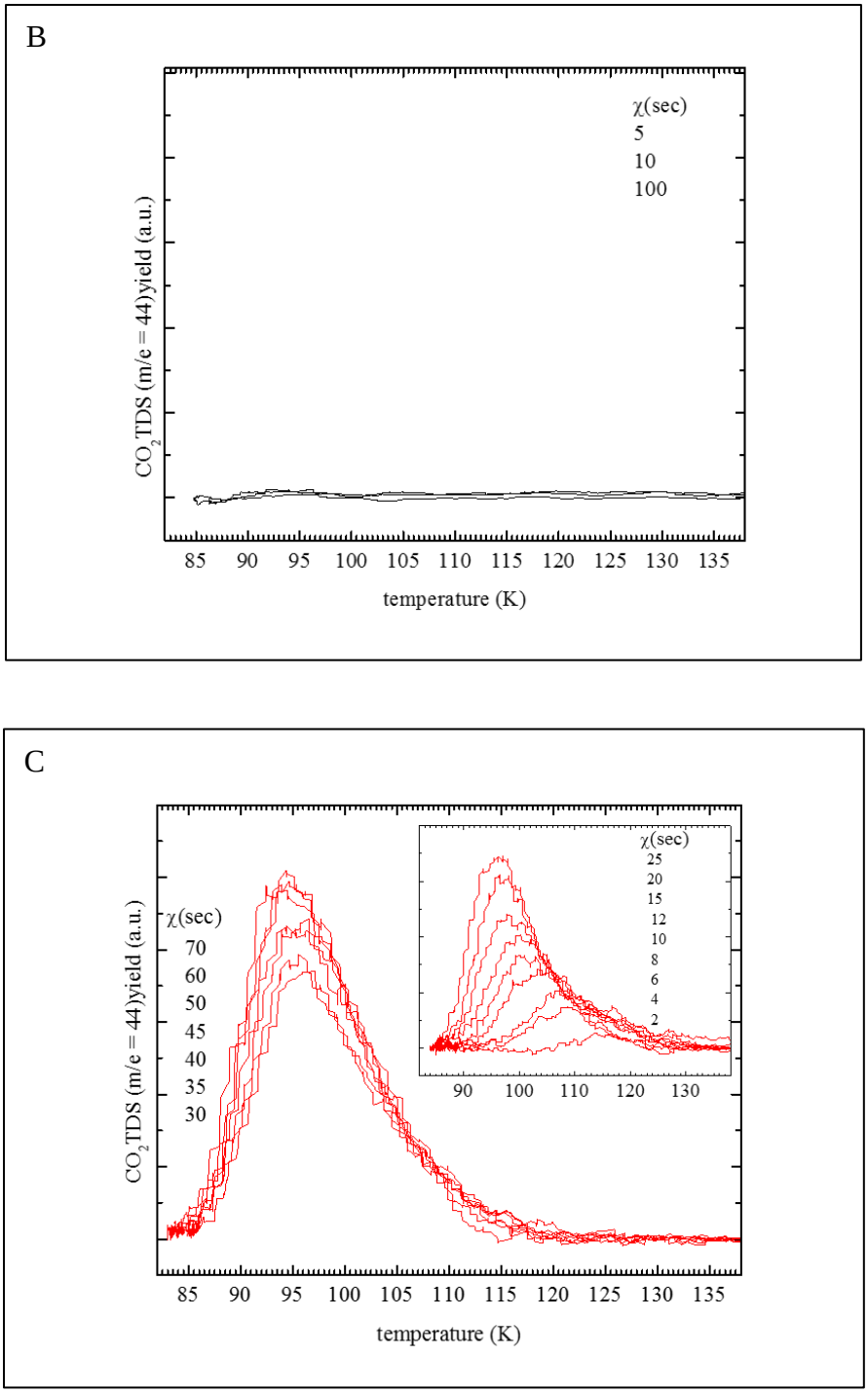

Figure 74. A. Adsorption of carbon dioxide on Ru(0001) B. Graphene/Ru(0001), C. Graphene oxide/Ru(0001) (continued)

A multi-mass TDS was recorded, on carbon dioxide adsorption on Ru(0001), graphene/Ru(0001), and graphene oxide/Ru(0001), for additional masses such as CO (m/e= 28) and CO_3^{2-} (m/e= 50). There were no peaks other than carbon dioxide (m/e=44) was seen, which indicates that the carbon dioxide did not dissociate on the surfaces studied. Besides, the intercalation of oxygen on the graphene/Ru(0001) and graphene oxide/Ru(0001) could be ruled out because the intercalated oxygen can bind to Ru(0001) surface to form RuO_2; carbon dioxide distinctly binds to RuO_2, where four different desorption peaks are evident at 93 K, 175 K, 188 K, and 315 K.[125-126] The first order kinetics was observed for carbon dioxide adsorption on Ru(0001) and graphene, which is depicted in figure 74(A and C). There was no distinct monolayer and multilayer peaks were observed, which is seen in most cases, due the similar interaction between carbon dioxide-surface and carbon dioxide-carbon dioxide. Translating the TDS curves into coverage dependent binding energies- using Redhead analysis is shown in figure 75. The binding energies of carbon dioxide on Ru(0001) and graphene oxide/Ru(0001) were different only by a few percentage; the graphene oxide/Ru(0001) had a higher binding energy (26.9 kJ/mol) compared to Ru(0001) (26.5 kJ/mol). The decrease in the binding energy with increasing coverage is due to the lateral interactions of carbon dioxide molecules, which is also observed in the TDS. Overall, the adsorption kinetics show that the carbon dioxide binds on Ru(0001) and graphene oxide/Ru(0001) and the binding energies are enhanced in graphene oxide/Ru(0001).

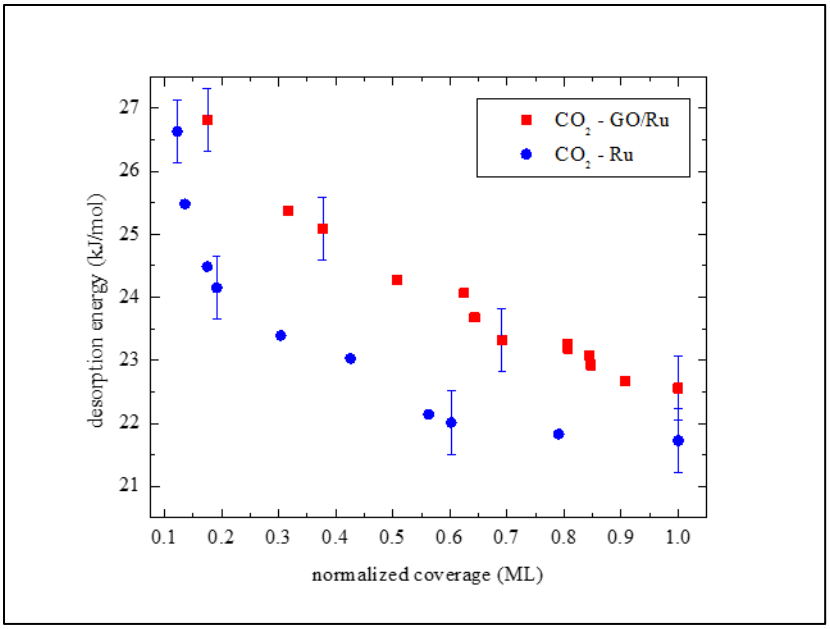

Figure 75. Coverage dependent binding energies of Ru(0001) and graphene oxide/Ru(0001)

7.3.2. Adsorption dynamics of carbon dioxide

The adsorption dynamics was studied on Ru(0001), graphene/Ru(0001), and graphene oxide/Ru(0001) using a seeded carbon dioxide beam (CO_2/He). The adsorption probability for carbon dioxide on graphene/Ru(0001) was zero (Figure 76), which was also seen in the TDS, where the carbon dioxide did not adsorb on graphene/Ru(0001). Since the adsorption dynamics for Ru(0001) and graphene oxide/Ru(0001) shows a similar trend, the adsorption dynamics for graphene/Ru(0001) and graphene oxide/Ru(0001) is depicted in figure 77. The adsorption transients are plotted as 1-initial adsorption probability ($1-S_0$) vs the time, since the S_0 was around 0.25. As the carbon dioxide does not adsorb on a graphene surface, a step-like increase is seen as soon as the beam flag is opened; the surface immediately reaches a saturation due to the background gas load on the chamber, which increases because the carbon dioxide does not adsorb on the graphene surface. In contrast, the graphene oxide/Ru(0001) shows a step-like increase as soon as the beam flag opens. As the carbon dioxide adsorbs on the surface, the background carbon dioxide pressure decreases showing a dip on the adsorption transient until 40 seconds. Once the

surface saturates at 40 seconds, which is evidenced from both the TDS and the adsorption probability curves (not shown), the adsorption kinetics also reaches a maximum. The adsorption transients clearly show that the adsorption probabilities are high for graphene oxide/Ru(0001) compared to graphene/Ru(0001).

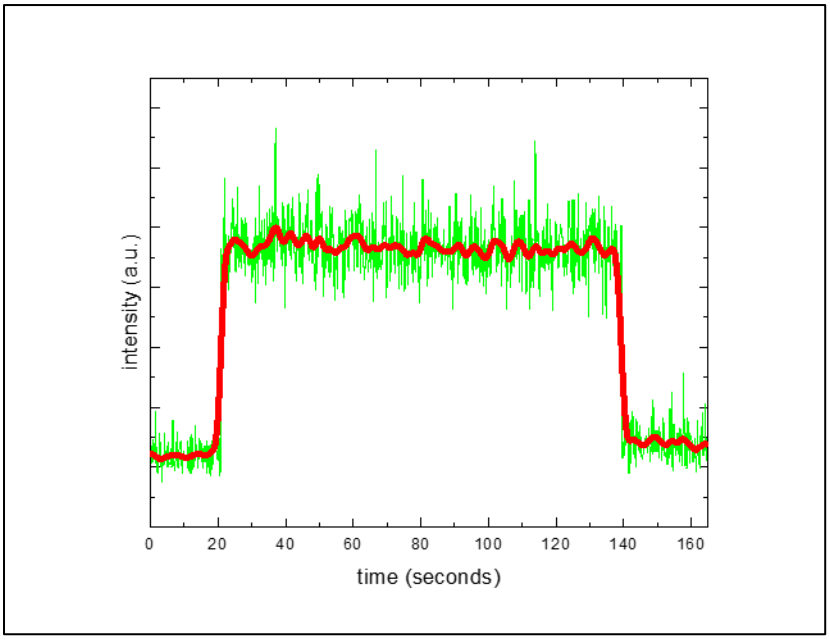

Figure 76. Adsorption probability for graphene

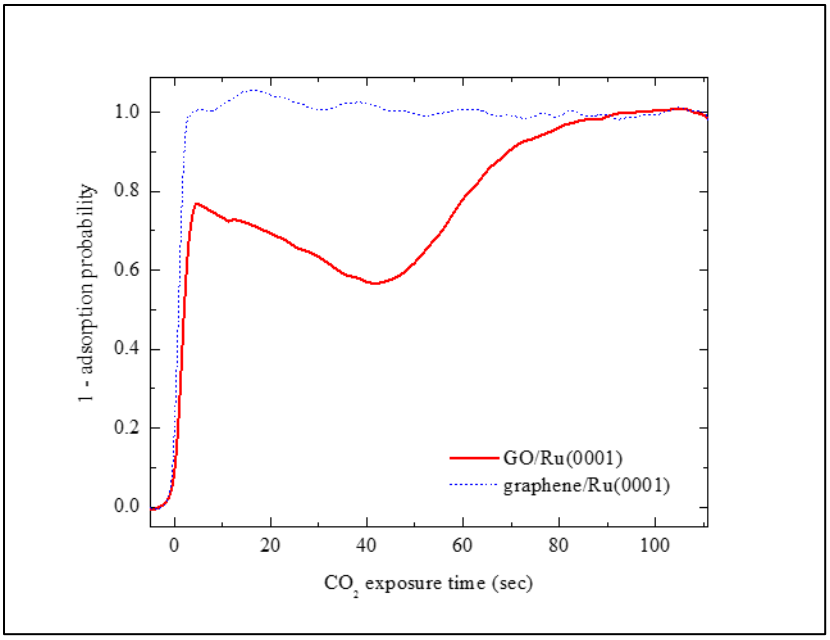

Figure 77. Transient kinetics of graphene oxide and graphene

Integrating the transient kinetics for graphene oxide/Ru(0001) results as shown in figure 78. The curve shape can be easily explained when the transient kinetics is integrated. The adsorption probabilities are plotted vs the coverage. At lower or zero coverage the adsorption probability is maximum and as the coverage increases the adsorption probability increases until it reaches a saturation. This is attributable to an adsorbate-assisted adsorption, also similar to an autocatalytic process, where the incoming molecule occupies a pre-occupied site and then moves towards or hops to a vacant site. Adsorption on an incoming molecule on a pre-occupied site is more favored than direct adsorption due to the mass match between the pre-occupied state and the incoming molecule; the energy can be easily dissipated when there is a mass match favoring the adsorption.[112-114] Adsorbate-assisted adsorption also facilitates the prolonged lifetime of the incoming molecule, until it hops into a vacant site. As soon as the surface is saturated, the adsorption probabilities drop to zero; around 1 ML coverage the adsorption probability drops

rapidly to zero. Thus, the integrated transient kinetics shows an adsorbate-assisted adsorption for carbon dioxide adsorption on a graphene oxide/Ru(0001).

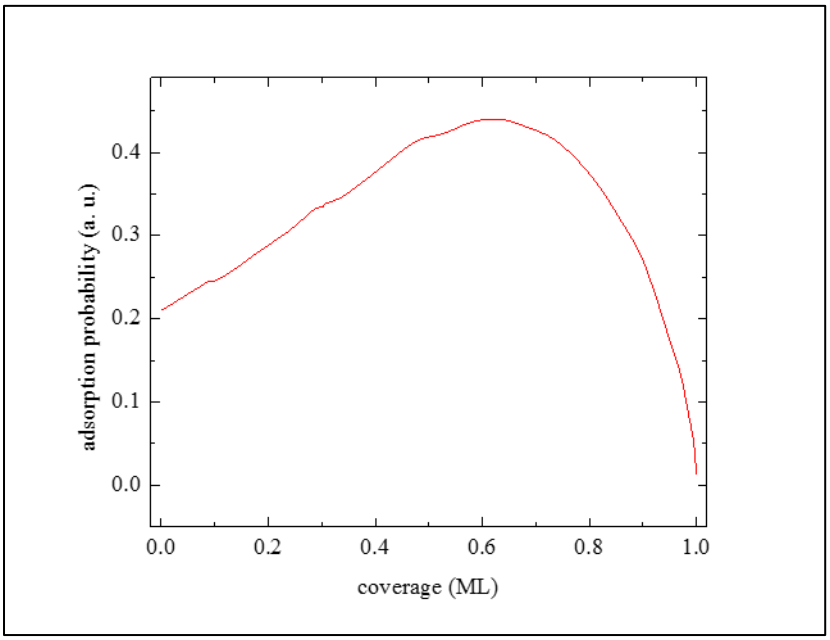

Figure 78. Integrated transient kinetics

The interaction of carbon dioxide on Ru(0001) and graphene oxide/Ru(0001) was studied by increasing the impact energy of the seeded carbon dioxide. The adsorption kinetics already showed (Figure 79) that the carbon dioxide adsorbs weakly through a van der Waals interactions. However, the adsorption dynamics were studied in addition to prove the fact that carbon dioxide adsorbed molecularly on, both, Ru(0001) and graphene oxide/Ru(0001). The maximum adsorption probabilities were plotted against the impact energy (Figure 79), at a surface temperature of 85 K. The adsorption probabilities decreased with increasing impact energies. This is in agreement with a non-dissociative adsorption of carbon dioxide on both Ru(0001) an graphene/Ru(0001). As the energy of the adsorbates increases, more energy has to be dissipated before they adsorb onto the surface and in turn the higher impact energy reduces the interaction of the adsorbate on the surface. The adsorption probabilities are higher for graphene oxide/Ru(0001) compared to Ru(0001) due

to the enhanced interaction of the oxygen functionalities on graphene oxide with carbon dioxide. In addition, the temperature dependent adsorption probabilities were also studied (figure 80) at constant impact energy (0.69 eV). A similar behavior was seen for the adsorption probabilities with increasing surface temperature, where the adsorption probabilities decreased with increasing surface temperature due to the non-dissociative and molecular adsorption of carbon dioxide. The adsorption probabilities with increased impact energy and surface temperature shows that the carbon dioxide binds molecularly on Ru(0001) and graphene oxide/Ru(0001) and the adsorption probabilities are enhanced for graphene oxide/Ru(0001)

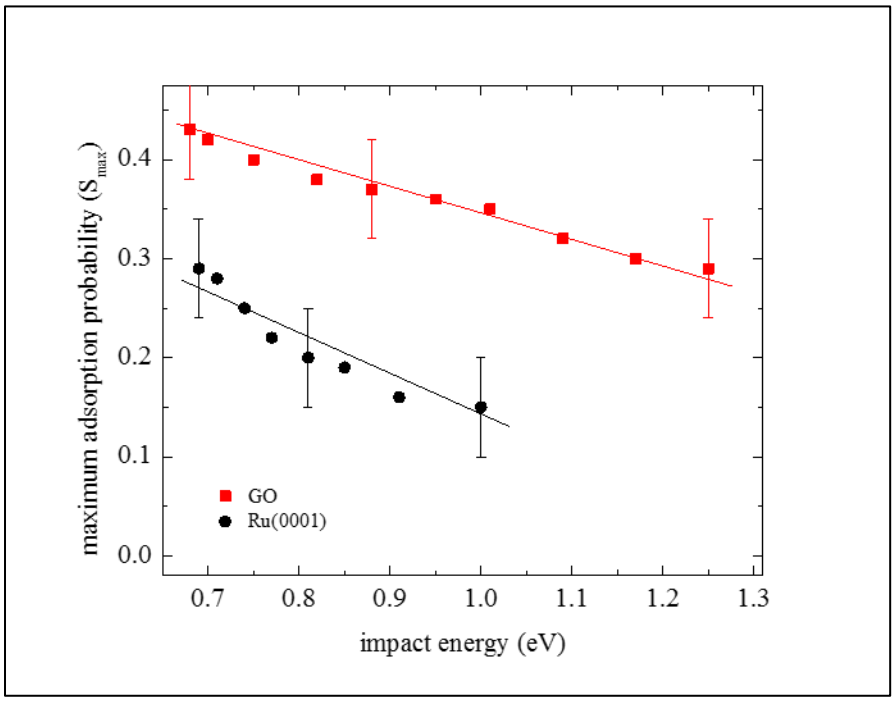

Figure 79. Change in adsorption probabilities with impact energy

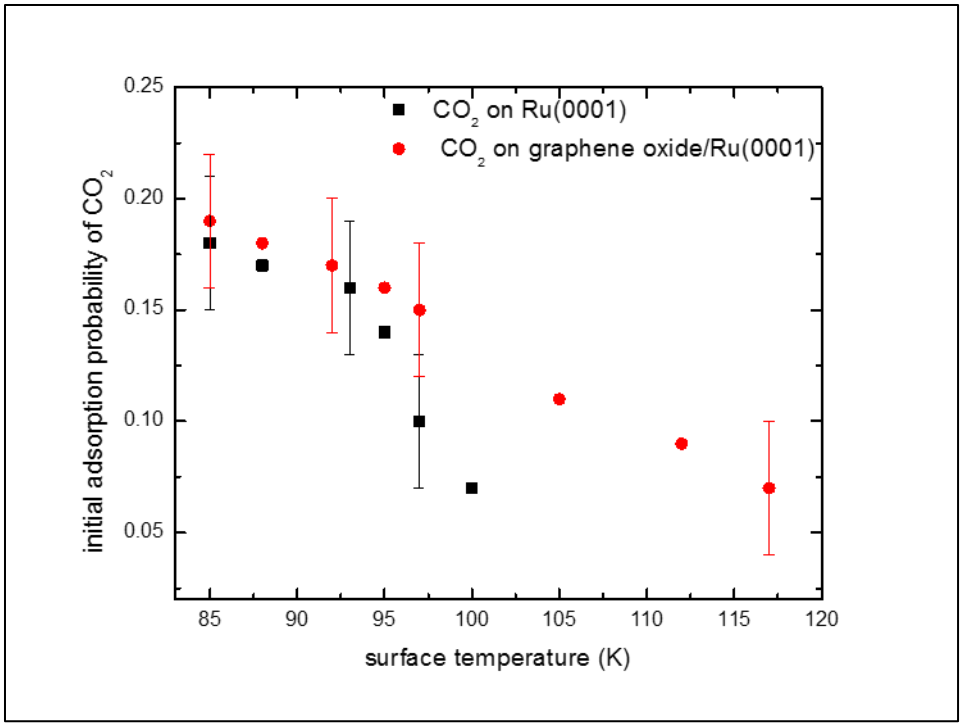

Figure 80. Change in adsorption probabilities with temperatures

7.4. Summary

The adsorption kinetic and dynamics showed that the carbon dioxide does not adsorb on graphene. On Ru(0001) and graphene oxide/Ru(0001) carbo dioxide adsorbs and an enhanced adsorption is seen for graphene oxide/Ru(0001); a synergetic effect of oxygen functionality and the polarizability of the substrate (Ru(0001)), could be the driving force for the enhanced adsorption. Although it was expected to see a catalytic behavior of carbon dioxide on a graphene oxide surface, which could be used as a metal-free catalyst, this study showed that the carbon dioxide can only molecularly adsorb and there was no dissociation seen on the surface. The overall results suggest that graphene oxide could be used as a promising material for carbon dioxide adsorption, which could be used in fabricating carbon dioxide sensors to reduce the elevated levels of carbon dioxide in the atmosphere.[127]

CHAPTER 8. SUMMARY AND CONCLUSIONS

The adsorption kinetics and dynamics of small molecules (water, benzene, n-alkanes, and carbon dioxide) were studied on graphene. The transparency of graphene, influence of support (support effects), and functionalization of graphene (graphene oxide) were addressed in this dissertation. All these studies were carried out under ultrahigh vacuum conditions to study the intrinsic interactions of the molecules. Surface analytical techniques were used for surface characterization (AES, LEED, and XPS) and adsorption kinetics and dynamics were studied using TDS and molecular beam scattering techniques, respectively.

The wetting transparency of graphene for water adsorption is a highly debatable topic and literature findings were contradictory. The contradictions were addressed in this dissertation by studying the wetting transparency of graphene under ultrahigh vacuum conditions. Our studies showed that graphene was non-transparent because the adsorption kinetics of water on supports (Ru(00001), Cu, and SiO2) and supported graphene (graphene/Ru(0001), graphene/Cu, graphene/SiO2) did not mimic each other. In addition, the adsorption kinetics were influenced by the support; hydrophobic support (SiO2) showed a hydrophilic water interaction on graphene (graphene/SiO2) and hydrophilic support (Ru(0001) and Cu) showed hydrophobic water interaction on graphene (graphene/Ru(0001) and graphene/Cu). Although the adsorption kinetics of water on the supports and on the supported graphene showed a non-transparent behavior of graphene, the support effects were transmitted through graphene . The transmitting the support effects through graphene layer makes graphene a semi-transparent (translucent) material for water adsorption. Thus the adsorption kinetics of water showed a reciprocal behavior for support and supported graphene and the translucency of graphene was evidenced. The findings will have

implications on coating, where graphene can be used as a protective coating depending on the supports on which the graphene will be placed.

The adsorption kinetics of benzene on supports and supported graphene was studied to address the transparency and the support effects. Benzene can be considered as a prototype or building blocks of carbon allotropes and hence the interaction of benzene on carbon allotrope is chemically intriguing. Besides, biomolecules (nucleic acids and amino acids) have benzene as part of the chemical structure; designing graphene-based sensors for biomolecules require the understanding of benzene interactions on graphene. In light of such facts, benzene interactions were studied on graphene. Adsorption kinetics showed that the graphene was transparent to benzene adsorption on graphene/Cu and graphene SiO_2 because the binding energies on supports (Cu and SiO_2) and the supported graphene (graphene/Cu and graphene SiO_2) were within the experimental uncertainties. It appeared at a glance that the transparency of graphene depends on the polarizability of the molecule because graphene was non-transparent to polar molecule (water) and transparent to non-polar molecule (benzene). However, benzene dissociates on a highly reactive support (Ru(0001)) and molecularly adsorbs on graphene/Ru(0001); graphene is non-transparent for Ru(0001) supported graphene. Furthermore, the coverage dependent binding energy was high for graphene/Ru(0001) compared to graphene/Cu and graphene/SiO2. The increased reactivity of benzene on a reactive support, like Ru(0001), could be attributable to the electropositive nature of Ru(0001) to withdraw the electron cloud on graphene and in turn reduce the Π-Π repulsion — resulting in a high binding energy for benzene on graphene/Ru(0001). Therefore, it could be concluded that the transparency of graphene not only depends on the polarizability of the molecule but also depends on the nature of the support.

Alkanes are a class of organic molecules occurring as backbones in biomolecules, monomers in polymers, and coatings on magnetic disks. Mapping the interactions of alkanes on graphene can be used in aforementioned applications. This dissertation addressed various aspects of alkane interactions. Firstly, the adsorption kinetics and dynamics showed that the n-butane was, both, kinetically and dynamically transparent. In addition, n-butane molecularly adsorbed on Ru(0001) and graphene/Ru(0001) and the adsorption was non-activated. Secondly, the support effects were studied for n-pentane on graphene/Ru(0001), graphene/Cu, and graphene SiO_2. The support influenced the n-pentane adsorption on graphene; the coverage dependent binding energy for n-pentane increased as: graphene SiO_2<graphene/Cu graphene/Ru(0001). Finally, the effect of chain length of n-alkanes (n-butane, n-pentane, n-hexane, and n-heptane) were studied on graphene/Ru(0001). The binding energy increased with increasing chain length due to the increased polarizability of the n-alkanes. Furthermore, the contribution of end group on alkane adsorption was studied by comparing the binding energy of linear alkane (n-hexane) with a cyclic-alkane (cyclo-hexane). The binding energy of n-hexane was nearly 1 kJ/mol higher than the binding energy of cyclo-hexane and the difference in binding energy could be attributable to the contribution of end methyl group on n-hexane. Moreover, the binding energy of n-butane was higher than iso-butane because the iso-butane can be considered as a spherical molecule, due to the branching, and hence iso-butane can bounce back easily from the surface compared to n-butane. Overall, the chain length dependence, contribution of the end methyl group, and the structural difference of alkanes were studied on supported graphene.

Graphene is a chemically inert material but due to the sp^2 hybridized carbon, graphene can be readily functionalized. Graphene oxide can be synthesized by oxidizing the graphene material. In this dissertation, graphene on Ru(0001) support was oxidized to form graphene oxide to utilize

in carbon dioxide adsorption. We hypothesized that the graphene oxide can act as a carbocatalyst to catalyze the carbon dioxide. The adsorption kinetics and dynamics of carbon dioxide was studied on Ru(0001), graphene/Ru(0001), and graphene oxide/Ru(0001). Graphene/Ru(0001) did not adsorb carbon dioxide. In contrast, both, Ru(0001) and graphene oxide/Ru(0001) adsorbed carbon dioxide and the adsorption was enhanced on graphene oxide/Ru(0001). Unfortunately, graphene oxide/Ru(0001) did not catalyze the adsorption of carbon dioxide and the molecular adsorption of carbon dioxide on Ru(0001) and graphene oxide/Ru(0001) were confirmed by AES and adsorption dynamics. However, enhanced adsorption of graphene oxide/Ru(0001) shows that graphene oxide could be used as a potential material to adsorb the elevated levels of carbon dioxide.

REFERENCES

1. Kumar, A.; Lee, C. H. In *Synthesis and biomedical applications of graphene: present and future trends*, InTech: 2013; pp 55-75.
2. Dąbrowski, A.; Adsorption — from theory to practice. *Advances in Colloid and Interface Science* **2001,** *93* (1), 135-224.
3. Vera, B.; Fundamentals in Adsorption at the Solid-Gas Interface. Concepts and Thermodynamics. *Calorimetry and Thermal Methods in Catalysis* **2013,** 561, 312.
4. Gabor A. Somorjai1 and Yimin Li.; Impact of surface chemistry. *PNAS* **2010,** 108, 917-924.
5. Lüth, H.; Surface and Interface Physics: Its Definition and Importance. In Solid Surfaces, *Interfaces and Thin Films*, Springer International Publishing: Cham, 2015; pp 1-28.
6. Cole-Hamilton D.J., Tooze R.P: Homogeneous Catalysis — Advantages and Problems. In: Cole-Hamilton D.J., Tooze R.P. (eds) Catalyst Separation, Recovery and Recycling. Catalysis by Metal Complexes, Springer International Publishing: 2006; pp 1-8.
7. Erica. F., Roberta. D. M., Jan. K. Homogeneous and heterogeneous catalysis. *Inorganic and Bioinorganic Chemistry* **2009,** *2, 50.*
8. Misra, K.; Graphene introduction. *Physics of Condensed Matter*. In *Novel Materials*, Elseveir Publishing: 2010; pp 600-617.
9. Zhao, G.; Li, X.; Huang, M.; Zhen, Z.; Zhong, Y.; Chen, Q.; Zhao, X.; He, Y.; Hu, R.; Yang, T.; Zhang, R.; Li, C.; Kong, J.; Xu, J.-B.; Ruoff, R. S.; Zhu, H., The physics and chemistry of graphene-on-surfaces. *Chemical Society Reviews* **2017,** *46* (15), 4417-4449.
10. Wang, X.; Shi, G., An introduction to the chemistry of graphene. *Phys. Chem. Chem. Phys.* **2015,** *17*, 28484-28504.

11. Loh, K. P.; Bao, Q.; Ang, P. K.; Yang, J., The chemistry of graphene. *J. Mater. Chem.* **2010,** *20*, 2277-2289.

12. Zhou, J.; Huang, R., Internal lattice relaxation of single-layer graphene under in-plane deformation. *J. Mech. Phys. Solids* **2008,** *56*, 1609-1623.

13. Ambrosi, A.; Chua, C. K.; Bonanni, A.; Pumera, M., Electrochemistry of graphene and related materials. *Chem. Rev. (Washington, DC, U. S.)* **2014,** *114*, 7150-7188.

14. Geng, X.; Guo, Y.; Li, D.; Li, W.; Zhu, C.; Wei, X.; Chen, M.; Gao, S.; Qiu, S.; Gong, Y.; Wu, L.; Long, M.; Sun, M.; Pan, G.; Liu, L., Interlayer catalytic exfoliation realizing scalable production of large-size pristine few-layer graphene. *Sci. Rep.* **2013,** *3*, 1134, 6 pp.

15. Allen, M. J.; Tung, V. C.; Kaner, R. B., Honeycomb Carbon: A Review of Graphene. *Chem. Rev. (Washington, DC, U. S.)* **2010,** *110*, 132-145.

16. Chen, J.; Yao, B.; Li, C.; Shi, G., An improved Hummers method for eco-friendly synthesis of graphene oxide. *Carbon* **2013,** *64*, 225-229.

17. Hossain, M. Z.; Johns, J. E.; Bevan, K. H.; Karmel, H. J.; Liang, Y. T.; Yoshimoto, S.; Mukai, K.; Koitaya, T.; Yoshinobu, J.; Kawai, M.; Lear, A. M.; Kesmodel, L. L.; Tait, S. L.; Hersam, M. C., Chemically homogeneous and thermally reversible oxidation of epitaxial graphene. *Nat. Chem.* **2012,** *4*, 305-309.

18. Whitener, K. E., Jr.; Sheehan, P. E., Graphene synthesis. *Diamond Relat. Mater.* **2014,** *46*, 25-34.

19. Sud, D.; Mahajan, G.; Kaur, M. P., Agricultural waste material as potential adsorbent for sequestering heavy metal ions from aqueous solutions. A review. *Bioresour. Technol.* **2008,** *99*, 6017-6027.

20. Muramatsu, H.; Kim, Y. A.; Yang, K.-S.; Cruz-Silva, R.; Toda, I.; Yamada, T.; Terrones, M.; Endo, M.; Hayashi, T.; Saitoh, H., Rice husk-derived graphene with nanosized domains and clean edges. *Small* **2014,** *10*, 2766-2770.

21. Gupta, S. S.; Sreeprasad, T. S.; Maliyekkal, S. M.; Das, S. K.; Pradeep, T., Graphene from Sugar and its Application in Water Purification. *ACS Appl. Mater. Interfaces* **2012,** *4*, 4156-4163.

22. Somanathan, T.; Prasad, K.; Ostrikov, K.; Saravanan, A.; Krishna, V. M., Graphene oxide synthesis from agro waste. *Nanomaterials* **2015,** *5*, 826-834.

23. Sun, L.; Tian, C.; Li, M.; Meng, X.; Wang, L.; Wang, R.; Yin, J.; Fu, H., From coconut shell to porous graphene-like nanosheets for high-power supercapacitors. *J. Mater. Chem. A* **2013,** *1*, 6462-6470.

24. Jin, H.; Wang, X.; Gu, Z.; Fan, Q.; Luo, B., A facile method for preparing nitrogen-doped graphene and its application in supercapacitors. *J. Power Sources* **2015,** *273*, 1156-1162.

25. Perreault, F.; Fonseca de Faria, A.; Elimelech, M., Environmental applications of graphene-based nanomaterials. *Chem. Soc. Rev.* **2015,** *44*, 5861-5896.

26. Gao, J.; Liu, F.; Liu, Y.; Ma, N.; Wang, Z.; Zhang, X., Environment-Friendly Method To Produce Graphene That Employs Vitamin C and Amino Acid. *Chem. Mater.* **2010,** *22*, 2213-2218.

27. Lonkar, S. P.; Abdala, A. A., Applications of graphene in catalysis. *J. Thermodyn. Catal.* **2014,** *5*, 132/1-132/6.

28. Fan, X.; Zhang, G.; Zhang, F., Multiple roles of graphene in heterogeneous catalysis. *Chem. Soc. Rev.* **2015,** *44*, 3023-3035.

29. Julkapli, N. M.; Bagheri, S., Graphene supported heterogeneous catalysts: An overview. *Int. J. Hydrogen Energy* **2015,** *40*, 948-979.

30. Singh, R. K.; Kumar, R.; Singh, D. P., Graphene oxide: strategies for synthesis, reduction and frontier applications. *RSC Advances* **2016,** *6* (69), 64993-65011.

31. Dreyer, D. R.; Park, S.; Bielawski, C. W.; Ruoff, R. S., The chemistry of graphene oxide. *Chem. Soc. Rev.* **2010,** *39*, 228-240.

32. Shen, A.; Zou, Y.; Wang, Q.; Dryfe, R. A. W.; Huang, X.; Dou, S.; Dai, L.; Wang, S., Oxygen Reduction Reaction in a Droplet on Graphite: Direct Evidence that the Edge is More Active than the Basal Plane. *Angew. Chem., Int. Ed.* **2014,** *53*, 10804-10808.

33. Johra, F. T.; Lee, J.-W.; Jung, W.-G., Facile and safe graphene preparation on solution based platform. *J. Ind. Eng. Chem. (Amsterdam, Neth.)* **2014,** *20*, 2883-2887.

34. Sudesh; Kumar, N.; Das, S.; Bernhard, C.; Varma, G. D., Effect of graphene oxide doping on superconducting properties of bulk MgB2. *Supercond. Sci. Technol.* **2013,** *26*, 095008, 8 pp.

35. Fujimoto, A.; Yamada, Y.; Koinuma, M.; Sato, S., Origins of sp3C peaks in C1s X-ray Photoelectron Spectra of Carbon Materials. *Analytical Chemistry* **2016,** *88* (12), 6110-6114.

36. Jorio, A., Raman spectroscopy in graphene-based systems: prototypes for nanoscience and nanometrology. *ISRN Nanotechnol.* **2012**, 234216, 16 pp.

37. Shivaveni, B.; Ajitha, A.; Rao, V. U. M., Thermal desorption spectroscopy. *World J. Pharm. Pharm. Sci.* **2015,** *4*, 458-475.

38. Komarneni, M.; Sand, A.; Goering, J.; Burghaus, U.; Lu, M.; Monica Veca, L.; Sun, Y.-P., Possible effect of carbon nanotube diameter on gas-surface interactions - The case of

benzene, water, and n-pentane adsorption on SWCNTs at ultra-high vacuum conditions. *Chem. Phys. Lett.* **2009,** *476*, 227-231.

39. Winkler, A., Thermal desorption of organic molecules. *Springer Proc. Phys.* **2009,** *129*, 29-36.

40. Burghaus, U., Effect of surface defects in heterogeneous catalysis. *Trends Phys. Chem.* **2006,** *11*, 1-19.

41. King, D. A.; Wells, M. G., Molecular beam investigation of adsorption kinetics on bulk metal targets. Nitrogen on tungsten. *Surface Sci.* **1972,** *29*, 454-82.

42. King, D. A., Thermal desorption from metal surfaces. Review. *Surf. Sci.* **1975,** *47*, 384-402.

43. Kisliuk, P., The sticking probabilities of gases chemisorbed on the surfaces of solids. *Phys. Chem. Solids* **1957,** *3*, 95-101.

44. Laha, T.; Agarwal, A., An Introduction to Surface Analysis by XPS and AES, Edited by John F. Watts and John Wolstenholme. *Mater. Manuf. Processes* **2004,** *19*, 571-572.

45. Brundle, C. R.; Baker, A. D.; Editors, *Electron Spectroscopy: Theory, Techniques, and Applications, Vol. 5*. Academic Press: 1984; p 378 pp.

46. Attard, G.; Barnes, C.; Editors, *Surafces, Vol. 1*. Oxford Primers: 1998; p 38 pp.

47. Van Hove, M. A.; Weinberg, W. H.; Chan, C. M., Low Energy Electron Diffraction, experiment, theory, and surface structure determination. *Springer Series in Surface Sciences, Vol. 2*. 1986; pp 14.

48. Jorio, A.; Dresselhaus, G.; Dresselhaus, M. S.; Saito, R., Raman Spectroscopy in Graphene Related Systems. *Wiley VCH.* **2011.**

49. Pimenta, M. A.; Dresselhaus, G.; Dresselhaus, M. S.; Cancado, L. G.; Jorio, A.; Saito, R., Studying disorder in graphite-based systems by Raman spectroscopy. *Phys. Chem. Chem. Phys.* **2007,** *9*, 1276-1291.

50. Ferrari, A. C.; Basko, D. M., Raman spectroscopy as a versatile tool for studying the properties of graphene. *arXiv.org, e-Print Arch., Condens. Matter* **2013**, 1-26, arXiv:1306.5856v1 [cond-mat.mtrl-sci].

51. John, R. F.; Kazuo, N., Introduction to Raman Spectroscopy. *Academic Press Inc*. **1994.**

52. Dresselhaus, M. S.; Jorio, A.; Hofmann, M.; Dresselhaus, G.; Saito, R., Perspectives on Carbon Nanotubes and Graphene Raman Spectroscopy. *Nano Lett.* **2010,** *10*, 751-758.

53. Bokobza, L.; Zhang, J., Raman spectroscopic characterization of multiwall carbon nanotubes and of composites. *eXPRESS Polym. Lett.* **2012,** *6*, 601-608.

54. Ouyang, Y.; Cong, L. M.; Chen, L.; Liu, Q. X.; Fang, Y., Raman study on single-walled carbon nanotubes and multi-walled carbon nanotubes with different laser excitation energies. *Phys. E (Amsterdam, Neth.)* **2008,** *40*, 2386-2389.

55. Costa, S.; Borowiak-Palen, E.; Kruszynska, M.; Bachmatiuk, A.; Kalenczuk, R. J., Characterization of carbon nanotubes by Raman spectroscopy. *Mater. Sci.-Pol.* **2008,** *26*, 433-441.

56. Graphene supermartket Inc. (https://graphene-supermarket.com/)

57. Wasielewski, R.; Yakshinskiy, B. V.; Hedhili, M. N.; Ciszewski, A.; Madey, T. E., Surface chemistry of Ru: relevance to optics lifetime in EUVL. *Proc. SPIE-Int. Soc. Opt. Eng.* **2007,** *6533*, 653316/1-653316/12.

58. Polta, J. A.; Thiel, P. A., Unusually facile dissociation of benzene by ruthenium metal. *J. Am. Chem. Soc.* **1986,** *108*, 7560-7.

59. Jakob, P.; Menzel, D., The adsorption of benzene on ruthenium(001). *Surf. Sci.* **1988,** *201*, 503-30.

60. Chakradhar, A.; Trettel, K.; Burghaus, U., Benzene adsorption on Ru(0 0 0 1) and graphene/Ru(0 0 0 1). How to synthesize epitaxial graphene without STM or LEED? *Chem. Phys. Lett.* **2013,** *590*, 146-152.

61. Van Staden, M. J.; Roux, J. P., The superpostion of carbon and ruthenium Auger spectra. *Appl. Sur. Sci*. **1990**, *44, 259-262.*

62. Singh Raman, R. K.; Chakraborty Banerjee, P.; Lobo, D. E.; Gullapalli, H.; Sumandasa, M.; Kumar, A.; Choudhary, L.; Tkacz, R.; Ajayan, P. M.; Majumder, M., Protecting copper from electrochemical degradation by graphene coating. *Carbon* **2012,** *50*, 4040-4045.

63. Berry, V., Impermeability of graphene and its applications. *Carbon* **2013,** *62*, 1-10.

64. Shih, C.-J.; Wang, Q. H.; Lin, S.; Park, K.-C.; Jin, Z.; Strano, M. S.; Blankschtein, D., Breakdown in the wetting transparency of graphene. *Phys. Rev. Lett.* **2012,** *109*, 176101/1-176101/5.

65. Rafiee, J.; Mi, X.; Gullapalli, H.; Thomas, A. V.; Yavari, F.; Shi, Y.; Ajayan, P. M.; Koratkar, N. A., Wetting transparency of graphene. *Nat. Mater.* **2012,** *11*, 217-222.

66. Shih, C.-J.; Strano, M. S.; Blankschtein, D., Wetting translucency of graphene. *Nat. Mater.* **2013,** *12*, 866-869.

67. Raj, R.; Maroo, S. C.; Wang, E. N., Wettability of Graphene. *Nano Lett.* **2013,** *13*, 1509-1515.

68. Yuan, Y.; Lee, T. R., Contact angle and wetting properties. *Springer Ser. Surf. Sci.* **2013,** *51*, 3-34.

69. Li, Z.; Wang, Y.; Kozbial, A.; Shenoy, G.; Zhou, F.; McGinley, R.; Ireland, P.; Morganstein, B.; Kunkel, A.; Surwade, S. P.; Li, L.; Liu, H., Effect of airborne contaminants on the wettability of supported graphene and graphite. *Nat. Mater.* **2013,** *12*, 925-931.

70. Chakradhar, A.; Sivapragasam, N.; Nayakasinghe, M. T.; Burghaus, U., Support effects in the adsorption of water on CVD graphene: an ultra-high vacuum adsorption study. *Chem. Commun*, 11463-11466.

71. Schmitz, P. J.; Polta, J. A.; Chang, S. L.; Thiel, P. A., Isotope effect in water desorption from ruthenium(001). *Surf. Sci.* **1987,** *186*, 219-31.

72. Hodgson, A.; Haq, S., Water adsorption and the wetting of metal surfaces. *Surf. Sci. Rep.* **2009,** *64*, 381-451.

73. Held, G.; Menzel, D., Structural isotope effect in water bilayers adsorbed on Ru(001). *Phys. Rev. Lett.* **1995,** *74*, 4221-4.

74. Leenaerts, O.; Partoens, B.; Peeters, F. M., Water on graphene. Hydrophobicity and dipole moment using density functional theory. *Phys. Rev. B: Condens. Matter Mater. Phys.* **2009,** *79*, 235440/1-235440/5.

75. Wehling, T. O.; Lichtenstein, A. I.; Katsnelson, M. I., First-principles studies of water adsorption on graphene. The role of the substrate. *Appl. Phys. Lett.* **2008,** *93*, 202110/1-202110/3.

76. Berland, K.; Chakarova-Kaeck, S. D.; Cooper, V. R.; Langreth, D. C.; Schroeder, E., A van der Waals density functional study of adenine on graphene: single-molecular adsorption and overlayer binding. *J. Phys.: Condens. Matter* **2011,** *23*, 135001/1-135001/8.

77. Le, D.; Kara, A.; Schroder, E.; Hyldgaard, P.; Rahman, T., Physisorption of nucleobases on graphene: a comparative van der Waals study. *J. Phys.: Condens. Matter* **2012,** *24*, 424210/1-424210/7.

78. Kozlov, S. M.; Vines, F.; Goerling, A., On the interaction of polycyclic aromatic compounds with graphene. *Carbon* **2012,** *50*, 2482-2492.

79. Chakradhar, A.; Sivapragasam, N.; Nayakasinghe, M. T.; Burghaus, U., Adsorption kinetics of benzene on graphene: An ultrahigh vacuum study. *J. Vac. Sci. Technol., A* **2016,** *34*, 021402/1-021402/4.

80. Chakarova-Kack, S. D.; Schroder, E.; Lundqvist, B. I.; Langreth, D. C., Application of van der Waals Density Functional to an Extended System: Adsorption of Benzene and Naphthalene on Graphite. *Phys. Rev. Lett.* **2006,** *96*, 146107/1-146107/4.

81. Chang, C.-H.; Fan, X.; Li, L.-J.; Kuo, J.-L., Band Gap Tuning of Graphene by Adsorption of Aromatic Molecules. *J. Phys. Chem. C* **2012,** *116*, 13788-13794.

82. Li, Y.; Tu, X.; Wang, H.; Sanvito, S.; Hou, S., First-principles investigation on the electronic efficiency and binding energy of the contacts formed by graphene and poly-aromatic hydrocarbon anchoring groups. *J. Chem. Phys.* **2015,** *142*, 164701/1-164701/7.

83. Vernov, A.; Steele, W. A., Computer simulations of benzene adsorbed on graphite. 2. 298 K. *Langmuir* **1991,** *7*, 2817-20.

84. Al Zahrani, A. Z., First-principles study on the structural and electronic properties of graphene upon benzene and naphthalene adsorption. *Appl. Surf. Sci.* **2010,** *257*, 807-810.

85. Bjork, J.; Hanke, F.; Palma, C.-A.; Samori, P.; Cecchini, M.; Persson, M., Adsorption of Aromatic and Anti-Aromatic Systems on Graphene through π-π Stacking. *J. Phys. Chem. Lett.* **2010,** *1*, 3407-3412.

86. Zacharia, R.; Ulbricht, H.; Hertel, T., Interlayer cohesive energy of graphite from thermal desorption of polyaromatic hydrocarbons. *Phys. Rev. B: Condens. Matter Mater. Phys.* **2004,** *69*, 155406/1-155406/7.

87. Krasnenko, V.; Kikas, J.; Brik, M. G., Modification of the structural and electronic properties of graphene by the benzene molecule adsorption. *Phys. B (Amsterdam, Neth.)* **2012,** *407*, 4557-4561.

88. Silvestrelli, P. L.; Ambrosetti, A., Including screening in van der Waals corrected density functional theory calculations. The case of atoms and small molecules physisorbed on graphene. *J. Chem. Phys.* **2014,** *140*, 124107/1-124107/8.

89. Chakradhar, A.; Trettel, K.; Burghaus, U., Benzene adsorption on Ru(0 0 0 1) and graphene/Ru(0 0 0 1). How to synthesize epitaxial graphene without STM or LEED? *Chem. Phys. Lett.* **2013,** *590*, 146-152.

90. Rochefort, A.; Wuest, J. D., Interaction of Substituted Aromatic Compounds with Graphene. *Langmuir* **2009,** *25*, 210-215.

91. Rofer-DePoorter, C. K., A comprehensive mechanism for the Fischer-Tropsch synthesis. *Chem. Rev.* **1981,** *81*, 447-74.

92. Nieszporek, K.; Drach, M., Alkane separation using nanoporous graphene membranes. *Phys. Chem. Chem. Phys.* **2015,** *17*, 1018-1024.

93. Paserba, K. R.; Gellman, A. J., Effects of conformational isomerism on the desorption kinetics of n-alkanes from graphite. *J. Chem. Phys.* **2001,** *115*, 6737-6751.

94. Gellman, A. J.; Paserba, K. R., Kinetics and Mechanism of Oligomer Desorption from Surfaces: n-Alkanes on Graphite. *J. Phys. Chem. B* **2002,** *106*, 13231-13241.

95. Jachimowski, T. A.; Weinberg, W. H., Trapping-mediated dissociative chemisorption of cyclopropane on Ru(001) via C-C bond cleavage. *Surf. Sci.* **1997,** *370*, 71-76.

96. Jachimowski, T. A.; Weinberg, W. H., Trapping-mediated dissociative chemisorption of ethane and propane on Ru(001). *Surf. Sci.* **1997,** *372*, 145-154.

97. Weaver, J. F.; Krzyzowski, M. A.; Madix, R. J., Direct dissociative chemisorption of alkanes on Pt(111). Influence of molecular complexity. *J. Chem. Phys.* **2000,** *112*, 396-407.

98. Arena, M. V.; Deckert, A. A.; Brand, J. L.; George, S. M., Surface diffusion and desorption of pentane isomers on ruthenium(001). *J. Phys. Chem.* **1990,** *94*, 6792-7.

99. Brand, J. L.; Arena, M. V.; Deckert, A. A.; George, S. M., Surface diffusion of n-alkanes on ruthenium(001). *J. Chem. Phys.* **1990,** *92*, 5136-43.

100. Hamza, A. V.; Steinruck, H. P.; Madix, R. J., The dynamics of the dissociative adsorption of alkanes on iridium(110). *J. Chem. Phys.* **1987,** *86*, 6506-14.

101. Londero, E.; Karlson, E.; Landahl, M.; Ostrovskii, D.; Rydberg, J.; Schroeder, E., Desorption of n-alkanes from graphene: a van der Waals density functional study. *J. Phys.: Condens. Matter* **2012,** *24*, 424212/1-424212/8.

102. Lei, R. Z.; Gellman, A. J.; Koel, B. E., Desorption energies of linear and cyclic alkanes on surfaces: anomalous scaling with length. *Surf. Sci.* **2004,** *554*, 125-140.

103. Kadossov, E.; Goering, J.; Burghaus, U., Molecular beam scattering of linear and branched butane on graphite (HOPG). *Surf. Sci.* **2007,** *601*, 3421-3425.

104. Funk, S.; Burghaus, U.; White, B.; O'Brien, S.; Turro, N. J., Adsorption dynamics of alkanes on single-wall carbon nanotubes. A molecular beam scattering study. *J. Phys. Chem. C* **2007,** *111*, 8043-8049.

105. Tait, S. L.; Dohnalek, Z.; Campbell, C. T.; Kay, B. D., n-alkanes on Pt(111) and on C(0001)/Pt(111): Chain length dependence of kinetic desorption parameters. *J. Chem. Phys.* **2006,** *125*, 234308/1-234308/15.

106. Tait, S. L.; Dohnalek, Z.; Campbell, C. T.; Kay, B. D., n-alkanes on MgO(100). II. Chain length dependence of kinetic desorption parameters for small n-alkanes. *J Chem Phys* **2005,** *122*, 164708.

107. Yang, T.; Berber, S.; Liu, J.-F.; Miller, G. P.; Tomanek, D., Self-assembly of long chain alkanes and their derivatives on graphite. *J. Chem. Phys.* **2008,** *128*, 124709/1-124709/8.

108. Kamiya, K.; Okada, S., Energetics and electronic structures of alkanes and polyethylene adsorbed on graphene. *Jpn. J. Appl. Phys.* **2013,** *52*, 06GD10/1-06GD10/5.

109. Sivapragasam, N.; Nayakasinghe, M. T.; Burghaus, U., Adsorption of n-butane on graphene/Ru(0001)-A molecular beam scattering study. *J. Vac. Sci. Technol., A* **2016,** *34*, 041404/1-041404/6.

110. Sivapragasam, N.; Nayakasinghe, M. T.; Chakradhar, A.; Burghaus, U., Effects of the support on the desorption kinetics of n-pentane from graphene: An ultrahigh vacuum adsorption study. *J. Vac. Sci. Technol., A* **2017,** *35*, 061404/1-061404/4.

111. Wang, W.; Gong, J., Methanation of carbon dioxide: An overview. *Front. Chem. Sci. Eng.* **2011,** *5*, 2-10.

112. Burghaus, U., Surface chemistry of CO2 - Adsorption of carbon dioxide on clean surfaces at ultrahigh vacuum. *Prog. Surf. Sci.* **2014,** *89*, 161-217.

113. Burghaus, U. In *Surface science studies of carbon dioxide chemistry*, Elsevier B.V.: 2013; pp 27-47.

114. Burghaus, U., Surface science perspective of carbon dioxide chemistry-Adsorption kinetics and dynamics of CO2 on selected model surfaces. *Catal. Today* **2009,** *148*, 212-220.

115. Walter, H.; Birgit, P., Plant Biochemistry. *Academic Press*. **2011.**

116. D'Alessandro, D. M.; Smit, B.; Long, J. R., Carbon Dioxide Capture: prospects for New Materials. *Angew. Chem., Int. Ed.* **2010,** *49*, 6058-6082.

117. Wang, S.-G.; Cao, D.-B.; Li, Y.-W.; Wang, J.; Jiao, H., Chemisorption of CO2 on nickel surfaces. *J. Phys. Chem. B* **2005,** *109*, 18956-18963.

118. Chakarov, D. V.; Osterlund, L.; Kasemo, L., Water adsorption and coadsorption with potassium on graphite. *Langmuir*. **1995**, 11, 1201-1214.

119. Mishra, A. K.; Ramaprabhua, S., Carbon dioxide adsorption in graphene sheets. *AIP Adv.* **2011,** *1*, 032152, 6 pp.

120. Thakur, D. P.; Barde, N. P.; Bardapurkar, P. P.; Khairnar, R. S., A density functional study of the adsorption of carbon dioxide molecule on graphene. *Ukr. J. Phys.* **2013,** *58*, 841-845.

121. Zhu, Y.; Murali, S.; Cai, W.; Li, X.; Suk, J. W.; Potts, J. R.; Ruoff, R. S., Graphene and Graphene Oxide: Synthesis, Properties, and Applications. *Adv. Mater. (Weinheim, Ger.)* **2010,** *22*, 5226.

122. Tang, S.; Cao, Z., Adsorption of nitrogen oxides on graphene and graphene oxides. Insights from density functional calculations. *J. Chem. Phys.* **2011,** *134*, 044710/1-044710/14.

123. Dimiev, A. M.; Tour, J. M., Mechanism of Graphene Oxide Formation. *ACS Nano* **2014,** *8*, 3060-3068.

124. Dave, S. H.; Gong, C.; Robertson, A. W.; Warner, J. H.; Grossman, J. C., Chemistry and Structure of Graphene Oxide via Direct Imaging. *ACS Nano* **2016,** *10*, 7515-7522.

125. Reuter, K.; Stampfl, C.; Ganduglia-Pirovano, M. V.; Scheffler, M., Atomistic description of oxide formation on metal surfaces. The example of ruthenium. *Chem. Phys. Lett.* **2002,** *352*, 311-317.

126. Hrbek, J.; van Campen, D. G.; Malik, I. J., The early stages of ruthenium oxidation. *J. Vac. Sci. Technol., A* **1995,** *13*, 1409-12.

127. Sivapragasam, N.; Nayakasinghe, M. T.; Burghaus, U., Adsorption Kinetics and Dynamics of CO2 on Ru(0001) Supported Graphene Oxide. *J. Phys. Chem. C* **2016,** *120* (Copyright (C) 2018 American Chemical Society (ACS). All Rights Reserved.), 28049-28056.